Radial Velocity Studies of Eclipsing Binary Systems

A Thesis

submitted for the Award of Ph.D. degree of

MOHANLAL SUKHADIA UNIVERSITY

in the

Faculty of Science

By

Priyanka Chaturvedi

Under the supervision of

Dr. P. Janardhan

Professor

Physical Research Laboratory, Ahmedabad

DEPARTMENT OF PHYSICS

FACULTY OF SCIENCE

MOHANLAL SUKHADIA UNIVERSITY

UDAIPUR (RAJ.)

Year of submission: 2016

DECLARATION

I, **Ms. Priyanka Chaturvedi**, D/o Mr. Rakesh Kumar Chaturvedi and Mrs. Neerja Chaturvedi, resident of 113, PRL Thaltej Hostel, Ahmedabad 380054, hereby declare that the research work incorporated in the present thesis entitled, **"Radial Velocity Studies of Eclipsing Binary Systems"** is my own work and is original. This work (in part or in full) has not been submitted to any University for the award of a Degree or a Diploma. I have properly acknowledged the material collected from secondary sources wherever required. I solely own the responsibility for the originality of the entire content.

Date:

Priyanka Chaturvedi
(Author)

CERTIFICATE

We feel great pleasure in certifying the thesis entitled, **"Radial Velocity Studies of Eclipsing Binary Systems"** by Ms. Priyanka Chaturvedi. She has completed the following requirements as per Ph.D regulations of the University.

(a) Course work as per the university rules.

(b) Residential requirements of the university.

(c) Regularly submitted six monthly progress reports.

(d) Presented her work in the departmental committee.

(e) Published minimum of one research paper in a referred research journal.

We recommend the submission of thesis.

Date:

Prof. P. Janardhan
Professor,
Physical Research Laboratory,
Navrangpura,
Ahmedabad

Countersigned by
Head of the Department

Dedicated

to my beloved Baba-Dadi

Contents

List of Figures

List of Tables

Acknowledgements

I feel elated to hold the 5 years of hard work in the form of this manuscript. Looking back at the journey which started a little over 5 years back, I remember a lot many people who have mitigated the arduous paths traversed in this journey.

I wish to begin by expressing my gratitude towards the first teachers of my life, my parents, who were supportive of my decision in moving out of my home city to pursue a PhD, a very first in my family. For the duration of five years, I worked on a challenging and an emerging field in astronomy under the guidance of Dr Abhijit Chakraborty and Prof. Janardhan (Jerry). I thank them for having taught me the science and techniques required to proceed in the direction of the thesis. Jerry, thank you for giving me the atmosphere that encouraged me to talk on any thing under the earth from people to places, history to mythology around the world. I am happy to have got a chance to work with you Abhijit; because of you, I got introduced to world-class researchers who are pioneers in their respective fields. It would be unfair not to mention the name of Prof. Anandarao. He has advised and mentored me to look at the research problems and carefully inspect each and every idea. Guruji, your patience and meticulous reading of the first draft of my thesis has ultimately shaped up in the form of this book and I am heartily indebted to you for this. Whenever I felt low about my work or any problem, I was re-energized by your motivating words. I am thankful to all my three mentors for carefully going through this thesis and making critical and useful comments and corrections. I would also like to extend my thanks to their spouses. Their concern on my work progress has kept me motivated throughout.

I appreciate the help received from my past and current research group members. Foremost, I would like to acknowledge Vaibhav and Varun for being such nice labmates. I have spent some good time with you guys, especially at the observatory. Those late night observing sessions, eating the special ‘Dal-Bati’ at Mount Abu, speaking the mind out with no reservations, you guys were always there for me. Thanks Vaibhav for assisting me in observations and debugging my codes at various stages. I heartily thank you Varun, for a friend like you is difficult to get. Thanks for being my technical advisor while purchasing any electronics equipment :) I also take the opportunity to thank Mr Vishal Shah, Mr F.M. Pathan, Mr S. Doshi, Aashka, Kapil and Prasad who have not only helped me with observations and other technical aspects at various stages of the project but have also showed concern for my work. I am gratified towards my collaborators at Penn State, USA; Dr Rohit Deshpande, Dr Suvrath Mahadevan and Arpita Roy who have helped me in all possible ways for computational help, with the data reduction pipeline and scientific discussions we had over emails and skype. I thank Dr Arvind Rajpurohit for some good suggestions during my thesis writing stage. A major portion of my thesis has been spent at the observatory, Mount Abu. The entire staff at Mount Abu has been very co-operative. I wish to thank Mr Rajesh Shah, Mr G.S. Rajpurohit, Mr Jinesh Jain, Mr Mathur, Mr Nafees, Mr Patwal, Mr Narayan Singh, Mr Padam Singh, Akshay, Prakash, Vishakh for the help with the observations and the entire canteen and house-keeping staff at Mount Abu for keeping the environment pleasant. It gives me immense pleasure to mention the name of Rajpurohit Aunty whose love and affection has compensated for the motherly love and care I received at home. Thank you Aunty for the wonderful lunches you have invited me over for.

I feel revered to have a cordial group of researchers working in the Astronomy and Astrophysics Division. I take this opportunity to thank Prof. N.M. Ashok for examining my thesis. I also express my gratitude towards Dr Ashok Singal, Prof Baliyan, Prof U.C. Joshi, Dr Shashikiran, Dr Mudit Srivastava, Prof Chandrashekhar, Prof Hari Om Vats, Prof D.P.K. Banerjee, Dr Santosh Vadawale, Dr Sachindra Naik, Mr A.B. Shah, Dr Venkat, Dr Veeresh Singh for indulging in scientific and technical dialogues at area seminars and tea times which have bettered me as a researcher. I would also like to acknowledge the help I have received from Mr Bhagirath Kuntar who has promptly carried out the administrative work at Thaltej campus. I can't thank enough my past seniors at the division Ashish, Susanta, Sunil, Tapas, Arun, Vishal and Blesson whose suggestions during student discussions have always helped me in various ways. I am also grateful to my juniors at the division without whom the division would be less lively; to name them, Gaurav, Prahlad, Navpreet and Kumar. Mithun, Samir, Rathna and Suruchi, thanks are due to you, the concern you showed for my research work are heartily appreciated. I want to express my profound thanks to my batchmate Tanmoy, I have benefited a lot due to the fruitful scientific discussions I had with you. Thanks is perhaps a small word for all the times you have been there for me as a colleague and as a friend. I would also mention the name of my school teachers, Ms Sanla, Mrs Yawalkar, Mr Dhavle, Mr Gatne for their constant encouragement during my school days and two of my mentors during my graduation, Dr Raka Dabhade and Prof. Ananthkrishnan who have played pivotal role in motivating me to pursue PhD.

I am obliged to Department Of Space, Govt. of India for the research grant offered to me during my tenure at PRL. I extend my thanks to the past and current Directors, Deans, Academic Committee Chairmen, Registrars, Astronomy Division Chairmen and the entire Academic committee members, course work instructors at PRL who were always supportive in imparting science-based suggestions, providing facilities and due permissions at each stage of my PhD. I am also thankful to the Dean and Head of Physics Dept. at MLSU, Udaipur, and Hemant ji and Jagdish ji for their extended co-operation. I would like to especially mention the international travel amount which was granted to me by PRL during my tenure through which I could attend and reach out to international audience. I am gratified towards Prof Francesco Pepe, Prof Jean Pierre Mallard, Prof Michel Mayor, Prof Frank Grupp, Prof Daniel Rouan for hosting me and giving me a chance to present my research work at their institutes. A special thanks to Sandesh, Rajlaxmi, Priya and Ashish for the kind hospitality rendered at their respective places during my international visits. I owe my thanks to the vast knowledge which is readily available at internet (Google, NASA ADS, SIMBAD data base, arxiv) which have played a key role in my research. I am gratified to the Thaltej canteen and CISF who have provided unceasing services. I would also like to acknowledge the account section, purchase, workshop facilities, transport section and the entire administrative services of PRL for their prompt help offered to me. I wish to thank the efficient computational services at PRL especially Hitendra Mishra ji, Samuel, and Jigar ji. Thanks to Pragya and Dr Nishtha for their ready to help attitude for procuring books and similar facilities at library. Pragya, you have taken all the efforts at your disposal for offering uninterrupted services. It would not be an exaggeration to mention that I got to see home away from one only because of you. Thanks to you and my youngest best buddy ‘Golu’, you have been a very big bundle of joy for me.

I am privileged to have many good friends who have been a part of this journey for me. Thanks to Shaheen, I missed your marriage due to my on-going work, something which I had always promised to attend. Thanks for always being so patient with me. Mayank, I don’t know how to thank you. Thanks for the discussions, encouragement, proof-reading and all the care and concern which you have tirelessly offered me. Uma and Lata, though you moved at different places to pursue your PhDs, the bond we share has helped me grow a lot. Thank you Kamlesh, Dhara, Aditya, Digu, Tinkal and Prasanna for the beautiful times we have spent together especially the cooking parties and late night tea and ice-cream parties. I would like to thank Arko, Shweta and Sneha for being patient listeners and enthusiastic partners in any plans made at any time. You friends have been a wonderful source of happiness and fun. I relish the time I have spent at PRL, especially Thaltej hostel, and I thank each one of you for the same. I would like to thank Naveen, Monojit, Deepak, Dipti, Lalit, Yashpal, Bhavya, Rupa, Rukmani, Amrendra, Arvind Singh, Aarthy, Bivin, Jinia, Gaurav Tomar, Gulab, Reddy, Wageesh, Upendra, Lekshmy, Midhun, Avdhesh, Chandan(s), Rangu, Kuldeep and Jabir for their company. I am grateful towards my other close buddies, Sonal, Yogita and Panchali who believed in me even when I gave up. I am obliged towards my entire Udaan family, especially Dr Prakash and Rupal who introduced me to the source of happiness of teaching deserving kids, the peace I gather after meeting this family has helped me concentrate in my research.

This thesis wouldn't have been possible without a supportive family. I am grateful to them that they co-operated with my mood swings, my prolonged stays in the laboratory and frequent observatory trips and the little time I got to spend with them at home. Thanks to my sister, Himani Didi, for being such an inspiration to motivate me to pursue a PhD. I admire you for so many things for being independent, creative and humble. I would also like to thank you Prashant Jiju. Having patience is something to learn from you. I am thankful to have a wonderful set of grandparents and relatives who have always been supportive of my work. Had you been here, Baba and Dadi, I am pretty sure you would have been happiest to see this, but I am glad it has only been possible due to your blessings. I am indebted to my parents, they are the best part that has happened to my life.

Priyanka

ABSTRACT

Eclipsing Binaries (EB) are systems in which two stars orbit around the common center of mass at such an angle that they are seen transiting each other to an observer on Earth. Mass and radius, the two fundamental properties of a star that allow us to infer its age, evolution and luminosity, can be determined precisely from observations of such EB systems. Stars having masses $\geq 1\ M_\odot$ observationally match well with the theoretical models of convective interiors and radiative atmospheres. However, there have been discrepancies reported for the observed and model-derived stellar radii of very low mass stars (VLMS) of masses $\leq 0.6\ M_\odot$ (Torres, Andersen and Giménez, 2010). With the motivation to study these VLMS, which are poorly modelled due to limited observational data, we shortlisted a collection of 10 potential EB candidates from the photometric catalogues of Kepler, *STEREO*, and *Super-Wasp* for the EB programme initiated at Physical Research Laboratory (PRL). The aim of the study is to look for single-lined EB systems (for which spectra of only the primary can be recorded), where VLMS occur as companions to F, G, K type primaries, for precise characterization of masses and radii at better accuracies. Radial velocity (RV) data of these sources were obtained using the high-resolution spectrograph, Physical Research Laboratory Advanced Radial velocity Abu-sky Search (PARAS) (Chakraborty *et al.*, 2014) coupled with the 1.2 m telescope at Gurushikhar Observatory, Mount Abu, India. Wideband differential photometry with the help of a 10 inch telescope located at PRL's Mount Abu Observatory has also been performed to complement the spectroscopy. In addition, for a few sources, the archival photometry data have been analysed and included in our study. A software code, PARAS SPEC has been developed to determine the stellar properties of the host star (T_{eff}, $[Fe/H]$ and $\log g$), essential to determine the mass and radius of its companion, based on the synthetic spectral fitting and equivalent width methods. The basic principles and methodology utilized to develop this tool and results obtained when applied to some of the programme stars are discussed.

The major result that has emerged from the work is the confirmation of discovery and characterization of stellar parameters of four VLMS out of which three are mid M dwarf secondaries (M3/M4 spectral type) in three F+M EB systems namely, HD 213597, HD 23765 and SAO 106989. Orbital parameters and system properties such as period, RV semi-amplitude, semi-major axis, masses, radii of the components and inclination in all but one system are derived here at accuracies of $5-8\%$. The fourth EB, J2343+29, is a K+M EB where the secondary has a mass of 0.098 ± 0.003 $M_{\odot}$, the second least massive star discovered till date, for which masses and radii are determined with accuracies of $4-5\%$. A comparison has been made between the values determined from observations and those derived theoretically for all the M dwarfs. It is seen that for the M dwarfs, HD 213597B and HD 23765B, the radii derived from observations are larger than the model derived values (Baraffe *et al.*, 2015); while for J2343+29B, the observed value is in agreement with the model. However, for the fourth M dwarf studied here, namely, SAO 106989B, the observationally reported value of the radius based on SW photometry is smaller than the theoretically derived one. We suspect noisy photometry data for erroneous measurements for the radius, demanding thus, the need for accurate ground based photometry. The study of mass-radius relation for VLMS at high accuracies has been limited. A significant contribution from this work is the addition of four VLMS to the existing 26 VLMS studied in literature previously for the determination of their masses and radii at similar high accuracies.

Keywords: Low Mass stars - Eclipsing Binaries: Techniques: High resolution Spectroscopy, Photometry, Radial Velocity: Spectral property of the star

Chapter 1

Introduction

Stars form the primary building blocks of galaxies and hence fundamental understanding of their structure and evolution is immensely important. Stars are the natural laboratories where we can test our models and theories. The pre-main sequence and the main sequence evolution of a star depends on its mass and the initial chemical composition. Testing of various stellar structural and evolutionary models involves precise measurements of physical parameters such as age, mass, radius, temperature, chemical composition of the stars (Torres, Andersen and Giménez, 2010). The sample size should be significant in order to test and reconcile the stellar evolutionary models. Accurate direct determination of stellar parameters like mass and radius are only possible by observations of eclipsing binary stars, the kind of binaries focused upon in this thesis. Such systems offer a unique opportunity to study stellar and orbital parameters by quantifying the gravitational interaction between the components.

1.1 Motivation for the current research work

Stars in binaries wherein both the components have masses $\geqslant 1M_{\odot}$ have been studied for a long time and significant advances have been made since then to determine their physical properties by photometry and spectroscopy techniques

(Popper, 1974; Andersen, 1975; Vaz *et al.*, 1997; Popper and Tomkin, 1984; Andersen and Clausen, 1989; Ribas, Jordi and Torra, 1999; Torres *et al.*, 2000; Lacy *et al.*, 2004; Southworth and Clausen, 2007; Pietrzyński *et al.*, 2009). The stellar models associated with such objects have been able to reproduce the observations fairly well (Andersen, 1991, 1998; Torres and Ribas, 2002). However, low mass stars (LMS), objects having masses less than $1M_{\odot}$ (Ribas *et al.*, 2008), are studied poorly, mainly because of their relative faintness in the visible bands. The study of such stars was initiated by Kumar (1963) who showed that there is a lower limit to the mass of a main sequence star, the hydrogen burning minimum mass (HBMM) at around 0.085 $M_{\odot}$, below which the stars become completely degenerate (Hayashi and Nakano, 1963). Objects having masses between $0.085 - 0.6$ $M_{\odot}$ are termed as very low mass stars (VLMS) (Chabrier and Baraffe, 1997b). Based on spectral classification, these objects are M dwarfs having spectral types ranging from M_0 to M_{10} (Baraffe and Chabrier, 1996). VLMS objects also include the recently studied new class of objects, L and T dwarfs, first identified by Kirkpatrick (2005) which lie very close to the boundary of the HBMM. There are other interesting objects known as brown dwarfs, the substellar objects which lie below the HBMM and are thus unable to sustain hydrogen burning (Chabrier and Baraffe, 1997a). The term brown dwarf was proposed by Tarter and the objects were first discovered by Nakajima *et al.* (1995). VLMS form a major fraction of the galactic population (Chabrier, 2003). Salpeter (1955) was first to show that the distribution of stars more massive than Sun can be represented by a power-law function. A similar distribution was observed for VLMS objects (for masses less than 0.6 $M_{\odot}$) (Mera, Chabrier and Baraffe, 1996), $dN/dm \propto m^{-\alpha}$ with $\alpha \approx 2 \pm 0.5$. Despite the monotonic increasing nature of the mass function with decreasing mass, these stars are studied poorly, prominently due to their less luminous nature in the visible band with their peak emission lying in the infrared wavelengths.

The abundance of M dwarfs also makes them prominent targets for the hunt of planets around them. The characterization of a planet's mass and radius requires precise study of its host star. Thus, it is of immense importance to model the masses, radii and thereby the interiors of the parent stars precisely. As seen from the statistical analysis of the optical and near-infrared photometry light curves on the candidates from Kepler Input Catalogue, an occurrence rate of $1-2$ planets is predicted per M dwarf with orbital periods less than 150 days (Dressing and Charbonneau, 2013; Ballard and Johnson, 2014). The smaller size of M dwarfs leads to a higher probability of discovering earth-like planets around them due to a relatively larger transit depth induced in comparison to the transit depth induced by a similar mass planet associated with a star having mass $\geqslant 1$ $M_{\odot}$. Apart from the planet causing a larger transit depth on its host M dwarf, the planet will also exhibit a relatively larger gravitational force on its companion M dwarf in comparison to a similar mass planet associated with a star having mass $\geqslant 1$ $M_{\odot}$. Thereby, smaller planets around M dwarfs can be easily detected within the current existing RV precision limitations on large telescopes. The size and evolution of habitable zone of a planet, which is defined as the region around a terrestrial planet with atmospheric conditions favourable to sustain liquid water on its surface (Hart, 1978; Kopparapu *et al.*, 2014), depends on the mass of the parent star. Thereby, the habitable zone boundary for a M dwarf would be closer than that for a solar mass star and hence a planet lying in this zone would be comparatively easier to detect as compared to a similar mass planet around a solar type star. Since characterization of such planets require accurate modelling of their VLMS hosts at high accuracies, it is necessary to increase the sample size of study for VLMS objects.

There are several discrepancies regarding the stellar parameters associated with the VLMS. In order to make critical assessment on stellar evolution models, a general perception is that an uncertainty above 10% on the observed parameters like masses and radii is unacceptable (Torres, Andersen and Giménez, 2010). A total of 95 detached EB systems, having accuracies on masses and radii as high as 3%, were identified and discussed upon in a critical compilation by Torres, Andersen and Giménez (2010). The authors asserted from their work that the VLMS objects, which occur in short orbital period binaries, have a radius 10% larger than the binaries in long period orbit. Mass-Radius (M-R) relation from theoretical models serve a crucial test for verification of the stellar parameters of M dwarfs against the values derived from observations. A vast majority of observations of M dwarfs for varying masses have reported a higher radius by $10-20\%$ and a temperature lower by $5-10\%$ than those predicted by the models (Torres and Ribas, 2002; Ribas, 2003; López-Morales and Ribas, 2005; López-Morales, 2007; Ribas *et al.*, 2008; Torres, Andersen and Giménez, 2010). The mismatch of the radii as seen in these stars is termed as the "M dwarf radius problem" (Triaud *et al.*, 2013). Studying VLMS in EBs with an aim to alleviate the M dwarf radius problem is the motivation for the current research work.

This introductory Chapter gives an overview of various types of eclipsing binaries (EBs), the prime focus of this research work. An introduction is given to the techniques undertaken to study these objects, namely, the radial velocity (RV) technique and transit photometry. The discrepancies associated with the mismatch in the measurements of masses and radii through observations and the existing stellar models for VLMS objects, and the hypotheses, which are postulated to reason for some of these observed discrepancies, are described. At the end of the Chapter, we summarize the objectives of the research work undertaken.

1.2 Binary stars

The term 'binary' in context of double stars was first used by Sir William Herschel while cataloguing 500 new nebulae, stars and clusters of stars (Herschel, 1802). The occurrence of binary systems is quite common. A statistical study of the binaries using the WIYN 3.5 m and Gemini 8.1 m telescopes on the Kepler exoplanet host stars by Horch *et al.* (2014) has revealed a binary fraction of $40-50\%$. These results are in accord with the work done by Duquennoy and Mayor (1991), where they found a binarity fraction of $\sim$ 57% on solar type stars; and the work done by Fischer and Marcy (1992) on M dwarfs, where they found a binarity fraction of $\sim$ 42%. Binary stars have led to the determination of an empirical mass-luminosity relationship through which the masses of single stars can be estimated (Kuiper, 1938). Angular momentum and mass ratio remain conserved in binary systems and thus can shed light on the conditions under which the stars were formed (Larson, 2001).

Calculation of their orbits allows masses of their companion stars to be determined directly, which helps us gather information on other stellar parameters, such as radius and density. Consider a binary system where the two stars are moving around the common centre of mass in circular orbits with velocities v_1 and v_2. Their velocities can be written as (Carroll and Ostlie, 2006):

$$v_1 = \frac{2\pi a_1}{P} \quad \text{and} \quad v_2 = \frac{2\pi a_2}{P} \tag{1.1}$$

where a_1 and a_2 are the semi-major axes of the ellipses of the binary orbits having a period P. The quantities v_1 and v_2 are not directly observed. Instead, what we observe is the projected velocities of the stars along the line of sight. The angle formed between the orbital plane of the binary and the plane of the sky (perpendicular to observer's line of sight) is called the angle of inclination (i). The observed projected velocities for the two stars is given as:

$$v_{r1} = v_1 \sin i \quad \text{and} \quad v_{r2} = v_2 \sin i \tag{1.2}$$

The ratio of masses of the two stars is given as

$$\frac{m_1}{m_2} = \frac{a_2}{a_1} \tag{1.3}$$

The orbital separation of the components is given as

$$a = a_1 + a_2 = \frac{P}{2\pi}(v_1 + v_2) \tag{1.4}$$

Kepler's third law gives the relation between the orbital period and the orbital separation of a two-body system as

$$P^2 = \frac{4\pi^2 a^3}{G(m_1 + m_2)} = \frac{P^3 (v_1 + v_2)^3}{2\pi G(m_1 + m_2)} \tag{1.5}$$

Rearranging the equation, we get

$$m_1 + m_2 = \frac{P}{2\pi G}(v_1 + v_2)^3 \tag{1.6}$$

Substituting Eqn. 1.2 in the above equation, we derive a relation between the observable projected velocity and masses for the two stars in a binary orbit.

$$m_1 + m_2 = \frac{P}{2\pi G}\frac{(v_{r1} + v_{r2})^3}{\sin^3 i} \tag{1.7}$$

Since, our study involves eclipsing binaries (EBs), a brief description is given below.

1.3 EBs and their classification

Stellar systems gravitationally bound to each other where the orbital plane is inclined in such a way that one component passes in front of the other causing variations in brightness are known as EBs (Kallrath and Milone, 2000). Photometric light curve modelling of these stars enables one to get the value of radius and effective temperature of the components (Carroll and Ostlie, 2006). Spectroscopy gives more information on such systems than photometry. Depending on the period of the binary system, we see the periodic shifts in the Doppler lines present in the spectra of the component stars. If the luminosities of both the components are comparable, then the spectra of both the stars are observable. These are called double-lined spectroscopic binaries (SB2). For the cases, where spectra of only single star are visible due to intrinsic faintness of the secondary component, the stars are called single-lined spectroscopic binaries (SB1) (Carroll and Ostlie, 2006). VLMS, which are relatively faint in the visible band, can be studied indirectly in SB1 systems.

Based on their orbital morphology, the binary systems may be classified as follows:

- **Detached EBs:** The first class is the well-separated EB also known as detached EB, component stars of which have very little effect on each other, and their evolution is similar to that of single stars. Such stars can thus be easily used to verify stellar evolutionary models. In detached EBs, the Roche lobes for both the component stars are not filled and hence there is no mass transfer between the components.

- **Semi-detached EBs:** For the semi-detached systems, the more massive component is the main sequence star and the less massive component is usually a cooler and larger sub-giant with partly or fully filled Roche lobe (Malkov *et al.*, 2006). In the case of fully filled Roche lobe, mass transfer can occur from the more massive star to its companion.

- **Contact EBs:** The third class is of the close or contact binaries, the ones where each component has a surface larger than its Roche lobe (Wilson, 1979). Study of evolution processes of contact binaries is a little more complicated as they evolve via angular momentum losses by magnetized winds and also by mass transfer. The tidal force in contact binaries, which is stronger than the other two classes, and viscous dissipation occurring in the system drive the EBs towards a synchronous orbit (Rasio, 1995).

The ability of an observer to predict precise masses and radii in detached EBs permit direct comparison with the models at a fundamental level (Feiden, 2015). The determination of masses, radii and temperatures in case of EBs, where both the components can be studied by spectroscopy and photometry, help us deduce luminosity of each of the stars in the system and hence precise measurement of their distance can be accomplished. Thus, EBs are used as standard candles upto distances of several kiloparsecs in some cases, especially where extragalactic EBs are discovered, a distance of 45.7 ± 1.6 kpc is estimated for the Large Magellanic Cloud and a distance of 772 ± 44 kpc is estimated for the Andromeda Galaxy with the help of EBs (Guinan *et al.*, 1998; Ribas *et al.*, 2005).

1.4 EB: Methods of Detection

VLMS objects are the prime sources of interest for this thesis work. Though, it is not always possible to resolve the individual components of the binary by the direct methods of detection like imaging, it is still possible to probe the system by methods like astrometry or RV and transit photometry and perceive useful information. In single-lined detached EB systems where VLMS objects occur as companions to brighter F, G and K type stars, RV and transit photometry techniques ensure indirect determination of stellar parameters at high accuracies. This section focuses on the description of both the techniques.

1.4.1 Transit photometry

In order to monitor eclipses, the technique of recording and plotting time dependent flux over the phase or period of the orbit is called transit photometry (hereafter photometry). The photometry done on the EB system gives a wealth of information. The total flux as seen from the EB has a contribution from both the components of the system, the primary star (heavier) and the secondary star (lighter). The passage of an object in front of the other leads to partial blockage of the light coming from one of the objects, which causes dips in the brightness periodically based on the orbit of the EB. The primary eclipse, by definition, is when the primary star (in most cases the more luminous one) is behind the secondary (in most cases the less luminous one). The primary eclipse is, thus, in general deeper than the secondary eclipse. However, for cases, where the primary despite being heavier object is less luminous than the secondary, say for a white dwarf, primary eclipses will be shallower than the secondary. If both the primary and secondary eclipses are seen for the EB, the light curve will have double eclipses. It may not be always possible to see secondary eclipses in EBs by a moderate size telescope or due to a less efficient detection capability due to its smaller depth. The size of the dip in brightness expected during the transit can be estimated simply from the fraction of the brighter stellar disc covered by the fainter one (Haswell, 2010):

$$\frac{\Delta F}{F} = \frac{4\pi {R_B}^2}{4\pi {R_A}^2} \tag{1.8}$$

Here, F is the measured flux of the star and ΔF is the change in the flux during transit, $4\pi {R_A}^2$ and $4\pi {R_B}^2$ are the surface areas of the primary and secondary components respectively. Thus, the dip in the magnitude of the primary (or secondary star) depends on the size of the eclipsing companion. However, it also depends on the geometric alignment of the two stars as seen from earth. For an orbit parallel to the sky, i is 0°, a condition for face-on orbit and no transit will be seen in such a case. On the other hand, for an orbit perpendicular to the sky, i is 90°, a condition for edge-on orbit and transit will be seen in this case. If the smaller star is completely eclipsed by the larger one and if the larger star is hidden by the secondary when the smaller passes in front of it, constant amount of light will be blocked for that duration. This results in constant minima of the eclipse indicating $i \sim 90°$ whereas if the minima are no longer constant, it indicates that i should be less than 90° (Carroll and Ostlie, 2006). As seen in Fig. 1.1, t_a and t_b are the points of first contact and second contact (minimum light) respectively which is helpful in determination of radius of the larger star (primary) and the secondary is estimated by considering the time between first and third contact (t_c) (Carroll and Ostlie, 2006).

As seen in Fig. 1.1, the primary eclipse occurs when the smaller star transits the larger star between the points a and d. Though, the larger star is not fully hidden from view, a constant amount of area is still obscured. The secondary eclipse occurs when the larger star is occulted by the smaller, here in the figure between points e and h. The total eclipse duration is dependent on the size and also the inclination of the orbit.

Mandel and Agol (2002) have modelled the transit of a spherical star by a dark sphere. The analytic formulation valid for a star-planet system can be extended to a star-VLMS EB system as the VLMS objects are faint enough to hardly contribute any light of its own and can be well approximated as a dark

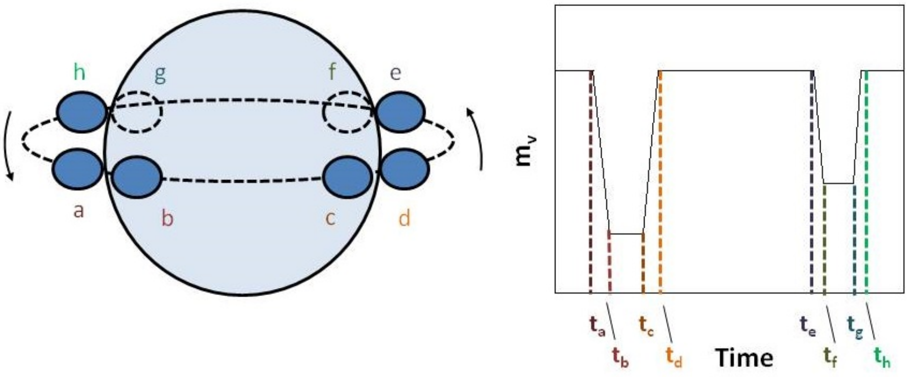

Figure 1.1: Light curve of the EB system seen from the observer point of view. The primary and secondary eclipses are indicated based on the points of contact.

sphere. Consider, d to be the separation between the two stars, r_1 and r_2 be radii of the two stars, $z = d/r_1$ is the normalized separation of the centers and $p = r_2/r_1$ is the ratio of the radii of two stars. The flux relative to the unobscured flux is F. The ratio of obscured to unobscured flux is given by Mandel and Agol (2002) as:

$$F(p,z) = 1 - \lambda(p,z) \tag{1.9}$$

where,

$$\lambda(p,z) = \begin{cases} 0, & \text{for } 1+p < z \\ \frac{1}{\pi}[p^2\kappa_0 + \kappa_1 - \sqrt{\frac{4z^2-(1+z^2-p^2)^2}{4}}], & \text{for } |1-p| < z \leqslant 1+p \\ p^2, & \text{for } z \leqslant 1-p \\ 1, & \text{for } z \leqslant p-1 \end{cases} \tag{1.10}$$

Here, $\kappa_1 = cos^{-1}[(1-p^2+z^2)/2z]$, $\kappa_0 = cos^{-1}[(p^2+z^2-1)/2pz]$. The transit data is modelled with this formulation for the regimes in and out of transit times. κ_0 and κ_1 along with p leads to determination of radii and i for the EB by photometry method.

1.4.2 Radial Velocity

Radial velocity is the line of sight velocity of the object as seen from Earth. The concept and the techniques used in its determination are discussed here.

1.4.2.1 Concept

The basic principle behind the ingenious method of RV comes from the simple physics of Doppler effect. For a non-relativistic case, any rest-frame photon of wavelength λ_o will be detected at a different wavelength λ by an observer depending on whether the source is moving toward the observer (blue shift) or away from the observer (red shift) as shown in Fig. 1.2.

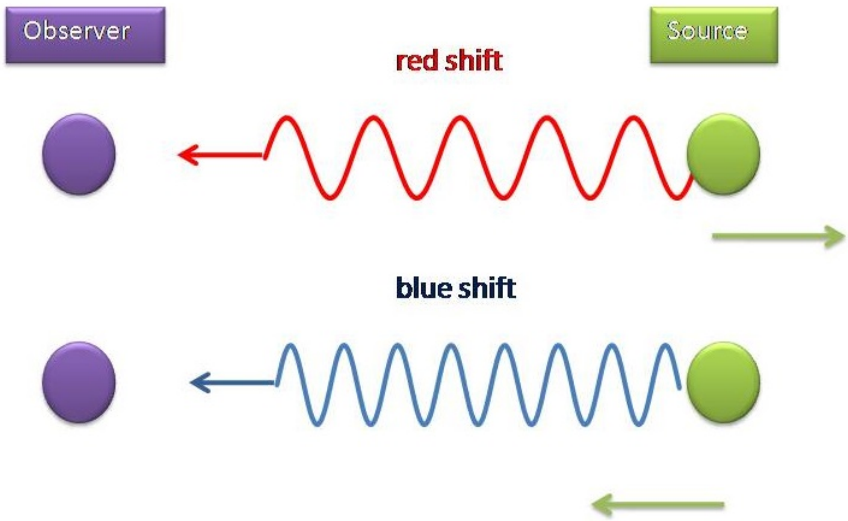

Figure 1.2: The spectral lines shift towards red or towards blue due to the Doppler effect as the source moves away or toward the observer.

This can be given in the form of an equation

$$\frac{v \sin i}{c} = \frac{\lambda - \lambda_o}{\lambda_o} \tag{1.11}$$

Here, v is the velocity of the source moving, i is the angle of inclination between the plane of the sky and the plane in which the source is moving, c is the velocity of light. Thus, $v \sin i$ is the RV of the source. Vogel in the year

1888 demonstrated the Doppler effect by photographically recording the displacement of lines in the stellar spectra for the stars which moved along the line of sight (Seager, 2010). This effect has been used as a powerful tool to study stellar kinematics, orbital parameters of stellar binary systems and to identify stellar pulsations. If the star happens to be in a binary, the RV of each component varies with time periodically.

The wavelength shift can be translated to RV shift in velocity space based on the Eqn 1.11. Sources for which spectra of one of the stars in binary are visible are known as single-lined eclipsing binaries and systems for which spectra of both the stars are visible are known as double-lined eclipsing binaries. The mapping of RV shift for a double-lined EB as a function of orbital phase is schematically shown in Fig 1.3. The smaller of the two stars is denoted in red colour and the larger of the two is denoted in blue. The corresponding RV curves based on their orbital phases are shown in the right side of the figure.

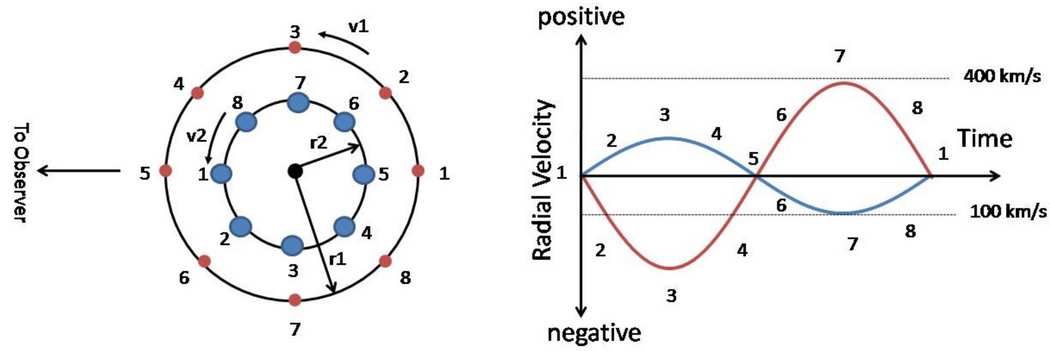

Figure 1.3: RV curve is shown for the orbit of a double-lined EB also known as SB2 as spectra for both the stars are seen. If spectrum from single star is seen, such systems are known as single-lined EB or SB1. Based on phase of orbit for the two stars, the RV curve varies with a maximum which equals the RV semi-amplitude.

Based on the orbital phase, the RV value varies leading to a sinusoidal curve having a RV semi-amplitude (K) given by (Seager, 2010):

$$K = \frac{2\,\pi\,G^{1/3}}{P}\;f(m)\;\frac{1}{\sqrt{1-e^2}} \tag{1.12}$$

$$\text{where } f(m) = \frac{m_2 \ \sin i}{(m_1 + m_2)^{2/3}}$$

is the mass function of the EB system (Kallrath and Milone, 2000). Here, P, e, G and i stand for orbital period, eccentricity of the system, gravitational constant and angle of inclination; m_1 and m_2 are masses of the two components in EB. Thus, the quantity we derive from RV measurements is the mass function. A knowledge of the primary mass (m_1) and $\sin i$ is needed to calculate the secondary mass (m_2). The former quantity can be derived by estimating the stellar parameters of the primary by high-resolution spectroscopy as discussed in Ch 3 while the latter one can be derived by photometry as presented in § 1.4.1 of this Chapter.

1.4.2.2 RV technique

The usage of RV technique in high-resolution spectrographs has gained momentum since the past half century for determination of masses of the components and the orbital parameters in EB systems as well as star-planet systems. The precision achieved with this technique has seen major improvement over the years. RV precision is dependent on the calibration techniques used in the spectrographs. In 1953, RV studies began with the usage of telluric lines (absorption lines present in the atmosphere of Earth) as the reference lines against which the stability of spectra was verified. A typical precision of 750 m s^{-1} was achieved with this technique by Griffin and Griffin (1973). The telluric lines were later replaced by hydrogen fluoride (HF) in a glass cell. Similar to telluric lines, HF lines provided absorption features in the stellar spectra and provided a calibration source but limited to a small wavelength range of 50 $\mathring{A}$ (Campbell *et al.*, 1979). To broaden the range of wavelength calibration used and improve the precision of RV, emission spectrum from calibrating lamps such as thorium argon (ThAr) was used (Baranne *et al.*, 1996). Currently, two calibration techniques are being used for precise RV determination which are described in the following sections.

Iodine cell technique: In this technique, a glass cell is filled with iodine in the vapour form and maintained at a constant temperature and pressure. This cell is inserted in the light path; in front of the slit of the spectrograph. This leads to a dense forest of molecular absorption between the wavelengths of $5000-6200\mathring{A}$ (Seager, 2010) superimposed on the stellar spectra. Observation of the iodine spectrum superimposed on the spectrum of a featureless star such as B type star is carried out with a Fourier Transform Spectrometer at the beginning and end of each night. Valenti, Butler and Marcy (1995) devised a technique where the PSF of the star is modelled as a sum of Gaussians and a wavelength solution is generated for the superimposed spectra with no Doppler shifts for the reference iodine spectrum. In the next step, the process is repeated by taking the spectra of the program star with the iodine cell. The wavelength solution generated in the previous step is applied at this step and Doppler shifts are calculated with respect to the reference spectrum.

Simultaneous Thorium-Argon Reference technique: The simultaneous Thorium-Argon (ThAr) reference technique was introduced by Baranne *et al.* (1996), which uses ThAr lamp as the calibrator source. Along with stellar spectra on one of the channels, a reference spectra from ThAr lamp is simultaneously obtained in a similar optical path onto the second channel. ThAr lamp is a laboratory source and the spectra obtained can be wavelength calibrated from pre-determined solutions. Since, the optical path seen by both the channels is same, the wavelength calibration solution of ThAr is applied to the stellar spectra (Seager, 2010). ThAr spectra are taken after fixed intervals of time in the duration of the observation night ($6-8$ in number) to determine the drift in the spectra due to minute changes in the temperature and pressure (see Chakraborty *et al.* (2014) for details). Wavelength shifts obtained due to the above mentioned reasons are then compensated. High SNR stellar spectra in the form of a zero RV mask is used to compute the RV value from each wavelength calibrated stellar spectra by the technique of cross-correlation (See § 2.6 for details). Currently for high SNR, RV measurements of sub m s^{-1} can be obtained by ThAr simultaneous reference method (Lovis *et al.*, 2006). This has not only enabled the discovery of substellar masses, like brown dwarfs, but also sub-Jupiter-sized planets (Marcy and Butler, 2000). This technique has been successfully used in many spectrographs, namely, High Accuracy Radial velocity Planet Searcher (HARPS) installed on ESO 3.6 m telescope at La Silla Observatory, Chile (Pepe *et al.*, 2003), ELODIE at Observatoire de Haute Provence (OHP), France (Baranne *et al.*, 1996), Spectrographe pour l'Observation des Phénoménes des Intérieurs stellaires et des Exoplanétes (SOPHIE) at OHP (Bouchy and Sophie Team, 2006), CORALIE at La Silla (Udry *et al.*, 2000).

Comparison of the two methods: These two methods have their own share of advantages and disadvantages. Iodine cell technique has an advantage of having thousands of iodine absorption lines which are superimposed onto the stellar spectra by sharing a common stellar path leading to better estimation of drifts in the spectra occurring due to external factors. However, since iodine cell has its major lines clustered in the visible band, it is difficult to study stars which have peak emission towards the red and infrared wavelength region. Moreover, the absorption cell also absorbs 30 % of the incoming photons (Mason, 2008). For the case of ThAr calibration technique, there are thousands of emission lines spread over a broader wavelength region, out of which 3800 – 6800 Å is best utilized in most of the spectrographs (Chakraborty *et al.*, 2014). Broad wavelength coverage is necessary to improve the RV precision capabilities. There is no loss of photons by absorption as both the spectra are observed onto two different channels. However, the entire instrument needs to be installed in an isothermal and mechanically stable environment to account for drift in spectra due to external conditions (Mason, 2008). Therefore, the instrument design becomes more complicated than that using the iodine calibration method.

Currently, we are using the ThAr simultaneous calibration method at the Physical Research Laboratory Advanced Radial velocity Abu sky Search

(PARAS), and have achieved high precision by initiating RV studies (Chakraborty *et al.*, 2014). (For details refer Ch 2). With our EB program, we aim to deduce the masses and radii of the components in the EB and also infer the orbital evolutionary status of the EB based on its orbital parameters.

1.5 Tidal interaction in EBs

F-type primaries with M-type secondaries (hereafter F+M binaries) are often discovered in transit surveys that are primarily designed to search for transiting planets (e.g. Bouchy *et al.* (2005); Beatty *et al.* (2007)). Over the last few years a handful of F+M binaries have been discovered and their properties determined (e.g. (Pont *et al.*, 2005a,b, 2006); Fernandez *et al.* 2009). F-type stars are typically fast rotators with a tenuous convective zone. Bouchy *et al.* (2011a) suggest that there is a higher probability of M dwarfs orbiting F-type primaries, in contrast to G-type primaries. Bouchy *et al.* (2011a,b) further suggest that for a massive companion to exist around a primary star, the total angular momentum must be above a critical value. If a primary star has a shorter spin period than the orbital period of the system (as in the case for G-type stars), the tidal interactions between the two stars will cause the secondary companion to be eventually engulfed by the primary. However, this is less likely to occur among fast rotating F-type stars which have weaker magnetic braking and can avoid the spin-down caused due to the tides raised by the massive secondary. This helps the companions around F-type stars to survive rapid orbital decay due to loss of angular momentum. Tidal evolution may be studied by measuring the degree of circularization of the orbit and the level of synchronization of the rotational velocities. In a sample of 95 binary systems studied by Torres, Andersen and Giménez (2010), 44 were found to be eccentric. Stars were studied separately for the ones having radiative envelopes or convective envelopes. Orbits for short period stars were found to be circular while the longer period stars had a range of eccentricities with no case of eccentric orbit below 1.5 d. Torres, Andersen and Giménez (2010) have also noted that stars with a convective envelope have circular orbits for some longer period orbits in comparison with the ones having radiative envelopes. The other important parameter in understanding tidal evolution is comparing the rotational period of the stars with the values expected from synchronization with the orbital period (Zahn, 1977). The speed at which the stars spun up or spun down in the course of evolution will depend on the relative radii (ratio of orbital semi-major axis and the radius of the star, a/R_*) of the stars. The overall tendency in binaries is thus to spin up the convective stars by increasing their rotational velocities and to slow down the ones having radiative envelopes by decreasing their rotational velocities. Thus, the evolution of binary stars would be different relative to their single counterparts.

1.6 Mass-Radius relation in VLMS

M-R relation has been an important parameter studied by astrophysicists to verify the stellar evolutionary models. The M-R relation as shown in Fig. 1.4 starting from Sun to gaseous planets can be summarized in a simple polytropic relation, $R \propto M^{\frac{1-n}{3-n}}$ (Chabrier *et al.*, 2009). LMS objects are shown in the Fig 1.4 plotted on theoretical isochrones (line connecting points of same age) of 1 Gyr, 5 Gyr and 10 Gyr (Baraffe *et al.*, 1998). As shown in the figure, LMS from Sun to the HBMM have a polytropic index, n $\sim$ 3 for stars with radiative cores to n = 3/2 for stars with convective cores having masses below 0.4 $M_\odot$. A decrease in polytropic index leads to decreasing central pressures and densities. The polytropic index, n, for Jupiter mass objects, is close to 1. Further down the mass regime, for the case of planets, the index n = 0 indicates homogeneous incompressible matter. For stars with a combination of a classical ideal gas equation of state (EOS) and the quasi-static equilibrium condition, yields $R \propto M$ dependence. Since, surface density varies inversely as a third power of radius, with a decrease in mass, the surface density increases leading to the electrons becoming degenerate. The onset of degeneracy corresponds to the HBMM.

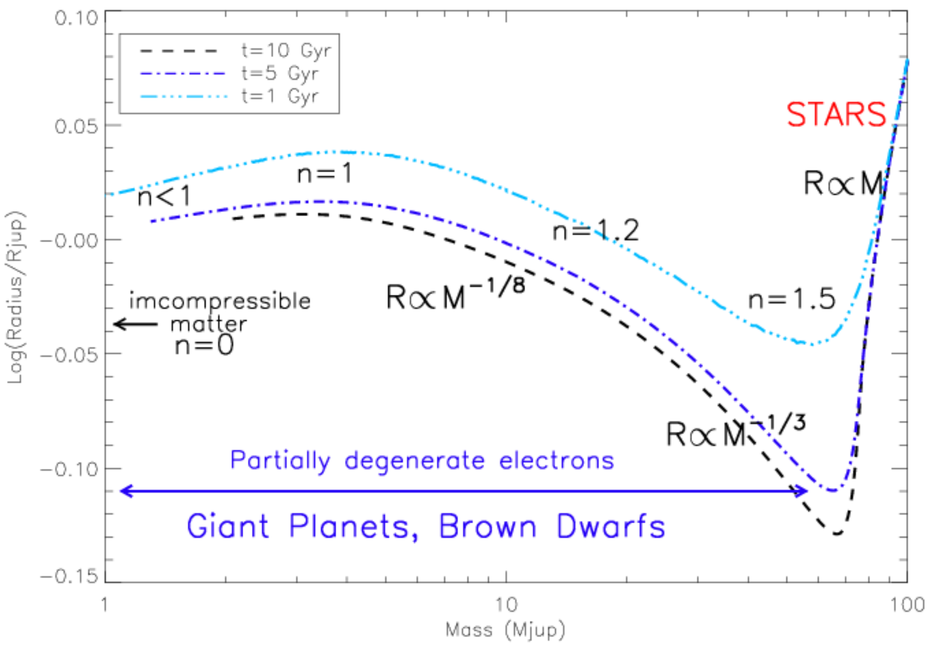

Figure 1.4: M-R relationship from Sun to Jupiter for three different isochrones. Characteristic values of the polytropic index n are indicated. Image credit (Chabrier *et al.*, 2009)

Through careful photometry and spectroscopy, it is possible to obtain radii and masses of individual components with accuracies as high as 1 % for double-lined EBs. Such precise measurements impose strong constraints on stellar evolution models. López-Morales (2007) has compiled a sample of 48 LMS which have masses in the range of 0.092 to 0.960 $M_{\odot}$. The precision in the mass and radius measurements would be different depending on the brightness of the stars and measurement technique employed to derive the parameters. For stars with masses below 0.5 $M_{\odot}$, the measured radii appear to be $20-30\%$ larger than predicted (López-Morales, 2007).

The techniques of RV and transit photometry have been applied to hundreds of EBs studied in literature (Andersen, 1991; Torres, Andersen and Giménez, 2010), and references therein. A M-R plot of the studied low-mass stars in detached EBs is provided in Fig 1.5. The figure also shows objects that have reported error bars in both masses and radii below 3% (Ribas *et al.*, 2008). The systematic offset of $5-10\%$ between the observations and the 1

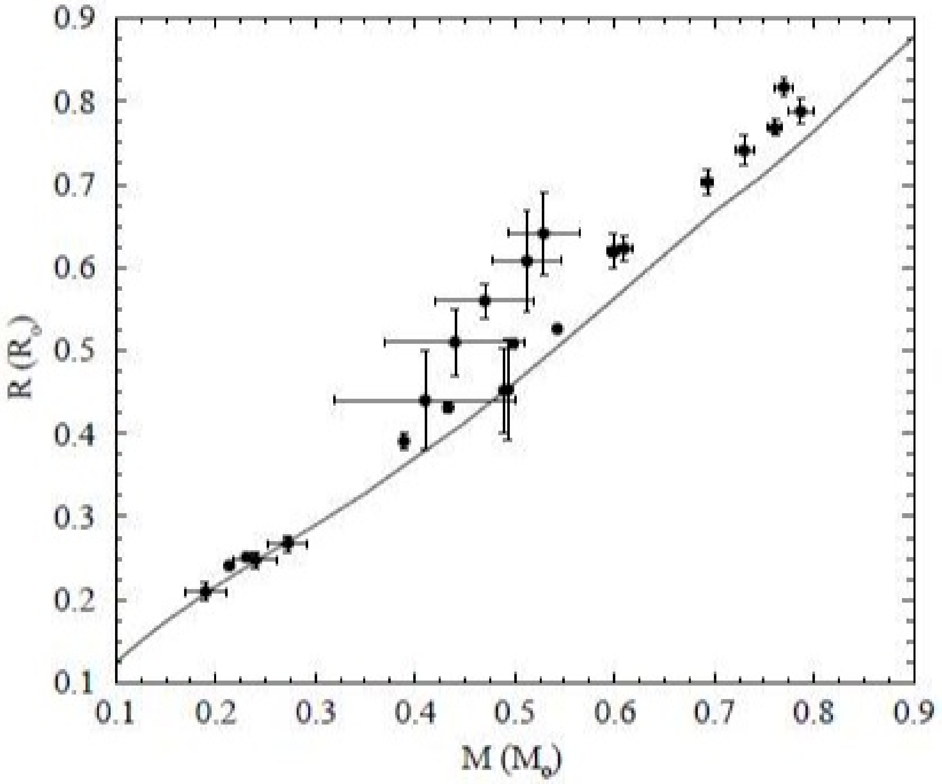

Figure 1.5: M-R plot for low-mass eclipsing binary stars with empirical determinations. Only few of the stars have uncertainties below 3%. The solid line represents a theoretical isochrone of 1 Gyr calculated with the Baraffe *et al.* (1998) models. Image credit (Ribas *et al.*, 2008)

Gyr isochrone from the models of Baraffe, Chabrier and Barman (2008) may be noticed. Stars having masses less than 0.4 $M_{\odot}$ have still not been studied extensively for their M-R relation (Triaud *et al.*, 2013) as rightly seen from Fig 1.5, in which the regime below 0.4 $M_{\odot}$ is sparsely populated. Moreover, objects close to the mass range of $0.3 - 0.4$ $M_{\odot}$ occur in the transition boundary regime between the partially radiative and completely convective means for energy transport (Chabrier and Baraffe, 2000). Thus, this region needs more careful inspection, as the underlying physics used in the models for this mass regime is poorly understood. Thus, in this work, stars having masses between $0.08 - 0.4$ $M_{\odot}$ were chosen for evaluating the M-R relationship.

The limited number of high-resolution spectrographs dedicated for studying VLMS in EBs has led to scantily made high precision studies. The theoretical models require improvement at each stage based on the observational updates to rectify the discrepancies associated with them. A few plausible reasons were suggested in the literature in order to account for the discrepancies.

1.6.1 Stellar magnetic activity hypothesis

Stellar activity hypothesis suggests that the afore-mentioned disagreement between theory and observations may be caused by the degree of magnetic activity in stars: strong magnetic fields inhibit convection leading to inflate stellar radii (López-Morales and Ribas 2005; Mullan and MacDonald 2001). As mentioned earlier, convection is the most efficient mechanism of energy transport in the low mass regime. The topology of magnetic fields in the interior of VLMS changes for stars of masses around 0.4 $M_{\odot}$. Objects having mass above 0.4 $M_{\odot}$ exhibit a toroidal field and objects below this limit are dominated by poloidal field showing some modest level of differential rotation. Baraffe *et al.* (1998) presented evolutionary models for low mass stars (from 0.075 $M_{\odot}$ to 1 $M_{\odot}$ and metallicities between $[M/H] = 0$ to $[M/H] = -0.5$) and were able to derive mass-M_V (M_V is magnitude in V band) and mass-M_K (M_K is magnitude in K band) relations in good agreement with the the empirical relations derived observationally. However, the uncertainties do exist for stars having temperatures below 3700 K (Baraffe *et al.*, 1998). Due to lack of observational data, the effect of magnetic activity on the M-R relation is not examined for stars having temperatures below 3700 K and hence smaller masses (for the case of M dwarfs). As discussed in § 1.5, tidal interactions in close binaries causing orbital synchronization is the distinctive feature occurring in VLMS evolving in binaries as compared with those evolving as single objects (Ribas *et al.*, 2008). As pointed out by the studies of López-Morales (2007) and references therein, magnetic activity has been found to be correlated with stellar rotation for single stars while there exists no such correlation for binaries (Fleming, Gioia and Maccacaro, 1989). All single stars are known to be slow rotators whereas the VLMS which occur as binaries can have rotational velocities ranging from 2.0 km s^{-1} to 130 km s^{-1}. Many of the fast rotating binaries have strong indications of X-ray activity from the corona and the H_α activity from the chromosphere (Chabrier, Gallardo and Baraffe, 2007). Thus, the magnetic activity level for binaries can be 100 times more than the single stars (Mullan and MacDonald, 2001).

1.6.2 Starspots

Starspots are dark regions seen on the observable photosphere of the star due to the presence of local magnetic fields which suppress the convective motion and thereby energy transport from the stellar interior to the surface (Strassmeier, 2009). López-Morales and Ribas (2005) propose a scenario based on energy conservation mechanisms in spot-covered areas. Chabrier, Gallardo and Baraffe (2007) concluded in their study that the inhibition of convection in fast rotating stars and the presence of stars spots on the stellar disk could affect the stellar models. Cool starspots too are reflective of the inhibition of energy by convective transport in the interior of the star. Let F_* and F_s be the flux emerging from the surface of the star, one without spots and the other covered by starspots by a factor β ($\beta = S_s/S_*$). Here, $F_* = \sigma T_{\text{eff}*}$, where $T_{\text{eff}*}$ is surface temperature of star associated with a spot-free star. Thus, the total flux emitted by the star is given by (Chabrier, Gallardo and Baraffe, 2007)

$$F = (1-\beta)F_* + F_s < F_s \tag{1.13}$$

Hence, the surface of star covered with spots will have a lesser effective surface temperature than the one free of starspots. A similar equation can be written for luminosity

$$L = (1-\beta)4\pi R^2 \sigma T_{eff}^4 \tag{1.14}$$

Here, R and T_{eff} are the radius and effective temperature of the star in presence of starspots. With a β parameter of 0.3, the observational M-R relation can be fitted to a better agreement. Moreover, if we consider a β value of 0.3, it indicates that almost half of the stellar disk is covered by spots that are cooler than the photosphere by 15% (Ribas *et al.*, 2008). The current theory is still into the developmental stage and more number of samples are needed to validate it.

1.6.3 Stellar Metallicity hypothesis

This hypothesis suggests the dependency of metallicity on the amount of inflation in the observed radius. Berger *et al.* (2006) in their study find that the disagreement is larger among metal-rich stars than metal-poor stars. They conclude that current atmospheric models have missed some opacity components which may lead to a larger radii for stars having higher metallicity. Direct investigation of the abundances of several elements from the M dwarfs is difficult on account of several complex molecular bands present in the interior of such stars. Below $T_{\rm eff} \leqslant 4000$ K, most of the hydrogen in the stellar atmosphere is locked into H_2, and most of the carbon in CO. Oxides such as TiO, VO, H_2O and metal hydrides such as FeH, CaH, MgH are also present (Chabrier *et al.*, 2009). Due to the presence of hydrogen in molecular form, the radiative opacity rises and convection plays a major role for transport mechanism inside the star (Chabrier *et al.*, 2009). An improper modelling of the molecular absorption coefficients due to incorrect abundance analysis results in an erroneous M-R relationships (Berger *et al.*, 2006). López-Morales (2007) showed that stars with $[Fe/H] > -0.25$ show larger deviations in the radius measurements from the models than stars with $[Fe/H] > -0.25$. However, this issue needs to be further investigated. Therefore, it becomes imperative to detect and study more such systems and determine their masses and radii to very high precision.

1.7 Objectives of the study

The main objectives of the work presented here are as follows:

- There are several discrepancies described above in the observationally measured radii of VLMS and the ones derived from the theoretical models. Previous high precision studies (accuracies better than $5 - 10\%$)

involving determination of masses and radii of objects in the mass range of $0.08 - 0.4$ $M_\odot$ have been limited. Thus, the aim of the thesis work is to determine physical parameters such as masses and radii of VLMS in this mass range. More samples will help eliminate any observational bias pertaining to study of objects in this field and help to resolve the aforementioned discrepancies. We will look at the current work done in this thesis in the light of work done by others in this field so far. This requires careful selection of stars from various photometry catalogues suitable to be observed with the available telescope and instrument facilities (Details presented in Ch 2).

- RV method is the primary technique employed to study the EBs for this research work. Making high-resolution spectroscopy observations, performing echelle data reduction and RV analysis are integrated aspects of the thesis work. The analysis techniques require constant improvement to suit better RV precision obtained for fainter and fast rotating stars.

- Photometry of the target gives insights on the angle of orbital inclination and radii of both the components providing us a complete picture of the system. The programme involves conducting photometry on the sources from ground-based telescope or retrieving archival data on photometry measurements if available.

- The determination of spectroscopic properties of the host star is very essential to impose better constraints on determination of mass and radius of the primary star. An accurate determination of stellar parameters of the primary host star will lead to precise characterization of the companion. For, the case of single-lined EBs, where the companion is a VLMS object bound to a F, G, K type primary, precise characterization of the host star will lead to better accuracies on the masses and radii determined for the VLMS objects.

The objectives listed above are accomplished using the measurements from the high-resolution spectrograph PARAS attached at the PRL 1.2 m telescope and the data analysis techniques which are described in brief in the following Chapters.

1.8 Overview of the thesis Chapters

The thesis contains the following Chapters:

In **Ch 2**, a brief description of the spectrograph and its optical layout are given. The general criteria adopted for candidate selection and photometry catalogues from where the sources are shortlisted are also discussed. The observation strategy followed for efficient utilization of time for observing these candidates is given. The data extraction and analysis methodology developed for obtaining the RV results are also described in detail in this Chapter.

Ch 3 deals with the methods used to determine stellar properties based on the spectral analysis. We used two main methods of stellar property estimation, one is the spectral fitting method and the other is the equivalent width fitting method. The Chapter describes in detail these methods, the in-house designed software pipeline and the results obtained from it.

Ch 4 describes results on three EB systems (F+M) selected from *STEREO* and *SuperWasp* photometry catalogues. RV and photometry measurements made on the sources along with the analyses and results obtained for the same are given in this Chapter.

Ch 5 describes results on one EB system (K+M) selected from *SuperWasp* photometry catalogue. Similar to the previous Chapter, observations, data analysis technique and results obtained on the source are covered as a part of this Chapter.

The summary and scope for future work are discussed in **Ch 6**.

Chapter 2

Observations and Data Analysis Techniques

2.1 Introduction

The primary objective of the thesis work is to determine physical parameters of very low mass stars (VLMS) right up to the mass limit of hydrogen burning. A statistically significant sample of VLMS is required to resolve the discrepancies encountered in their evolutionary models as discussed in Ch 1. This study can be done by observing VLMS in eclipsing binaries (EBs). VLMS as a part of EB systems are often detected in transit surveys which are primarily targeted to look for exoplanets. Study of Mass-Radius (M-R) relation of VLMS requires high precision measurements of the stellar parameters on large samples of such stars. To address these problems, candidates suitable for radial velocity (RV) and photometry follow-up are shortlisted from existing photometric archives (catalogues). Deducing the radius of both the components of the EB and angle of inclination (i) by means of photometry form a key area in the study of EBs. RV measurements for this thesis work have been undertaken with the Physical Research Laboratory Advanced Radial velocity Abu sky Search (PARAS) spectrograph (Chakraborty *et al.*, 2014).

In this Chapter, PARAS spectrograph is described in brief, including key elements of the optical design. The observation catalogues used for shortlisting PARAS EB candidates are discussed. The Chapter also gives a description of the observation procedure followed at the observatory. The data reduction and analysis pipeline (PARAS PIPELINE) is also discussed here.

2.2 PARAS

PARAS is an optical fiber-fed high-resolution (R $\sim$ 67000) cross-dispersed echelle spectrograph commissioned at the Mount Abu 1.2 m telescope in India (latitude: $24^\circ\ 39'\ 10''$N, longitude: $72^\circ\ 46'\ 47''$E, altitude 1680 m). The spectrograph has a spectral coverage of $3800 - 9000$ $\AA$. However, for precise RV measurements, wavelength range of $3800 - 6800$ $\AA$ is utilized with Thorium Argon (ThAr) simultaneous calibration method. The spectrograph is maintained in a temperature-stable (RMS of 0.01°C at 25°C) and pressure-stable environment (maximum variation of 0.06 mbar in one night of observation). Fig. 2.1 shows the optical layout of the spectrograph.

Primarily, the spectrograph resolving power is determined by the pupil diameter illuminating the grating/echelle ruling area and the size of the slit width. There is no physical slit in the PARAS. Instead, the fiber tip is re-imaged at the slit position of the spectrograph. This has a clear advantage in terms of stability of the spectrograph-PSF (point spread function), since it eliminates the PSF variations due to micro changes in the slit width over a long period of time, making it extremely suitable for precision RV measurements.

The pupil diameter of the spectrograph is defined as 100 mm and it is a white pupil design; in which the dispersive element pupil is re-imaged on the entrance pupil of the camera, a design proposed and demonstrated by Baranne (1972).

To achieve a spectrograph resolving power of 67,000, the following designs were considered:

(a) A 50 μm core fiber is employed, which corresponds to 2 arcsec at the focal plane of the 1.2 m telescope with a F/4.5 beam. (The F/13 beam

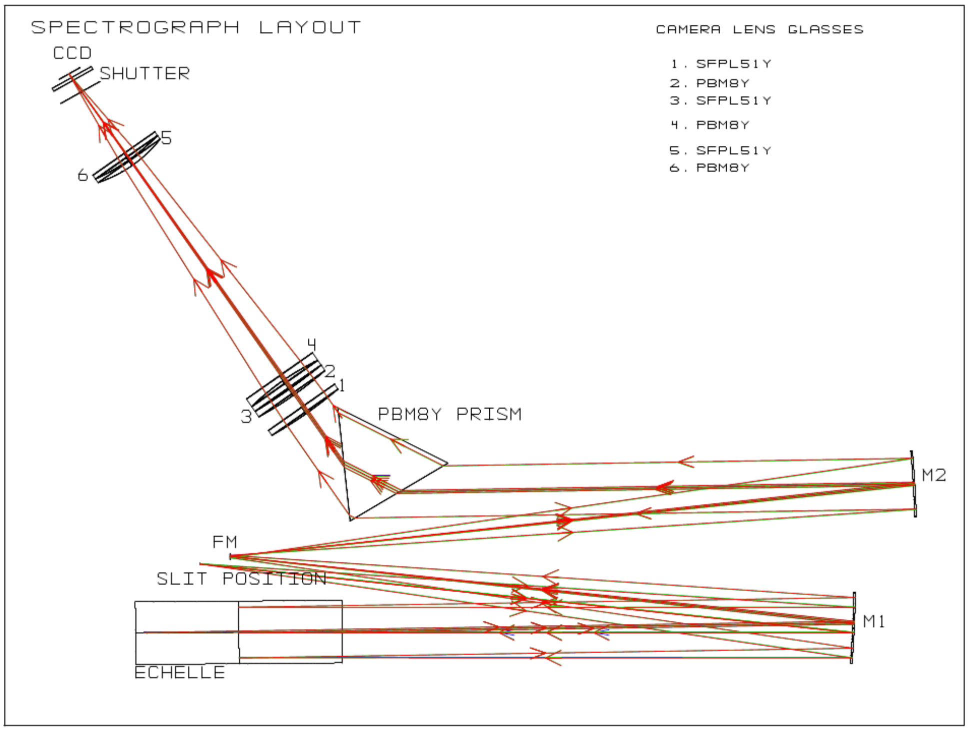

Figure 2.1: The optical layout of the PARAS spectrograph consisting of reflective collimator mirrors, echelle grating, prism and camera optics.

is pre-converted to F/4.5 using a focal reducer).

(b) The 50 μm core fiber tip is re-imaged at the slit position with F/4 converted back to F/13 optics taking into consideration the focal ratio degradation (FRD).

(c) The F/13 beam from the slit position coincides with the focal position of the off-axis mirror, M1, thus converting it into 100 mm pupil diameter.

(d) This 100 mm beam illuminates an R4 echelle grating with blaze angle of 75° in a quasi-Littrow position. Thus, the required physical size of the echelle grating is 100 mm $\times$ 400 mm. Actual size used here is 200 mm $\times$ 400 mm. The groove spacing is 31.6 lines/mm.

(e) The dispersed light from the echelle is reflected back by M1 and is folded by the fold mirror (FM) which is again picked up by the second off-axis mirror, M2, having the same focal length as that of M1. This makes a parallel beam of dispersed echelle light of 100 mm in diameter. Both M1 and M2 have a F number of F/13.

(f) The cross-disperser element, a prism made of the material PBM8Y, is kept in the optical train such that its dispersion axis is perpendicular to that of the echelle grating as it receives the 100 mm parallel light beam from M2. This helps in separating the echelle orders in a perpendicular direction to the echelle dispersion direction.

(g) The echelle dispersed and prism cross-dispersed beam is imaged by a F/4.5 camera lens system consisting of a singlet, triplet, and a doublet (as shown in Fig 2.1) onto the CCD.

(h) The spectral coverage designed for the spectrograph is from 3800 Å to 9000 Å. The spectrograph is designed for simultaneous two fiber spectroscopy between 3800 Å to 6800 Å and single fiber spectroscopy over the entire wavelength range. Two 50 μm core fibers that are separated by 180 μm will produce two spectra on the CCD, which will be separated by 255 μm. The CCD, 4096 $\times$ 4096 pixel array with 15 μm pixel size does the job required. The E2V CCD, 231-84 deep-depletion and back-thinned CCD cooled at $-115°$C using a Helium close-cycling cryocooling unit is used. The unit has a special ability to produce less than 0.1 Å vibrations on the CCD array for the requirement of stabilized PSF. The quantum efficiency of the CCD is greater than 85% between $4500 - 7500$ $\AA$. Two spectra of the same echelle orders are separated by 17 pixels. The spectra of the consecutive orders at blue end is separated by $\sim$ 74 pixels at 3800 Å and $\sim$ 32 pixels at 6900 Å.

(i) The above-mentioned combination of the different elements of the spectrograph gives us an average resolving power of 67,000 between echelle orders 160 (red end) and 87 (blue end). This takes into account of the

F/4.5 camera PSF which has a FWHM of 4.2 pixels on the CCD.

The total efficiency of the spectrograph, which includes the telescope, optical fibers and the spectrograph losses is 6% (Chakraborty *et al.*, 2014). The details of the individual optical components, along with their transmission losses (for lenses) and reflectivity (for mirrors) can be found in Chakraborty *et al.* (2010), Chakraborty, Richardson and Mahadevan (2008) and Chakraborty *et al.* (2014).

2.3 VLMS science with PARAS

PARAS is capable of high precision RV studies of the order of $1 - 2$ m s^{-1} for SNR > 150. As shown in Fig. 2.2, observations on a bright G9 type star, σ Dra (m$_v \sim 4.8$) (Wright *et al.*, 2008; Johnson *et al.*, 2006) over a period of 7 months have demonstrated a RV precision of 1.7 m s^{-1} (rms). For one night of observations, if the data is binned, the scatter reduces to 1.0 m s^{-1}.

The RV precision limited by photon noise errors is given by Hatzes and Cochran (1992)

$$\sigma_{\rm RV} \sim 1.45 \times 10^9 (S/N)^{-1} R^{-1} B^{-1/2} \text{ m s}^{-1} \tag{2.1}$$

where S/N is the signal-to-noise of the spectra, while R and B are the resolving power and wavelength coverage of the spectrograph in angstrom (Å) respectively. The photon noise is computed from the full information content of the spectra, using the method prescribed by Bouchy, Pepe and Queloz (2001). For the star σ Dra, the photon noise estimated is 0.95 m s^{-1}. Based on the photon noise, Table 2.1 lists the $\sigma_{\rm RV}$ value obtained with PARAS spectra on stars of different magnitude ranges.

As seen from Table 2.1, though PARAS is easily capable of looking for Neptune-like planets across Sun-like stars with the current RV precision, the precision degrades for stars having fainter magnitudes and higher temperatures. Bouchy, Pepe and Queloz (2001) defined a quality factor Q that represents the quality and spectral line richness of the spectrum. It was shown

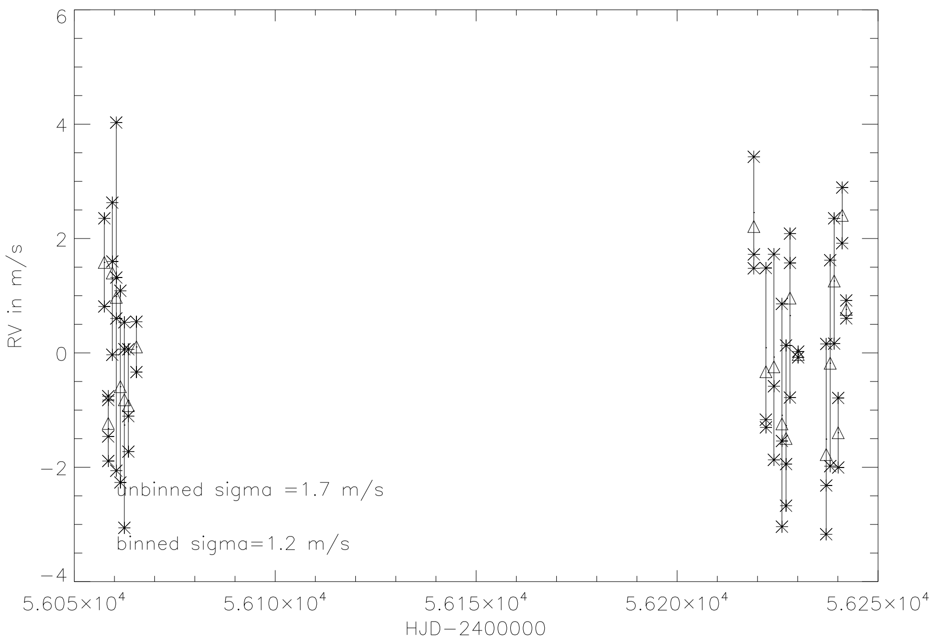

Figure 2.2: σ Dra observed with PARAS over a period of 7 months from May 2012 to Nov 2012. The star has a magnitude of 4.8 in V-band and a spectral type of G9. The asterisks are the individual data points and the open-triangles are the velocities of the binned data (mean of the three visits per night) and the lines show the RV variations per night.

Table 2.1: RV precision with PARAS for 1800 s exposure time

Visual Magnitude Range (mag)	PARAS RV precision (m s^{-1})
< 6.5	$1 - 2$
$7 - 8$	$3 - 7$
$8 - 9$	$7 - 10$
$9 - 10$	$12 - 15$
$10 - 11$	$15 - 35$

that Q deteriorates with increasing rotational velocity thereby increasing the RV uncertainty. For instance, a F2-type star with a rotational velocity of 40 km s^{-1} has a RV uncertainty 10 times larger than one that is rotating at

4 km s^{-1}. However, stars having VLMS or brown dwarfs as companions induce relatively larger RV shifts on their respective host stars. Such stars form the most suitable targets for pursuing VLMS science with PARAS. Therefore, we focus on F type sources having magnitudes in the range of 8 – 10 which are largely unexplored with high precision RV observation.

2.4 Photometry catalogues

As a part of the sample selection, a careful scrutiny of objects for the PARAS EB programme was carried out. The candidates were chosen from star catalogues from extensive space-based and ground-based photometric surveys like *STEREO*, *SuperWasp* and *Kepler* which looked at thousands of stars for transit signature. A brief description of each of the space-based or ground-based photometric survey is given as follows :

2.4.1 *STEREO*

STEREO, Solar Terrestrial Relations Observatory, are two spacecrafts (A & B) primarily dedicated to look at Sun and it's environment. The Heliospheric Imager (HI-1) on the Ahead spacecraft (HI-1A) has been used to study variability of stars up to 12 mag (Wraight *et al.*, 2011). The analysis of the light curves of several stars which were observed as a part of the *STEREO* programme has led to the discovery of several exoplanet and EB candidates. As reported in Wraight *et al.* (2011), the HI-1A has a field of view of 20° × 20° centred at 14° away from the Sun, where the solar F-corona is the dominant large-scale structure. The imager (CCD) of HI-1A has a focal length of 78 mm and a plate scale of 35 arcsec/pixel. Since, the images are 2 × 2 binned, the image size post binning is 70 arcsec. The filter used for observations is an R band (6300 – 7300 Å). A single frame has an exposure time of 40 sec and a combination of 30 frames including the time gaps between consecutive frames leads to generation of one frame every 40 minutes. The limit of observations is down to 12^{th} mag. About 650, 000 stars have been recorded with magnitudes brighter than 11.5, with almost 75, 000 of these being brighter than mag 9.5. *STEREO* has a data analysis pipeline developed (Sangaralingam and Stevens, 2011) and the final outcome of the entire exercise resulted in the release of a catalogue of 263 EBs. Some sources from this catalogue are shortlisted for making observations by PARAS as some of them are listed as potential candidates that host VLMS.

2.4.2 *SuperWasp*

SuperWASP (SW) is an extra-solar planet detection programme hosted by the joint collaboration between eight academic institutes located in the United Kingdom [1]. SW consists of ground-based robotic observatories and eight wide-angle cameras covering both the hemispheres of the sky. SW-N is located on the island of La Palma among the Isaac Newton Group of telescopes (ING) and SW-S at the site of the South African Astronomical Observatory (SAAO). The telescopes are aligned such that they are centred at +28° of declination. Different Right Ascension fields are observed with 1 hour increments of local sidereal time (Street *et al.*, 2003). The SW observatories use Canon 200-mm F/1.8 lenses attached with an e2V 2 × 2 back illuminated CCD having a field of view of 7.8° × 7.8°. The operational wavelength band is the entire V band covering stars having magnitudes between 8 to 15. Stellar exposures are kept at 30 s with a 4 s readout (Christian *et al.*, 2005; Pollacco *et al.*, 2006). An automated `FORTRAN`-based pipeline combined with shell scripts and several `STARLINK` packages are developed to detect transit signatures. Each science exposure is bias-subtracted, dark-corrected, flat-fielded before computing the astrometric solution (Pollacco *et al.*, 2006). Though, SW has been primarily aimed to look for exoplanet transit signatures, shortlisting sources with a relatively larger eclipsing depth gives a fair chance for locating an EB (Street *et al.*, 2007; Christian *et al.*, 2006; Lister *et al.*, 2007; Clarkson *et al.*, 2007; Kane *et al.*, 2008). (Refer § 2.5 for selection critera of the sources.)

[1] www.superwasp.org

2.4.3 *Kepler*

Kepler is a space observatory launched by NASA on March 7, 2009 to discover Earth-like planets orbiting other stars. Along with the usual target list of potential exoplanet host stars, *Kepler* also published a catalogue of eclipsing binary candidates (Koch *et al.*, 2007). The mission is designed specifically to look at around 100, 000 stars for transits in the region above the galactic plane looking down at the Orion arm of the Milky Way galaxy (Borucki *et al.*, 2009). It is basically a Schmidt telescope design with a 0.95 m aperture and a 105 degree^2 field-of-view (FOV) [2] (Borucki *et al.*, 2007). It continuously monitors the same field for more than three years to look for Earth-like planets orbiting in the habitable zone of the host star. The spacecraft consists of a photometer with a soft focus which has a simple purpose of differential photometry instead of capturing sharp images. The photometer comprises of an array of 42 CCDs each having 1024 $\times$ 2200 pixels with a size of 25 $\times$ 50 mm. Science exposures are integrated for 30 minutes and are read out every three seconds to prevent saturation (Swam *et al.*, 2007). The instrument has a spectral bandpass from 4000 Å to 8500 Å (Borucki *et al.*, 2007). The aim was to look at the sources which have been flagged as 'EB' in the *Kepler* catalogue. However, most of the sources studied from *Kepler* are relatively faint and none of the candidates could make upto the final selected list of PARAS EB candidates.

2.5 Candidate selection

A careful shortlisting of 10 candidates was made by us from the $\sim$ 200 candidates listed in the catalogues from the above mentioned surveys ((Wraight *et al.*, 2011, 2012; Street *et al.*, 2007; Christian *et al.*, 2006; Lister *et al.*, 2007; Clarkson *et al.*, 2007; Kane *et al.*, 2008), www.archive.stsci.edu/kepler/). The selection criteria are based on :

[2] www.kepler.nasa.gov

- Observability of a source based on its coordinates in the non-monsoon months between October-May of the observing season at Mt. Abu.

- Spectral types from F to K type; the reason is that these sources have sufficient number of spectral lines for cross-correlation technique to be accurate enough while determining stellar RVs. If the number of spectral lines used for the cross-correlation is insufficient, there will be a degradation of RV precision.

- Magnitudes of sources brighter than $\sim$ 11 in the V-band are selected. This is the limit of observations for PARAS spectrograph in conjunction with the 1.2 m telescope.

- The current interest being VLMS, candidates having an upper cut-off for the transit depth as $\sim$ 35 mmag are chosen in order to avoid samples having massive secondaries as companions. This criterion is relaxed for a few of the sources that were likely potential hosts for VLMS objects (Wraight *et al.*, 2012). The lower limit cut-off of the transit depth while shortlisting candidates is kept at $\sim$ 12 mmag to look for the possibility of L, T dwarfs or brown dwarfs in the speculated brown dwarf desert (Grether and Lineweaver, 2006; Armitage and Bonnell, 2002).

The final list for candidates shortlisted for the programme, which satisfied all the above mentioned criteria, is provided in Table 2.2.

Radial velocity observations of these candidates as single-lined EB systems were taken up with PARAS. Four candidates (HD 261026, II CnC, SAO 74008, 1SWASP J0130+31) followed-up for RV variations from PARAS turned out to be false positives with no periodic RV variations seen, results of which are shown in the last column of Table 2.2. Two of the targets, HD 287039 and HD 222891 showed double-lined EB nature with large RV variations between two nearby observed data points indicating the companion to be a G-type star. Since, the focus is on VLMS in the current study, these targets were discarded for detailed analysis. Thus, for the thesis work, we have four successful discoveries of VLMS companions listed in Table 2.2. Three of them are mid-M

Table 2.2: PARAS EB Candidates

Candidate	Transit Depth (mmag)	Magnitude (V band)	Spectral Type	Discovery Survey	Results from PARAS
HD 213597	25	7.8	F0	*STEREO*	VLMS companion
HD 23765	49	9.5	F8	*STEREO*	VLMS companion
HD 287039	75	9.8	F8	*STEREO*	G-type companion
HD 222891	39	8.07	F8	*STEREO*	G-type companion
HD 261026	60	8.2	G4	*STEREO*	False positive
II CnC	25	8.5	G8	*STEREO*	False positive
SAO 106989	13.5	9.2	F7	*SuperWasp*	VLMS companion
1SWASP J2343+29	28	10.7	K3	*SuperWasp*	VLMS companion
1SWASP J0130+31	15.6	10.6	G4	*SuperWasp*	False positive
SAO 74008	12.2	9.6	K5	*SuperWasp*	False positive

dwarfs orbiting around F-type primary stars i.e HD 213597, HD 23765 and SAO 106989 systems. The fourth one, 1SWASP J2343+29, is a M7 dwarf orbiting around a K type primary. The mass of the secondary, in one of the EB systems, indicates discovery of one of the lowest mass M dwarfs discovered till date. The details of these four EB systems are discussed in Ch 4 and Ch 5.

2.6 Observation strategy

The observations of the selected objects were carried out using the 1.2 m PRL telescope. The candidate selection for each observing season was done well in advance and based on the celestial coordinates and the local sidereal time, the sources were queued for the observing run for a particular night. The following steps were taken care while making observations:

- The number of observations to be taken for a given source is planned on the basis of the predicted transit of the source from the photometry catalogues listed in §2.4. For a relatively longer period ($\geqslant 8$ days), the source was monitored for alternate days. For smaller periods ($\sim 2-8$ days), the spectra were recorded each day on different times in order to have a well sampled phase of the orbital period of the system.

- Stars, which are brighter than 6 mag, were recorded with an exposure time of 600 s and the fainter ones were observed at an exposure time of 1200 s or 1800 s based on the brightness of the source and sky condition. The exposure time was fixed such that a minimum SNR of 12/pixel for each spectra is obtained. The spectra having lower SNR were discarded during RV analysis.

- The sources were observed in a planned way so that the air mass of each observation remains below 1.6 (For most of the sources it is well below 1.3). This ensures better SNR for each observation by avoiding high extinction.

2.7 Observation Procedure

The celestial coordinates are fed from the telescope control room. A *starfish* camera is used as an auto-guider (to correct for the drift of the telescope and ensure smooth and accurate guiding of the star) to compensate for the tracking and guiding errors present in the telescope. About 8% of the starlight is passed to the guide CCD.

The starlight from the telescope has to be focused on to the fibers which carry the light to the other end where the spectrograph is kept. This is accomplished in a two-step process. A CCD is installed at the same focal plane as that of the fibers. Thus, focussing at the focal plane CCD ensures focussing of the image at the fibers as well. In the first step, the secondary mirror is adjusted in order to focus the image of the star obtained at the focal plane CCD. Once the focussing of the fiber is ensured, the same light can be made to fall on to the fiber. This image is obtained at a fixed (X,Y) position on the

CCD. The focal plane CCD is then moved away with a pre-calculated number of fixed steps and the fiber is brought at the same location as that of the CCD with the help of PI (Physik Instrumente) motor control. This step lets the starlight fall in close vicinity of the fiber.

The second step ensures that no light loss occurs while focussing on to the fiber. We have kept an exposure meter CCD which sees the light from the fiber at the spectrograph end. A kinematic mirror is installed inside the vacuum chamber that diverts the light from the slit position to the exposure meter. The exposure meter is an 752×580 array having a QE of 45%. Once the fiber output is maximized, the kinematic mirror is flipped and light is allowed to enter the slit position. The counts in the exposure meter CCD are maximized by fine adjustments in the PI stepper motor in X and Y directions. The overhead time for the entire process for observation, starting from pointing the telescope to beginning of exposure, takes approximately $5-10$ min for each star. Thus, 6 to 8 stars with exposure time duration of 1200 s can be observed each night depending on the duration of night.

An observation log (PARAS LOG) is maintained each night which keeps a record of the science and calibration images, the duration of exposure, the start and end time time of observation and air mass during the observations. The nightly condition of sky (clear/hazy/cloudy or passage of thin clouds or variations in seeing or any technical problems including guiding and pointing errors occurring during the observations) are recorded in the observation log.

The general procedure followed for observations is to record source spectra where star is observed in one fiber and ThAr calibration spectra in the other. The nightly calibration sequence includes 5 bias frames and 5 flat frames (for which both fibers are illuminated with a tungsten lamp), and several ThAr-ThAr frames (for which both fibers are illuminated with the calibration lamp) throughout the night. The purpose of the ThAr-ThAr frames is to carefully measure absolute instrument drift, as well as differential drifts. Science observations are usually made using simultaneous star-ThAr exposures ($2-3$ exposures per night per target).

2.8 Data analysis techniques

Echelle spectrographs have the advantage of covering a large wavelength region at high-resolution in a single exposure. However, the curved format of the spectra on the CCD detector due to cross-dispersion by the prism complicates the reduction process. The data extraction and analysis pipeline (PARAS PIPELINE) is a set of routines written in `IDL` to ease the complex and time consuming process of data reduction. The pipeline is developed as a part of collaboration between Penn State University and PRL. It is fully automated requiring minimal amount of user interaction; only if external factors necessitate it. PARAS PIPELINE is based on the `REDUCE` data analysis package developed by Piskunov and Valenti (2002) for processing cross-dispersed echelle data. It is modified to suit the requirements of PARAS data. Major components of PARAS PIPELINE are described in the following.

2.8.1 Raw data format of PARAS

PARAS acquires spectra at wavelengths between 3800 Å to about 9500 Å. Both the fibers when illuminated in the simultaneous observation mode corresponds to a separation of 17 pixels on the detector as mentioned earlier. Fig. 2.3 shows the spectra in the region around 5300 Å for frames when both the fibers are illuminated. The spectral resolving power has been computed for the spectrograph between orders 160 and 87 using ThAr lines. The median FWHM of the PSF for ThAr lines is 4 pixels. At about 8500 Å, the resolving power is found to be 65000, and at 9000 Å, it is about 61000.

The entire data set extracted from PARAS, for science and calibration purposes is in FITS format. The reduction process requires the presence of bias, flat fields and calibration lamp frames in unison with the science exposures. The data analysis pipeline is based on the `REDUCE` data analysis package for conventional and cross-dispersed echelle spectra developed by Piskunov and Valenti (2002).

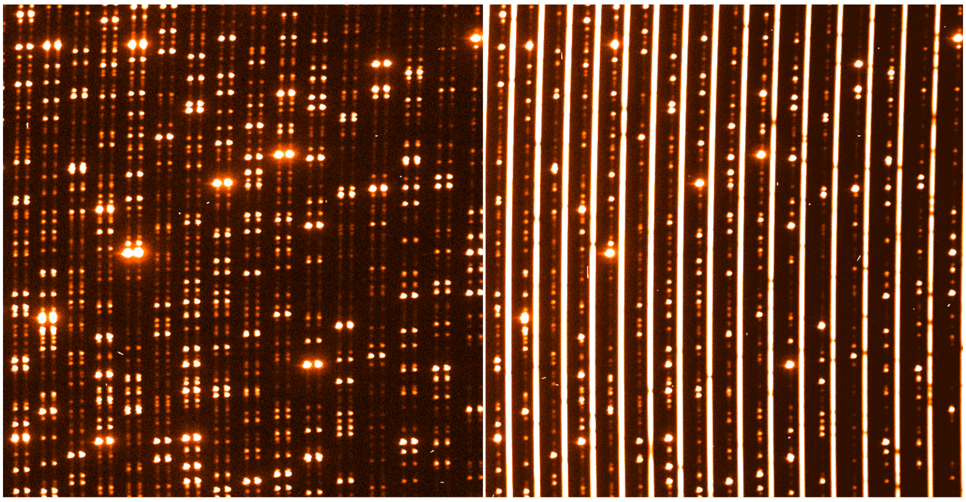

Figure 2.3: (left) Portion of raw image where both fibers are illuminated by ThAr calibration lamp (ThAr-ThAr), and **(right)** portion of image where one fiber is illuminated by star 47 UMa and other by ThAr calibration lamp (star-ThAr).

2.8.2 Bias corrections

The bias frames are recorded and combined in two groups, prior to and following science observations. These combined images are then compared for bias shifts, variations in read-noise and presence of any outliers and are further combined to produce a master bias frame. Bias corrections are imposed by subtracting master bias frame from all other calibration and science frames.

2.8.3 Location and extraction of orders

The grating order curvature present in the PARAS data is determined empirically from the obtained spectra. In order to locate the orders, flat frames are taken for the spectrograph by illuminating the fiber by hot Tungsten lamp generally before the science exposures. A master flat is created by combining all available flats. The echelle orders are located with the help of the combined master flats with negligible continuum. The software package `REDUCE` works on the principle of two dimensional clustering algorithm, selecting pixels from orders, clustering analysis of pixels, merging or rejecting clusters and fitting the merged clusters. PARAS has many spectral orders and to ease the process of order location, a mask is constructed which delimits the extraction of the image having sufficient SNR with no bad pixels. Since PARAS is a stable spectrograph, a master order trace is generated using a mean flat field and is incorporated in the automated pipeline. User interaction plays a role only for a few clusters where decision needs to be made for merging or rejection. The spatial profile of the order is represented by the illumination profile of an order taken perpendicular to echelle dispersion, whereas the spectral profile is the illumination along the order. The image is divided into swaths in order to separate the spectrum from the spatial profile. The spatial profile is fitted starting with an initial guess determined empirically from mean spatial profile, with weights based on a noise model. The slit function and spectrum is best reproduced by going through several iterations until the changes in the deduced spectrum is as small as epsilon (epsilon is 0.002 in this case).

2.8.4 Background estimation

Spectral extraction and normalization of flat-field images require estimation of scattered light in the background. Since, direct measurement of background beneath an order is not feasible, the background is interpolated between orders after decomposition of central group of columns in each order to empirically measure noise. Sky emission is included in this estimate, but the routine is not equipped to handle ghosts or very bright emission lines. There are no ghosts in the spectrograph even in the presence of strong argon lines beyond 7000 Å. The bleeding of bright argon lines at wavelengths greater than 7000 Å is restricted by means of a filter. A bleeding map, linearly scaled by a global parameter describing variations in lamp brightness (similar to Lovis and Pepe (2007)), is used for those orders which are not completely cured.

2.8.5 Wavelength Calibration

The task of converting the 1 D extracted spectra from "Intensity vs pixel" space to "Intensity vs wavelength" space is called wavelength calibration. This task can be accomplished by comparing the observed arc lamp (ThAr for current case) spectrum with a suitable template spectrum. The preliminary step for this was done by recording a ThAr spectrum and a cursory line identification was done manually with the help of *'echelle'* task of IRAF. The line identification templates were extracted from the Thorium-Argon Spectral Atlas (http://www.noao.edu/kpno/tharatlas/thar/). Five to six strong lines were identified across each order and a third order polynomial was fitted to create the blueprint thorium line list from PARAS. Since, PARAS is a stable spectrograph, the wavelength solution can be generated for simultaneous illuminated ThAr lamp spectra and can be used as a blueprint solution as long as external modifications do not affect the fiber and its position. Spectra observed at different epochs, shifted in velocity space due to the motion of the star in binary around its center of mass, are corrected for by cross-correlation techniques against the standard blueprint wavelength solution file. A third-order polynomial fit across each order leads to computation of polynomial coefficients for each order which can easily be used for determination of wavelength scale across the entire order. A complete thorium line list for the PARAS spectral range is utilized (similar to the SOPHIE line list at www.obshp.fr). For automated process, a binary mask of sharp thorium lines is created which is used to assist the calibration process. The cross-correlation function (CCF) is calculated by shifting this thorium mask against each spectral order, and the net drift value is corrected for each spectra. The extracted wavelength solution is imposed on the observed stellar spectra in the simultaneous reference mode, thereby enabling wavelength solution for each observed science exposure by incorporating necessary drift corrections.

2.8.6 Radial velocity computation

Radial velocities are derived by cross-correlating target spectra, i.e. computing the CCF with a suitable numerical stellar template mask, created especially from high signal-to-noise ratio spectra or synthetic data (Baranne *et al.*, 1996). It consists of values 1 and 0, where non-zero values correspond to theoretical positions and widths of the absorption lines at zero velocity. The CCF is constructed by shifting the mask as a function of Doppler velocity. This can be written as (Pepe *et al.*, 2002):

$$\mathrm{CCF(v_r)} = \int \mathrm{S}(\lambda)\cdot \sum_{\mathrm{i}} \mathrm{M_i}\lambda(\mathrm{v_r})\mathrm{d}\lambda = \sum_{\mathrm{i}} \int \mathrm{S}(\lambda)\mathrm{M_i}\lambda(\mathrm{v_r})\mathrm{d}\lambda \tag{2.2}$$

Here, $S(\lambda)$ is the recorded spectrum, $\lambda(v_r)$ represents the Doppler-shifted velocity and M is the numerical mask which can be expressed as the sum of masks M_i corresponding to each stellar absorption line i. The technique of computing RVs with numerical masks has eliminated the dependency on high SNR spectra.

However, a non-weighted mask is unable to retrieve the precise information. Pepe *et al.* (2002) suggested that the deep and sharp lines in a spectra should be weighted higher as they contain much more information than broad and weak lines. As shown by the authors, for a given amplitude of the CCF_i, the noise on each point of the CCF and thus on the resulting Gaussian fit is

$$\sigma_i^2 \propto S_i \propto \frac{\mathrm{CCF_i}}{c_i} \propto \frac{1}{c_i} \tag{2.3}$$

The weight given to the single CCF_i is

$$w_i = \frac{1}{\sigma^2} = c_i \tag{2.4}$$

Here, c_i is relative depth of each line. The width of the weighted mask lines is 3 km s^{-1} and the depth is set by the line depths depending on different spectral types. The CCF computing algorithm for PARAS PIPELINE is initiated by providing an estimate of the RV value.

A range is set around which the mask is recreated (moved in velocity space) and CCF for each order is computed. The CCF for all the orders are summed up and finally fitted with a Gaussian function to compute the RV value for the spectra at that epoch. The RV values thus determined are finally plotted against time or phase of the orbital period of the stellar system.

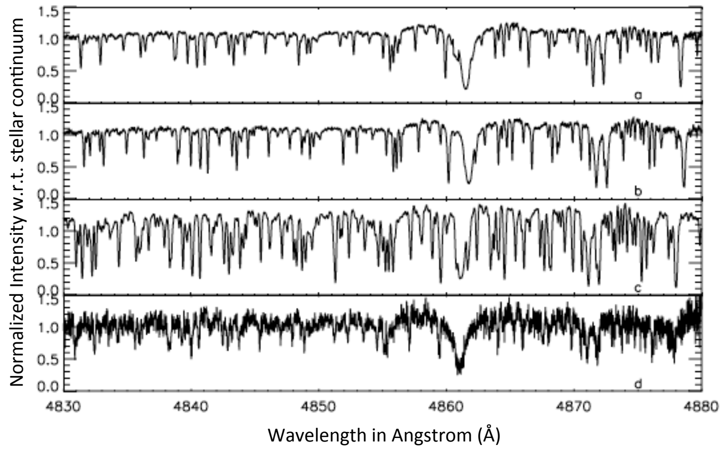

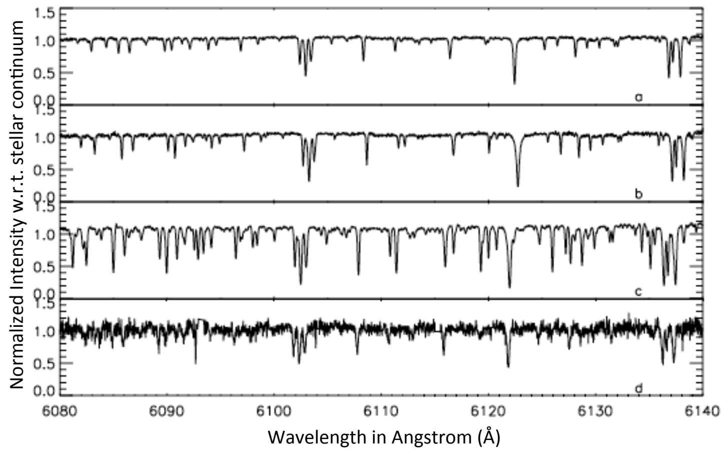

Figure 2.4: Portions of extracted and wavelength calibrated spectra. The stars shown are 47 UMa (G1V, a), Sig Dra (K0V, b), HD137759 (K2III, c) and HD 185374 (G0 IV, d)

2.8.7 Blaze correction and co-addition of spectra

The echelle spectra is blazed at each order, which needs to be accounted for before the spectra is normalized. For this purpose, a polynomial function is fitted iteratively to an accuracy of ∼1 % across the stellar continuum blaze profile for each order after ignoring absorption features in the stellar spectra. The observed spectra are then divided by this function to blaze correct and normalize it at a given epoch. In the whole process of blaze correction, pixel-to-pixel detector quantum efficiency variances are not accounted for because the detector is anti-reflection (AR) coated with a maximum pixel response non-uniformity (PRNU) of 3 % between the operated wavelength region of the spectrograph [3]. For, the same reason, flat-fielding is also not done for PARAS spectra. Fig. 2.4 shows a section of blaze-corrected and RV corrected sample spectra in both blue and red regions for four stars of different spectral types. Typical exposure times on these sources were 10 minutes, except in the case of HD 185374, where it was 15 minutes.

[3]www.e2v.com/resources/account/download-datasheet/1364

Chapter 3

A Spectral Analysis Code: PARAS SPEC

3.1 Introduction

As mentioned earlier, the double-lined EBs (SB2) enable the most accurate measurements of the radii and masses of the stars. Since in such systems spectra of both the stars can be recorded, RV measurements lead to precise determination of masses of the stars in the system directly. However, in single-lined EBs (SB1) systems, where the spectra of only the primary source is available, mass of the secondary is deduced by quantifying the amplitude of the wobble on the primary star in the binary system. Radial velocity (RV) studies with high-resolution spectroscopy on SB1 systems or with a star-planet system leads to determination of mass function for the system as given in Eq. 1.12. The mass of the secondary can only be determined if the mass of the primary and orbital inclination of the system are known. Orbital inclination can be obtained from photometry study as discussed in Ch 1. In order to infer mass of the primary and to classify whether the star is in main-sequence or in giant or sub-giant phase, it is essential to know the surface gravity (g = GM/R^2), often quoted in the form of log g, surface temperature ($T_{\rm eff}$), and metallicity ($[Fe/H]$) of the star. A detailed study by Torres, Andersen and

Giménez (2010) on a large sample of EBs has led to the establishment of an empirical relation for the mass and radius of the stars above 0.6 $M_{\odot}$ based on the stellar parameters, i.e, log g, the T_{eff} and $[Fe/H]$. In our case, since we have high-resolution spectroscopy data obtained for RV measurements, we can as well as use the same data to derive the stellar parameters.

There are many host stars for which spectral properties have not been studied so far and therefore it is of utmost importance to derive the same in order to draw inference on their mass and radius. In this context, we have developed a pipeline *PARAS SPEC*, to estimate the stellar atmospheric parameters from the analysis of stellar spectra. With high-resolution spectroscopy, it is possible to determine T_{eff} and $[Fe/H]$ (based on Fe I and Fe II lines) as well as log g (based on Mg I lines) at high accuracies. The pipeline, a set of `IDL`-based tools, is developed to facilitate the determination of stellar properties. The technique is based on two principal methods. The first method involves fitting of the observed spectrum with different synthetic spectra for a set of stellar parameters. The best-match having minimum χ^2 value between the observed and the synthetic spectra gives the best-fit values for the stellar parameters of the star. The second method is based on equivalent widths (EWs) that are used to derive abundances for a set of Fe I and Fe II lines from the observed spectra (Blanco-Cuaresma *et al.*, 2014). The abundances determined must fulfill the conditions of excitation equilibrium and ionization balance. The stellar model for which the conditions of equilibria are satisfied is considered to be the best-fit model for representing the observed spectra.

3.2 Methodology

The `IDL`-based tool, named *PARAS SPEC* is designed to facilitate the estimation of stellar parameters from PARAS observed spectra. The *PARAS SPEC* code requires blaze-corrected and normalized stellar spectra as an input. The blaze-corrected and normalized stellar spectrum is an output of the data reduction and analysis pipeline, PARAS PIPELINE as described in Ch 2. The detailed steps used by *PARAS SPEC* are described as follows:

3.2.1 A library of synthetic spectra

Observed PARAS spectra are compared with this reference library spectra which is at a similar resolving power as that of PARAS. A library of synthetic spectra is generated using the code `SPECTRUM` (Gray, 1999) [1]. PARAS observed solar spectrum is used to fix parameters, such as micro-turbulent velocity (v_{micro}), macro-turbulent velocity (v_{macro}) and stellar abundances for the synthetic spectral library. The relevant details are briefly described as follows.

3.2.1.1 `SPECTRUM` program

Synthetic spectra generator code `SPECTRUM` utilizes the Kurucz models (Kurucz, 1993) for stellar atmosphere parameters. `SPECTRUM` works on the principle of local thermodynamic equilibrium and plane parallel atmospheres. It is suitable for generation of synthetic spectra for stars from B to mid M type. It is developed with C compiler environment with a terminal mode interface to access it.

3.2.1.2 Solar spectrum

A solar spectrum (SNR ∼150) observed with PARAS is taken up as a first step to fix various parameters for the library of synthetic spectra. The synthetic spectra can be generated at a fine wavelength spacing of 0.01 Å between two consecutive wavelength values. This resolving power (R ∼ 500,000 at 5000 Å) is very high in comparison to the resolving power of PARAS (R ∼ 68,000 at 5000 Å). For PARAS, the wavelength dispersion is 0.02 $\AA$/pixel at 5500 $\AA$ and 0.024 $\AA$/pixel at 6500 $\AA$. PARAS has a resolution element of 4 pixels and thus the FWHM of the spectral profile of PARAS at the central wavelength region, 5500 Å, is ∼ 0.08 Å. In order to match the spectra, both the synthetic and observed spectra must have the same sampling and should be at the same

[1] http://www.appstate.edu/∼grayro/spectrum/spectrum276/spectrum276.html

resolving power. FWHM varies across the entire wavelength region covered by the PARAS spectra but for simplicity we use the the central wavelength FWHM for convolution of synthetic spectra with a Gaussian function. This is kept fixed for the entire library of synthetic spectra. All the parameters for the observed solar spectrum, such as, $v_{\rm micro}$, $v_{\rm macro}$, rotational velocity ($v \sin i$), $T_{\rm eff}$, $[Fe/H]$ and log g are kept free. When all the parameters are kept free, the best-derived model having the least χ^2 for the PARAS observed solar spectra has the following values for various parameters: $v_{\rm micro}$ = 0.85 km s^{-1} and $v_{\rm macro}$ = 2 km s^{-1}. The value for $v_{\rm micro}$ obtained here is in close agreement with the one derived by Blackwell, Booth and Petford (1984). The value of $v_{\rm macro}$ = 2 km s^{-1} derived here is consistent with the value of 2.18 km s^{-1} obtained by (Valenti and Piskunov, 1996). The value of $v_{\rm micro}$ and $[Fe/H]$ are partially degenerate as studied by Valenti and Fischer (2005), which means there can be more than one combination of $v_{\rm micro}$ and $[Fe/H]$ for a best-fit solution. Thus, following a similar approach as that of Valenti and Fischer (2005), it was decided to keep $v_{\rm micro}$ fixed in order to minimize the errors on estimation of $[Fe/H]$. A similar degeneracy is seen in the parameters $v_{\rm macro}$ and $v \sin i$. Stars having temperatures between 5000 – 6500 K, similar to those observed with PARAS, have a range of $v_{\rm macro}$ values between $2 - 5$ km s^{-1} (Valenti and Fischer, 2005). We set $v_{\rm macro}$ fixed at 2 km s^{-1} so that an upper limit on $v \sin i$ is determined, similar to the approach followed by (Valenti and Fischer, 2005). There are two atomic line-lists present in the distribution of `SPECTRUM`, *luke.lst* and *luke.iso.lst*. We used the second line list for the entire library since it was found that it has relatively smaller χ^2 than the first linelist (luke.lst) for the same synthetic models.

3.2.1.3 The synthetic library

The synthetic library consists of the following building blocks. The tabulated stellar library generated is given as Table 3.1.

- **Models:** The models for the synthetic spectra are retrieved from the Kurucz model database (Kurucz, 1993). The models are a byproduct of the larger combined family of models, the supermodels. Each supermodel belongs to a single metallicity and comprises different models having varying temperatures and surface gravity. Each model has a typical format, which the `SPECTRUM` routine undertakes into consideration while execution. It consists of the following columns.

1. $\int \rho$ dx: mass depth (g cm^{-2})
2. $T_{\rm eff}$: temperature (K)
3. $P_{\rm gas}$: gas pressure (dynes cm^{-2})
4. n_e: electron density (cm^{-3})
5. κ_R: Rosseland mean absorption coefficient (cm^2 gm^{-1})
6. $P_{\rm rad}$: radiation pressure (g cm^{-2})
7. $v_{\rm micro}$: microturbulent velocity (m s^{-1})

different combinations of $T_{\rm eff}$, $[Fe/H]$, log g and $v \sin i$ lead to generation of 19,200 synthetic spectra. The ranges of these parameters chosen are given in Table 3.1.

- **Interpolation of model atmospheres:**

  The `SPECTRUM`-generated synthetic library originally consists of a coarse grid in $T_{\rm eff}$, $[Fe/H]$ and log g. A finer grid is required to achieve the close resemblance of the observed spectra with the synthetic spectra. Thus, during the course of execution of the synthetic spectral fitting routine, the synthetic models are interpolated in the desired range of $T_{\rm eff}$, $[Fe/H]$ and log g to sharpen the precision of the derived parameters. The interpolation on the models is executed by the `IDL` subroutine `kmod`. The interpolated models then have a finer interval in $T_{\rm eff}$ (50 K), $[Fe/H]$ (0.1 dex) and log g (0.1 dex) as mentioned in Table 3.1.

- **Atomic line list:** `SPECTRUM` code distribution includes two line lists, namely, *luke.lst* and *luke.iso.lst*. As mentioned earlier, we tested both the atomic line lists on the solar spectra and found the *luke.iso.lst* yield better results in terms of a better minimized χ^2.

- **Abundances:** The standard solar abundances, which are provided by Anders and Grevesse (1989); Grevesse and Sauval (1998); Asplund, Grevesse and Sauval (2005); Grevesse, Asplund and Sauval (2007); Asplund *et al.* (2009), are used for generation of synthetic spectra with *PARAS SPEC*. The abundance value of any element for a star is computed by taking a ratio of the abundance of that element present in the star with respect to the solar abundance for the same element.

$$[Fe/H] = log_{10} \left(\frac{[Fe/H]_{star}}{[Fe/H]_{sun}} \right) \tag{3.1}$$

Table 3.1: Synthetic Spectral Library

Parameter	Range	Original Interval	Interpolated interval
$T_{\rm eff}$ (K)	4000 – 7000	250	50
$[Fe/H]$ (dex)	−2.5 – 0.5	0.5	0.1
log g (dex)	3.0 – 5.0	0.5	0.1
Wavelength (Å)	5050 – 6560	0.01	0.01
$vsini$ (km s^{-1})	1 – 40	1	1

3.2.2 Preliminary considerations

The spectra across various orders are blaze-corrected as discussed in § 2.8.7 and are stitched together to produce a continuous single spectrum. Many such epochs are co-added in velocity space to improve the signal-to-noise ratio (SNR) of the stellar spectra. In absence of any absorption line, the synthetic spectral continuum value is 1.0 since it is a normalized spectra. For the observed spectra, the continuum level fluctuates around 1.0, as the blaze correction is not accomplished accurately for the case of deep absorption lines in the spectra. The continuum value in the vicinity of a prominent absorption feature is likely to be under-estimated due to the broad wings in the absorption profile. To eliminate this issue, we devised a method wherein the observed stellar spectra is normalized with respect to its stellar continuum in small wavelength intervals of 5 Å each.

3.2.3 Synthetic Spectral Fitting method

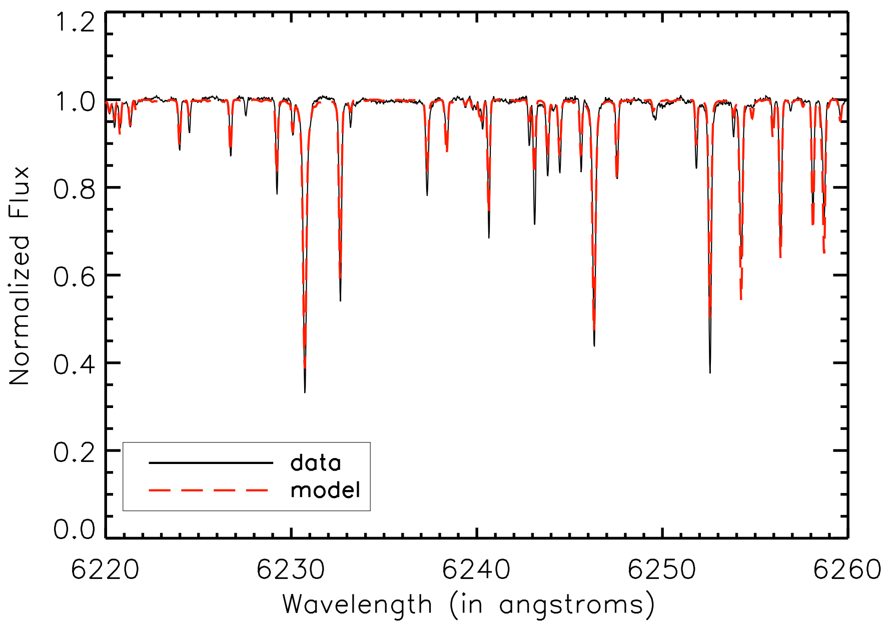

Figure 3.1: Observed normalized spectra for τ Ceti (solid black line) plotted across the wavelength region of $6220 - 6260$ $\AA$. Overplotted is the modelled spectra (red dash line) obtained from *PARAS SPEC* analysis, with $T_{\rm eff}$ of 5400 K, $[Fe/H]$ of -0.5 and log g of 4.4.

The synthetic spectral fitting method is then executed in four steps. $T_{\rm eff}$, $[Fe/H]$ and log g are all kept free in the first step. The RMS residuals defined as $\sum (O(i) - M(i))^2$ are computed between the observed and the synthetic spectra at each wavelength λ_i in the wavelength range $5050 - 6000$ $\AA$. Here, O & M are the observed and model spectra respectively. The best-match values of $T_{\rm eff}$ and $[Fe/H]$ are determined from this step. The first step of

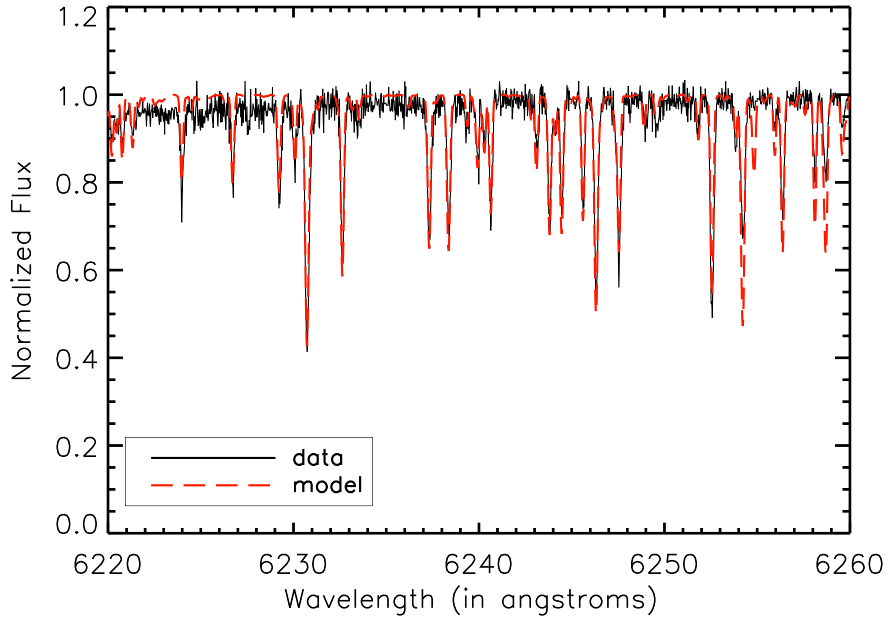

Figure 3.2: Observed normalized spectra for KID 5108214 (solid black line) plotted across the wavelength region of 6220 – 6260 $\AA$. Overplotted is the modelled spectra (red dash line) obtained from *PARAS SPEC* analysis, with $T_{\rm eff}$ of 6000 K, $[Fe/H]$ of 0.3 and log g of 4.0.

synthetic spectral fitting is executed on the set of models which have not been interpolated to a finer grid. The $T_{\rm eff}$, $[Fe/H]$ and log g parameters determined from the original set of library (case of non-interpolated models) will thus have a coarse precision, as given in second column of Table 3.1.

In the second step, the parameters obtained from the previous step are used as an initial guess value and interpolation is done simultaneously at finer precision in $T_{\rm eff}$, $[Fe/H]$ and log g in the wavelength range between 5050 – 6000 $\AA$ as given in third column of Table 3.1. The interpolation is done in the vicinity of the guess values on the three parameters obtained from the first step, i.e., $T_{\rm eff}$ in a range of $\pm$ 250 K, $[Fe/H]$ in a range of $\pm$ 0.3 and log g in a range of $\pm$ 0.3. The best-determined values derived from this second step are considered as initial approximations on stellar parameters for the third step.

In the third step, the same routine is re-run, but this time only on the log g sensitive Mg I lines in the wavelength region of 5160 – 5190 $\AA$ by keeping $T_{\rm eff}$

and $[Fe/H]$ the same as obtained from the second step.

The fourth step is executed again on the wavelength region of $5160-5190$ $\AA$ on the interpolated models which are generated during the course of execution of the code. The best-match model determined at this step gives us the value for log g along with previously determined values of $T_{\rm eff}$ and $[Fe/H]$ from the second step.

A typical best-determined synthetic spectra from the *PARAS SPEC* routine overlaid on normalized observed spectra for star τ Ceti is shown in Fig. 3.1. The SNR for this spectra is $\sim$ 500/pixel at 6000 $\AA$. The entire wavelength region of $5050-6500$ $\AA$ is covered for this star. In Fig. 3.2, the spectra for a faint star (V=8 mag), KID 5108214, having a SNR of $\sim$ 100 pixel^{-1} at 6000 $\AA$ is shown. The observed spectra appears more noisy than τ Ceti due to relatively less SNR in comparison to that for τ Ceti. If the spectra having SNR below $\sim$ 80 are used, the uncertainties on each of the stellar parameters are approximately equal to the coarse grid size of the library (column 3 of Table 3.1). Thus, for this method, we mention a lower limit on SNR of that being $\sim$ 80 in the entire wavelength region covered. For fainter stars having magnitudes between $7-11$ in V band, the method fails if applied as it is described above for the entire wavelength range $5050-6000$ $\AA$. Despite co-adding spectra for several epochs, SNR for some stars is below 80 in the blue end ($5050-6000$ $\AA$). Since, the CCD is more sensitive to redder wavelengths, even for stars having magnitudes between $7-11$ in V band, we expect a higher SNR (generally above 80) in the red portion of the spectra. Thus, we concentrate on the wavelength region between $6000-6500$ $\AA$ of the CCD where SNR is above 80 for such cases. However, despite the fact that we are able to determine $T_{\rm eff}$ and $[Fe/H]$, we lose crucial information of the surface gravity, which is dependent on the Mg I lines occurring between $5160-5190$ $\AA$. Thus, for such cases, it is necessary to rely upon the EW method inspired by the work of Blanco-Cuaresma *et al.* (2014).

3.2.4 EW Method

The EW method works on the principle in which one seeks the neutral and ionized iron lines to satisfy the two equilibria, namely, excitation equilibrium and ionization balance. A set of neutral and singly ionized lines is acquired from the iron line list by Sousa *et al.* (2014). The method is executed step by step as described below.

3.2.4.1 Measurement of EW

The EW of a spectral line is dependent on the number of photons that are absorbed at a particular wavelength.

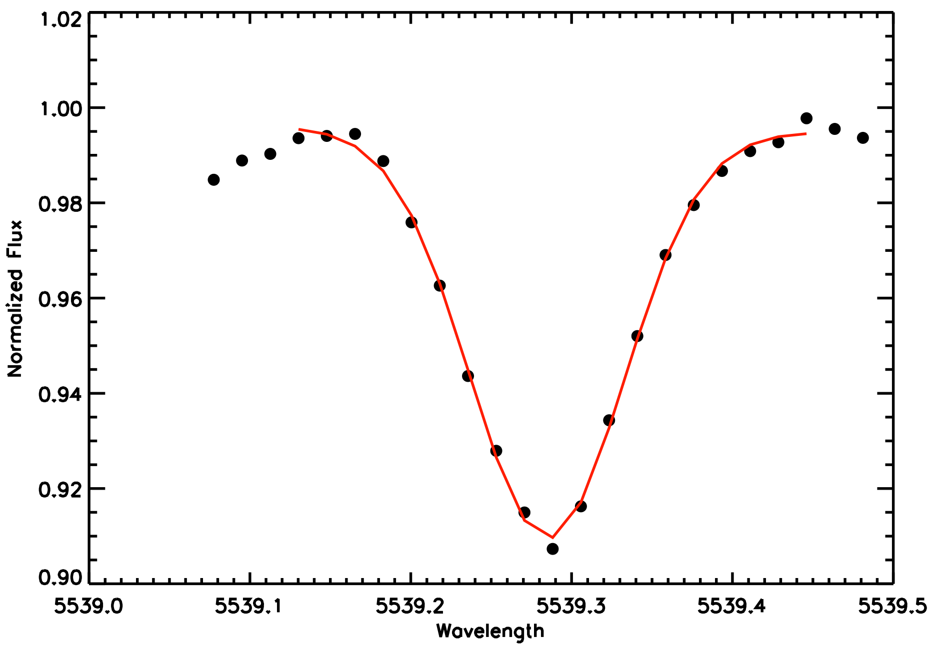

Figure 3.3: Observed spectral line profile of a Fe I line centered at wavelength 5539.2800 Å is seen in black dots. Overplotted in red is the Gaussian-fit function used to measure the EW of the line

The EW defined as:

$$W_\lambda = \int (1 - F_\lambda / F_o) d\lambda. \tag{3.2}$$

Here, F_o represents the continuum level, F_λ represents flux at a given wavelength, λ and W_λ represents the EW at that λ. It can be geometrically represented as the area of the line profile. Hence, it can be represented as the width in wavelength of a rectangular profiled line 100% deep having the same area in a flux vs wavelength plot as the actual spectral line profile (Emerson, 1996). For the measurement of EW, a Gaussian function is fitted for each spectral line of the observed spectra corresponding to all the iron lines that are present in the line list given by Sousa *et al.* (2014). Each Gaussian-fitted profile corresponding to the iron line list is then carefully inspected and poor fits and line blends are eliminated. A typical spectral line profile along with the fitted Gaussian function is shown in Fig. 3.3.

3.2.4.2 Determination of abundance

The `SPECTRUM` code facilitates estimation of abundance of elements from their spectral lines. After careful inspection of the EW fits as discussed above, a set of EW of the fitted lines is given as an input to the `ABUNDANCE` subroutine of `SPECTRUM`. The subroutine uses various stellar models which are formed as a combination of different T_{eff}, $[Fe/H]$, log g and v_{micro}. The output of the `ABUNDANCE` routine is as follows.

6127.895 26.0 1.08 -4.581 7.459 -0.041

The first and second columns stand for the central wavelength of the line formed by an element and the atomic number of that element, the third column is the v_{micro} (in km s^{-1}). The fourth column gives the abundance on the scale where total abundances are expressed with respect to the total number density of atoms (and ions), the fifth column expresses abundances on the normal scale, in which the logarithmic abundance of hydrogen is equal to 12.0. The last column is the abundance relative to the unscaled abundances with respect to solar abundances for the current case.

3.2.4.3 The three golden rules

The main purpose of calculating EW and thereby abundances is the fact that the abundances of a given species follow a set of three golden rules. This fact can be employed to choose a best-fit model of synthetic spectra in which all the rules are simultaneously satisfied. These three rules are:

1. Abundances as a function of excitation potential (EP) should have no trends.
2. Abundances as a function of reduced EW (EW/λ) should exhibit no trends.
3. Abundances of neutral iron (Fe I) and ionized iron (Fe II) should be balanced.

The *PARAS SPEC* routine is executed with a fixed value of metallicity. This value is taken from any previous measurements of metallicity done on the source as cited in literature or from the first method of synthetic spectral fitting. The abundances thus generated are plotted against EP and reduced EW for the respective lines. The ionization balance (Fe I - Fe II) is also estimated for each set of models. The slopes for the first two scatter plots and the difference of Fe I and Fe II are calculated for each set of models. The entire process is executed in two steps: first step on the coarse grid of models in $T_{\rm eff}$, log g and $v_{\rm micro}$ and second step on the interpolated finer grid, similar to the previous method of synthetic spectral fitting. Thus, the model having a set of parameters where the slopes and the differences are simultaneously minimum gives us the best-determined $T_{\rm eff}$, log g and $v_{\rm micro}$.

As a test case, for star τ Ceti (SNR $\sim$ 500), the stellar parameters are determined by the EW method. The plot of iron abundance vs EP is shown in the upper panel of Fig. 3.4. The figure also shows a solid line in blue obtained by a least-square fit having a slope of $0.0036^{+0.007}_{-0.008}$; indicative of the best-fit $T_{\rm eff}$ of 5400 K. In the bottom panel, a plot of iron abundance vs reduced EW is shown. A solid line in blue-green obtained by a least-square fit having a slope

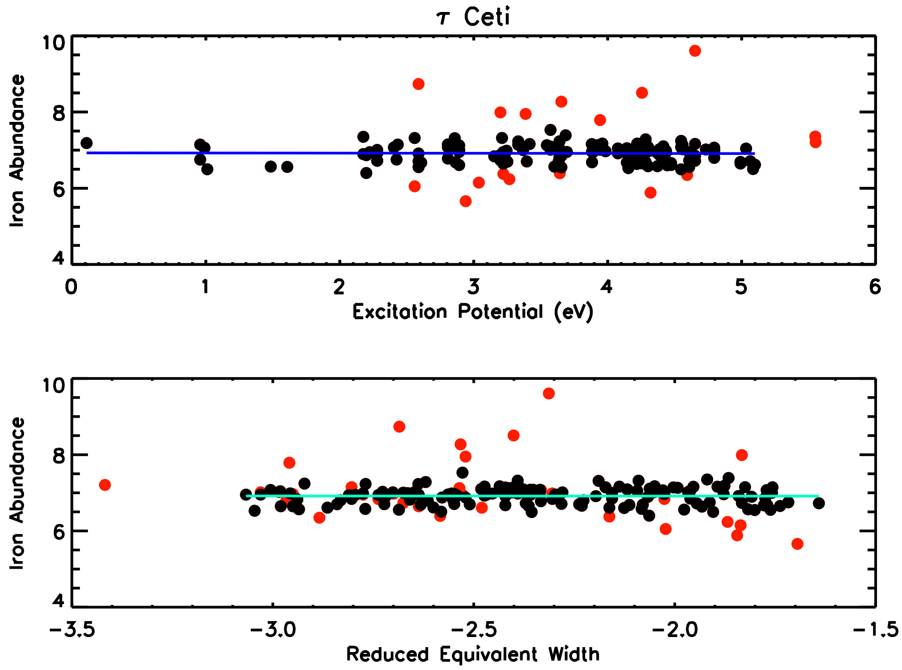

Figure 3.4: (Top panel) Iron abundance for τ Ceti is plotted against excitation potential for each Fe I or Fe II line from the line list. The blue line is the least-square fit having the minimum slope for the best-determined model temperature. (Bottom panel) Iron abundance is plotted against reduced EW and the blue-green line indicates the least-square fit having a minimum slope for best-determined value of $\upsilon_{\rm micro}$. The red points are the discarded points having standard deviation beyond 1 σ (not considered for the fit). The best-fit determined parameters are: $T_{\rm eff}$ = 5400 K, log $g = 4.4$, $\upsilon_{\rm micro} = 0.2$ km s^{-1} for $[Fe/H] = -0.5$

of $-0.002^{+0.002}_{-0.001}$ is shown indicative of best-fit $\upsilon_{\rm micro}$ of 0.2 km s^{-1}. The log g value is determined where the difference between Fe I and Fe II abundances is minimum. Since the difference is just a number, no plot is shown for this case. For τ Ceti, the difference is $0.00^{+0.002}_{-0.002}$; indicative of a best-fit log g value of 4.4. All the three parameters, $T_{\rm eff}$ and $\upsilon_{\rm micro}$ and log g are obtained simultaneously where the slopes (Iron abundances vs EP and Iron abundances vs reduced EW) and difference of abundances of Fe I and Fe II are simultaneously minimum. A similar plot is shown for the star KID 5108214 having spectra of less SNR (SNR of $\sim$ 100 pixel^{-1}) in Fig. 3.5. The upper panel of the figure also shows a solid line in blue obtained by a least-square fit having a slope of $0.018^{+0.017}_{-0.006}$

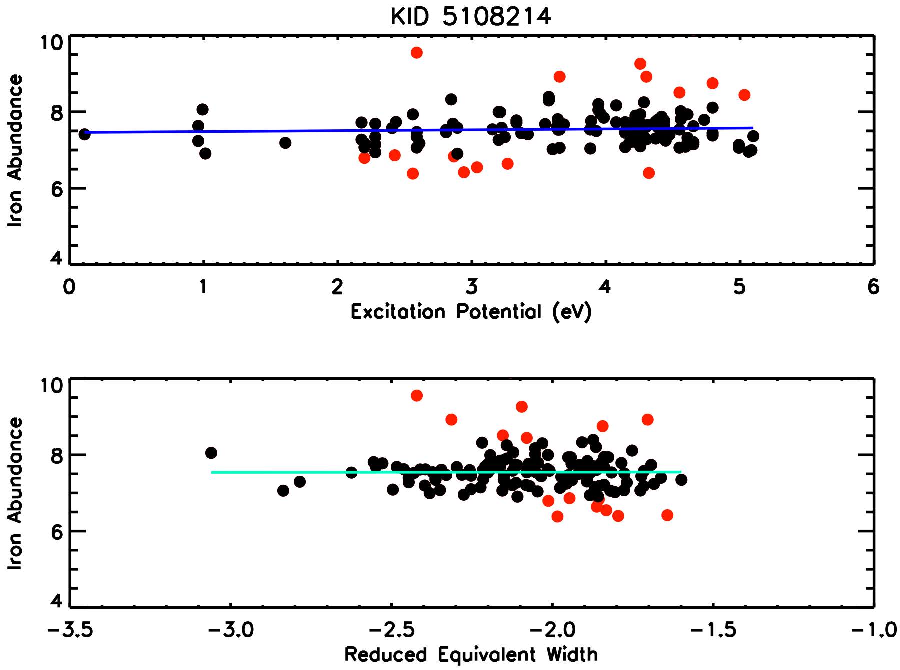

Figure 3.5: (Top panel) Iron abundance for KID 5108214 is plotted against excitation potential for each Fe I or Fe II line from the line list. The blue line is the least-square fit having the minimum slope for the best-determined model temperature. (Bottom panel) Iron abundance is plotted against reduced EW and the blue-green line indicates the least-square fit having a minimum slope for best-determined value of $v_{\rm micro}$. The red points are the discarded points having standard deviation beyond 1 σ (not considered for the fit). The best-fit determined parameters are: $T_{\rm eff}$=6050 K, $[Fe/H]$=0.5, log g = 3.95, $v_{\rm micro}$ = 1.65 km s^{-1} for $[Fe/H]$ = 0.3

for iron abundances vs EP indicative of best-fit $T_{\rm eff}$ of 6050 K. In the bottom panel, a plot of iron abundance vs reduced EW is shown. A solid line in blue-green obtained by a least-square fit having a slope of $0.01^{+0.004}_{-0.007}$ indicative of best-fit $v_{\rm micro}$ of 1.65 km s^{-1} is also shown in the bottom panel. Fe I - Fe II difference for KID 5108214 is given as $0.001^{+0.009}_{-0.001}$ indicative of a log g value of 3.95.

Both the parameters, $T_{\rm eff}$ and $v_{\rm micro}$, which are determined by fitting the slopes to the above-mentioned plot, are determined simultaneously. A slight positive or negative slope indicates under-estimation or over-estimation of $T_{\rm eff}$ and $v_{\rm micro}$ for the star respectively. Similarly, if the Fe I and Fe II difference is positive or negative, it indicates that log g is under-estimated or over-estimated respectively. A set of simulations were done where we supplied models with higher $T_{\rm eff}$ or $v_{\rm micro}$ to see how the slope changes. The results of these simulations are shown in Fig 3.6. As a test case, we show here the simulations done in a step-size of 250 K for the value of $T_{\rm eff}$. This step-size chosen is just for illustrative purposes as it is the grid size of the original library with no interpolated models. This simulation is to give an idea how the other parameters of the star get affected if an under-estimated $T_{\rm eff}$ model is supplied. It is important to note that the synthetic spectra are finally interpolated on a finer grid to gain a better precision. When a lower $T_{\rm eff}$ model, 5150 K (250 K lower than the best-fit model) is supplied for the star τ Ceti, a positive slope ($0.008^{+0.012}_{-0.01}$) for Abundance vs EP plot is seen. The plot for abundance vs reduced EW has a slope of $-0.076^{+0.006}_{-0.008}$ and the difference of Fe I and Fe II is $-0.252^{+0.004}_{-0.004}$. Thus, we see that none of the parameters have achieved a minimum slope or a minimum difference indicating of a state where excitation equilibrium and ionization equilibrium is not achieved. For the case when a higher $T_{\rm eff}$ model, 5650 K (250 K higher than the best-fit model) is supplied, a negative slope for abundance vs EP plot is seen ($-0.04^{+0.01}_{-0.009}$). The plot for abundance vs reduced EW has a slope of $0.1346^{+0.005}_{-0.006}$ and the difference of Fe I and Fe II is $0.22^{+0.003}_{-0.004}$. The bottom panel, the slope of abundance vs Reduced EW also shows a departure from the zero slope. Similarly to the previous case, excitation and ionization equilibria are not achieved in this case too.

Both the methods of synthetic spectral fitting and EW method are applied on several known stars. The results are summarized in Table 3.2.

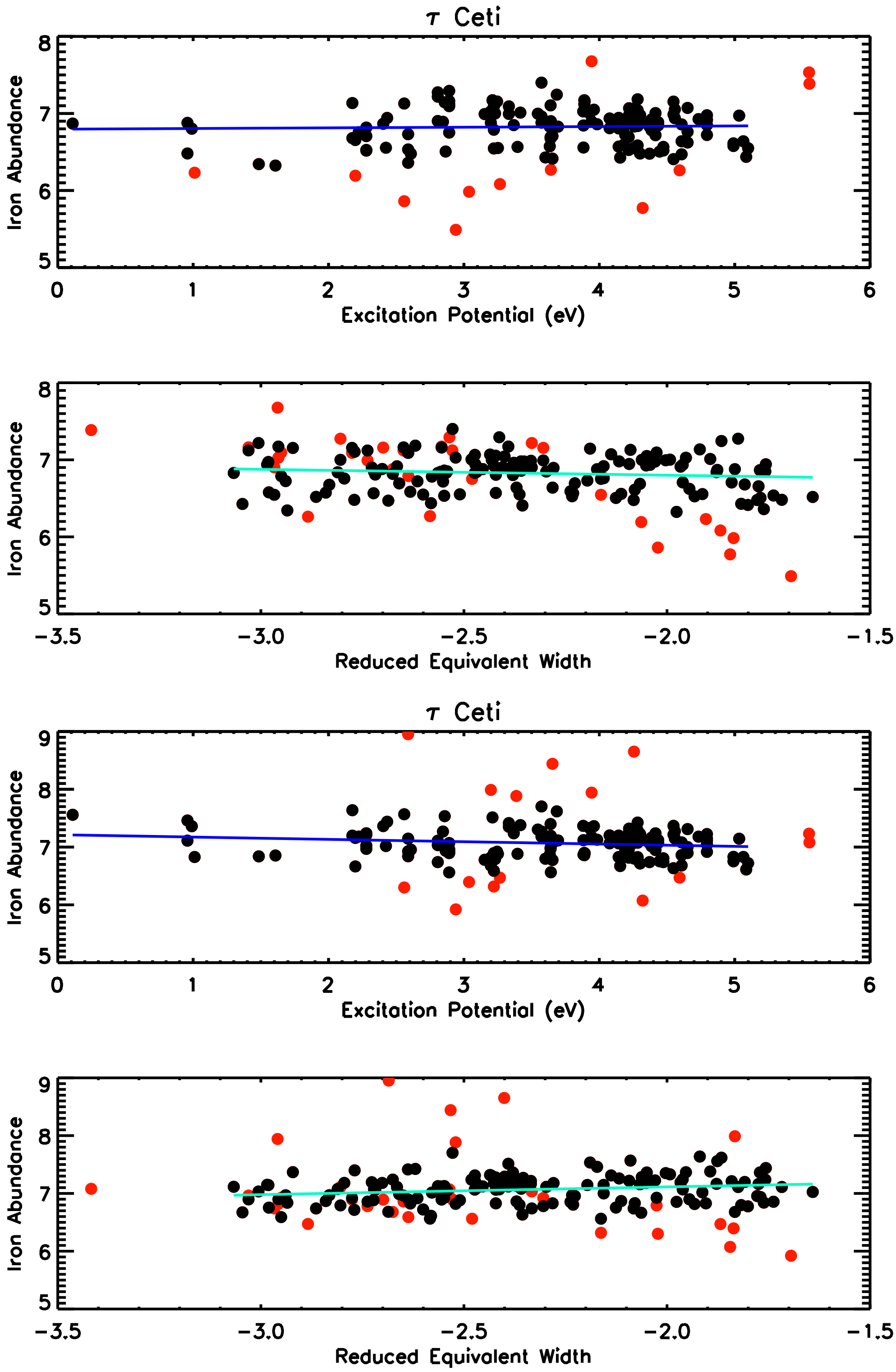

Figure 3.6: Simulations run for the star τ Ceti. The $T_{\rm eff}$ for the upper two panels is 250 K lower than the correct $T_{\rm eff}$ and in the bottom two panels the $T_{\rm eff}$ is 250 K higher. Thus, we see a positive slope and negative slope in the abundance vs EP plot and Abundance vs Reduced EW in the upper two and lower two panels respectively.

Table 3.2: Results obtained from Spectral analysis (SF=Spectral Fitting; EW=Equivalent Width Method; LV= Literature Value

Star	T_{eff}			$[Fe/H]$			$\log g$			
	SF	EW	LV	SF	EW (fixed $[Fe/H]$)	LV	SF	EW	LV	
τceti	5400 ± 25	5400 ± 12	5414 ± 10	-0.50 ± 0.1	-0.5	-0.5 ± 0.01	4.40 ± 0.05	4.5 ± 0.05	4.49 ± 0.03	(1)
Sigma Draconis	5450 ± 25	5475 ± 12	5400 ± 50	-0.1 ± 0.05	-0.1	-0.20 ± 0.06	4.50 ± 0.05	4.50 ± 0.05	4.5 ± 0.05	(2)
Procyon	6550 ± 25	6650 ± 12	6554 ± 18	0.0 ± 0.05	0.0	-0.04 ± 0.01	3.9 ± 0.05	3.9 ± 0.05	3.99 ± 0.17	(1)
HD9407	5700 ± 25	5725 ± 25	5661 ± 30	0.0 ± 0.1	0.0	0.03 ± 0.09	4.4 ± 0.05	4.35 ± 0.05	4.42 ± 0.14	(3)
HD16620	5200 ± 50	5025 ± 50	4966 ± 205	0.0 ± 0.1	0.0	-0.17 ± 0.08	4.6 ± 0.05	4.35 ± 0.1	4.45 ± 0.17	(3)
NLTT25870	5400 ± 50	5225 ± 25	5326 ± 45	0.3 ± 0.1	0.3	0.4 ± 0.07	-	4.6 ± 0.05	4.45 ± 0.08	(4)
HD285507	4650 ± 75	4450 ± 50	4542 ± 50	0.1 ± 0.1	0.1	0.13 ± 0.05	-	-*	4.67 ± 0.1	(5)
KID 5108214	6000 ± 50	6050 ± 25	5844 ± 75	0.3 ± 0.1	0.3	0.2 ± 0.1	4.0 ± 0.1	3.95 ± 0.05	3.80 ± 0.01	(6)
HD 49674	5650 ± 50	5600 ± 25	5632 ± 31	0.2 ± 0.1	0.2	0.33 ± 0.01	-	4.35 ± 0.05	4.48 ± 0.12	(7)

*No Fe II lines are shortlisted for EW determination.

References: (1) Blanco-Cuaresma *et al.* (2014); (2) Soubiran *et al.* (2010) ; (3) Paletou *et al.* (2015);

(4) Butler *et al.* (2000); (5) McDonald, Zijlstra and Boyer (2012);

(6) KEPLER CFOP (https://cfop.ipac.caltech.edu) ; (7) Ghezzi *et al.* (2014)

3.3 Error estimation and limitations of the method

The errors and limitations of each of the methods used in *PARAS SPEC* are discussed as follows:

3.3.1 Synthetic spectral fitting

In the synthetic spectral fitting code, the parameters $T_{\rm eff}$, $[Fe/H]$ and log g are fitted simultaneously. The parameter values are estimated by computing χ^2_{min} in a 3 parameter space. Errors on each of the parameters are computed by using constant χ^2 boundaries as confidence limits on the three parameters jointly (Press *et al.*, 1992). The errors shown in Table 3.2 are 68% confidence intervals for the parameters. As discussed previously, the uncertainties on stellar parameters derived from spectra having SNR/pixel less than 80 is large of the order of the grid size of the original library of synthetic spectra due to improper estimation of the stellar continuum. This method yields reliable results only for spectra having SNR/pixel $\geqslant$ 80. Between SNR $80 - 100$, the wavelength region of $6000 - 6500$ $\AA$ can be used for stellar property estimation. However, we loose information on log g which is determined by Mg I lines ($5160 - 5190$ $\AA$). For, SNR $\geqslant$ 100, the method works well to determine all three stellar parameters, $T_{\rm eff}$, $[Fe/H]$ and log g. Large integration time or co-addition of several spectra for faint targets on a small telescope (1.2 m) is required to achieve this. If the stellar continuum is not determined properly this method may lead to erroneous results.

3.3.2 EW method

As mentioned earlier, EW of a line is determined by modelling the spectral profile of the absorption feature of the star by MPFIT function in `IDL` (Markwardt, 2009) as shown in Eq. 3.2. The absorption lines are modelled by Gaussian profile and 1 σ errors on each of the fitting parameters of the function are obtained as given in Markwardt (2009). These errors are used to compute the 1 σ error bars on the obtained EW values for each of the absorption lines. Elemental abundances from the lines are derived using EW values and a stellar model (function of T_{eff}, $[Fe/H]$ and log g) as inputs as shown below. We determine three set of abundances, one on the original set of EWs, one on EW+σ_{EW} and the third set on EW-σ_{EW}. The sets of abundances determined on EW+σ_{EW} and EW-σ_{EW} correspond to the two extreme values of abundances determined as shown in Eq. 3.3 and 3.4.

$$Abundance_{+\sigma} = Abundance(EW + \sigma_{EW}) \tag{3.3}$$

$$Abundance_{-\sigma} = Abundance(EW - \sigma_{EW}) \tag{3.4}$$

For each set of Abundances, Abundance$_{+\sigma}$ and Abundance$_{-\sigma}$, and different stellar models we derive a set of best-fit parameters, T_{eff}, $[Fe/H]$ and log g in the same way as described earlier. This provides an upper and lower-limits on each of the best-fit parameters of T_{eff}, $[Fe/H]$ and log g.

Table 3.3: Typical errors on Individual Parameters by EW method from PARAS SPEC

SNR/pixel	Error bars T_{eff} (K)	Error bars log g dex
$50 - 80$	±100	0.15
$80 - 120$	±50	±0.1
$\geqslant 120$	±25	±0.05
$**$ 50	±50	±0.1

$**$ From Blanco-Cuaresma *et al.* (2014)

Fast rotating stars will have line blends and will pose difficulty in measuring accurate EW of the lines. Visual inspection for all the lines, despite being a cumbersome task, is necessary to cross-check and discard line blends and improper fits. The typical error bars for different SNR/pixel values obtained on estimation of T_{eff} and log g by *PARAS SPEC* are given in Table 3.3. The last row shows typical uncertainties on similar parameters from Blanco-Cuaresma *et al.* (2014) as discussed in the following section. Thus, this method can be applied on stars having low SNR/pixel between $(50 - 80)$ unlike the synthetic spectral fitting method for determination of stellar parameters though with larger error bars as indicated in Table 3.3.

3.3.3 Comparison with similar work done by others

Blanco-Cuaresma *et al.* (2014) applied the synthetic spectral fitting and EW methods on many stars. Based on the results applied to several stars, the average errors determined for these methods on the respective parameters are given in the last row of Table 3.3. It is important to note that these are average errors reported on an average SNR/pixel of 50. Thus, errors given in Table 3.2 only correspond to the fitting errors and are formal errors on each parameter. As quoted by Smalley (2005), realistically the typical errors on the atmospheric parameters of a star determined by any method are of the order of ± 100 K for T_{eff}, ± 0.1 dex for $[Fe/H]$ and ± 0.2 dex for log g. The exact magnitude of the uncertainty will depend upon the sensitivity of the lines used in the analysis. Mortier *et al.* (2014) have compared the accuracies of the atmospheric parameters obtained by photometry, spectroscopy and asteroseismology and find asteroseismology to yield the most reliable results.

3.4 Conclusions

The stellar parameters derived from the code *PARAS SPEC* agree well with those reported in literature as indicated in Table 3.2. Torres, Andersen and Giménez (2010) studied a large sample of EBs which have masses, radii and stellar parameters studied at a precision as high as 3%. From this study, the authors reported an empirical relationship of mass and radius of stars above 0.6 $M_{\odot}$ as a function of the T_{eff}, $[Fe/H]$ and log g as follows:

$$logM = a_1 + a_2X + a_3X^2 + a_4X^3 + a_5(log\ g)^2 + a_6(log\ g)^3 + a_7[Fe/H] \quad (3.5)$$

$$logR = b_1 + b_2X + b_3X^2 + b_4X^3 + b_5(log\ g)^2 + b_6(log\ g)^3 + b_7[Fe/H] \quad (3.6)$$

where X = $\log(T_{\text{eff}}) - 4.1$. The calibration coefficients a_i and b_i are given in Torres, Andersen and Giménez (2010). The reliability of stellar parameters derived from high-resolution spectroscopy is expected to be better than compared by modelling photometry data (Casagrande *et al.*, 2011). Thereby, this code can be used to deduce the masses and radii of primary stars at higher accuracies leading to precise determination of stellar parameters of the secondary component.

Chapter 4

Decoding three F+M Eclipsing Binary systems

4.1 Introduction

Determining the masses of the VLMS occurring as a part of the EB system, characterizing their orbital parameters, and investigating the empirical M-R relationship, form the essence of this thesis. As discussed in Ch 1, high precision spectroscopy and photometry measurements are a pre-requisite to infer the masses and radii of stars occurring in EBs. Based on the criteria mentioned in Ch 3, EB candidates are carefully shortlisted. F-type primaries with M-type secondaries (hereafter F+M binaries) are often discovered in surveys, which are designed primarily to search for transiting planets (e.g. Bouchy *et al.* (2005); Beatty *et al.* (2007)). Over the last few years only a handful of F+M binaries have been discovered and their properties determined (e.g. Pont *et al.* (2005a,b, 2006); Fernandez *et al.* (2009)). Due to the paucity of such studies, therefore, every additional system discovered and analyzed contributes significantly to our understanding of fundamental stellar properties; thus making the sample of F+M binaries an important subset of stellar studies. Here, in this Chapter we present our investigations on three F-type sources, HD 213597, HD 23765 and SAO 106989, shortlisted from the *STEREO* and *SuperWasp*

(SW) photometry catalogue. Here, we describe high- resolution spectroscopic and photometric observations and the methods of analysis used to derive the physical parameters concerning the three EBs. Discussion and conclusions of this work are presented at the end of the Chapter.

4.2 Mass and orbital parameters of a low-mass star HD 213597B

As one of the important by-products of their quest for exoplanets, Wraight *et al.* (2011) catalogued 263 EB candidates from a careful analysis of *STEREO* data. HD 213597 was particularly highlighted by these authors for potentially hosting a substellar companion. SIMBAD database noted the star to have a spectral type F0 with no reported variability. The star is shown to have box-shaped eclipses of 25 mmag in depth at a periodicity of 2.4238 d (Wraight *et al.*, 2011). This star, as a result of the detailed work done by Wraight *et al.* (2012) on *STEREO* photometry data, also formed a part of their study on 9 low mass EB candidates where the radius of the secondary is estimated to be below 0.4 $R_{\odot}$. HD 213597, with a visual magnitude of 7.8, is an F-type star having a rotational velocity of 40 $\pm$ 4 km s^{-1} (Nordström *et al.*, 2004; Głębocki and Gnaciński, 2005). The radius measurement for this star is 2.039 $R_{\odot}$ based on 2MASS photometry measurements by Masana, Jordi and Ribas (2006) whereas those derived by the photometry measurements from *STEREO* is 1.96 $\pm$ 0.06 $R_{\odot}$ (Wraight *et al.*, 2012). Nordstrom *et al.* (1997) took 4 RV measurements of this source and found a reflex motion of around 60 kms^{-1} suggesting the possible existence of a low-mass companion in contrast to the suggestion of a brown-dwarf companion by Wraight *et al.* (2011). Based on photometry, the radius estimates of the secondary indicates the possibility of a low-mass companion (Wraight *et al.*, 2012). Table 4.1 lists the properties of this star obtained from the literature.

Table 4.1: Stellar properties of host star HD 213597 from literature.

Parameter	Value	Reference
Mass	1.5 $\pm$0.1 $M_\odot$	(1)
Radius	2.039$\pm$0.303 $R_\odot$	(2)
log g	3.99$\pm$0.05	(1)
$v \sin i$	40$\pm$5 km s^{-1}	(3)
$T_{\rm eff}$	6837$\pm$80 K	(1)
$[Fe/H]$	$-$0.14$\pm$0.1	(1)
Age	1.90$\pm$0.2 Gyr	(1)
Distance	115 $\pm$15 pc	(4)
V magnitude	7.8	(5)
RA(epoch=2000)	22^h 32^m 32^s.626	(5)
Dec(epoch=2000)	1° 34' 56.83 "	(5)

References: (1) Casagrande *et al.* (2011); (2) Masana, Jordi and Ribas (2006); (3) Nordström *et al.* (2004); (4) from HIPPARCOS data (5)from SIMBAD

4.2.1 Spectroscopic and Photometric Observations of HD 213597

4.2.1.1 Spectroscopy

High-resolution spectroscopic observations of the star HD 213597 were made on several occasions during 2011-12 with the fiber-fed high-resolution spectrograph (hereafter HRS; Tull, 1998) at the 10-m McDonald Hobby-Eberly Telescope (hereafter HET; Ramsey *et al.*, 1998), and the fiber-fed echelle spectrograph, PARAS (Chakraborty *et al.*, 2014) at the 1.2-m telescope at Gurushikhar Observatory, Mount Abu, India.

HET-HRS observations: A set of 9 observations were obtained between 2011 October and 2012 July using the HRS in its 316g5936 cross-disperser setting. The data at HET-HRS were obtained with a 2 arcsec diameter fiber with options for different resolving power; 15,000, 30,000, 60,000 and 1,20,000 based on different slit widths. We took observations at a resolving powers of 30,000 with a data binning of 2×3 pixels. A simultaneous coverage in two wavelength regions of $4300 - 5800$ $\mathring{A}$ and $6200 - 7600$ $\mathring{A}$ was recorded. The two distinct portions of wavelength coverage correspond to two mosaics of the R4 echelle having a wavelength coverage at the blue end and a wavelength coverage at the red end with a gap of 5 orders in between. The exposure times ranged between 60 s and 300 s yielding signal-to-noise ratio (SNR) between 200 and 600 per resolution element. Since, each resolution element in the 30,000 resolving power mode is 2.7 pixels, the SNR per pixel is between 74 to 222 for the observed data. Each observation was bracketed before and after with a ThAr lamp exposure for wavelength calibration. The same procedure was used on another star HD 215648, which served as a template to derive RVs. The template star is used for computing cross-correlation functions for deriving RVs in lieu of the numerical mask used to derive RVs as discussed in Ch 2. HD 215648 has a spectral type of F7V with $T_{\rm eff} = 6228 \pm 100$ K, log $g = 4.15 \pm 0.07$ (Edvardsson *et al.*, 1993), $v \sin i = 6.7 \pm 0.7$ km s^{-1} (Ammler-von Eiff and Reiners, 2012), and $[Fe/H] = -0.22$ (Valenti and Fischer, 2005). The data were reduced using a custom optimal extraction pipeline as described in Bender *et al.* (2012).

Mt Abu-PARAS observations: A total of 13 observations were taken between October and November 2012 using the fiber-fed PARAS spectrograph at a resolving power of 67,000. The exposure time for each observation was fixed at 1200 s resulting in SNR between 20 to 25 per pixel at the blaze wavelength. Simultaneous exposures of the science target and the ThAr lamp for wavelength calibration were taken. The wavelength region between 3700 and 6800 Å was considered for the RV measurements. The data were reduced by the Interactive Data Language (`IDL`) pipeline designed specifically for PARAS as described in Ch. 2. Over the course of one year (October 2011 - November 2012), a combined total of 22 observations were obtained with the two spectrographs. The barycentric corrected RV values along with the associated uncertainties (Refer § 4.2.2.2) are given in Table 4.2.

Table 4.2: RV Observation log for the star HD 213597.

UT Date	T-2,400,000 (BJD-TDB)	Instrument (flag)	Exp. Time (sec.)	RV (km s^{-1})	σ-RV (km s^{-1})
2011 Oct 30	55864.689	HET-HRS	250	4.844	0.209
2011 Nov 25	55890.614	HET-HRS	60	11.822	0.208
2011 Nov 27	55892.609	HET-HRS	180	−20.967	0.214
2011 Dec 15	55910.552	HET-HRS	60	15.026	0.212
2012 Jun 11	56089.949	HET-HRS	300	14.561	0.210
2012 Jun 22	56100.924	HET-HRS	300	−30.586	0.217
2012 Jun 23	56101.918	HET-HRS	300	19.909	0.212
2012 Jul 01	56109.905	HET-HRS	180	−27.993	0.204
2012 Jul 02	56110.901	HET-HRS	300	−9.125	0.214
2012 Oct 17	56218.260	PARAS	1200	2.940	0.187
2012 Oct 17	56218.276	PARAS	1200	2.905	0.214
2012 Oct 17	56218.292	PARAS	1200	2.134	0.266
2012 Oct 18	56219.210	PARAS	1200	−61.491	0.221
2012 Oct 18	56219.225	PARAS	1200	−61.522	0.256
2012 Oct 18	56219.241	PARAS	1200	−62.592	0.288
2012 Oct 23	56224.198	PARAS	1200	−62.984	0.200
2012 Oct 23	56224.214	PARAS	1200	−62.904	0.216
2012 Nov 7	56239.202	PARAS	1200	−42.605	0.583
2012 Nov 7	56239.219	PARAS	1200	−40.721	0.747
2012 Nov 7	56239.234	PARAS	1200	−39.516	0.665
2012 Nov 8	56240.179	PARAS	1200	0.438	0.223
2012 Nov 8	56240.195	PARAS	1200	−1.008	0.248

The time in UT and BJD-TDB are mentioned in first two columns followed by instrument flag used for observations and exposure time in third and fourth column respectively. The last column has RV errors, corresponding to co-variant errors (HET-HRS) or statistical photon noise errors (PARAS).

4.2.1.2 Transit Photometry

Ground-based photometric observations for HD 213597 were performed from the calculated mid-eclipse time based on the ephemeris of Wraight *et al.* (2012). Given the celestial coordinates of the star (Refer Table 4.1) and the period of monsoon in India from middle of June to early October, a narrow window of three weeks was available in the month of October to observe the complete transit of the object. Thus, the archival *STEREO* data (Wraight *et al.*, 2012) was also revisited, in order to compute the transit parameters such as transit duration and angle of inclination in combination with our ground-based photometry at PRL, Mount Abu, India.

***STEREO* archival data:** *STEREO* data from HI-1A instrument were extracted from the UK Solar System Data Centre (UKSSDC) website [1]. The star was observed for a period of 16 to 17 days on the CCD for each cycle of observation. Six such cycles of data were used for HD 213597 during the period from January 2008 to October 2012. For this purpose, we utilized the L2 images that were pre-processed (bias-subtracted and flat-fielded) and accounted for solar coronal contamination. The wavelength band of $6300 - 7300$ $\mathring{A}$ was used for observation (Wraight *et al.*, 2012). A total of 36 transits for HD 213597 were recorded in 6 cycles of the extracted data.

Mt. Abu observations: Follow-up photometric observations of HD 213597 were also made with the Physical Research Laboratory (PRL) 10-inch telescope at Gurushikhar, Mount Abu, India. Photometry was carried out with Bessel R-band filter on 2013 October 21 UT for a duration of 5 h. The telescope is equipped with a back thinned E2V 1k $\times$ 1k CCD array giving a field of view of 35 arcmin $\times$ 35 arcmin. A mismatch of the telescope dome position while guiding resulted in the rejection of an hour-long observation corresponding to the phase between mid-eclipse duration and the egress of the eclipse. Furthermore, due to passing clouds, we lost about 20 per cent of the egress time.

[1] www.ukssdc.rl.ac.uk

Despite the data loss, we recorded the transit at a confidence level of 4σ. The observations on this source, HD 213597 discussed in this section, as well as the analysis and results discussed in the next sections, have been published in Chaturvedi *et al.* (2014).

4.2.2 Data Analysis of HD 213597

4.2.2.1 Radial Velocity Analysis

HET-HRS: The reduced data were wavelength-calibrated and continuum-normalized and the echelle orders were stitched to produce a continuous 1-D spectrum between two wavelength regions of $4300 - 5800$ $\mathring{A}$ and $6200 - 7500$ $\mathring{A}$. The spectrum was then divided into 8 segments ($4386 - 4486$ $\mathring{A}$; $4593 - 4843$ $\mathring{A}$; $4925 - 5025$ $\mathring{A}$; $5100 - 5410$ $\mathring{A}$; $5475 - 5800$ $\mathring{A}$; $6365 - 6430$ $\mathring{A}$; $6620 - 6850$ $\mathring{A}$; $7450 - 7500$ $\mathring{A}$) that were free of telluric lines. Each segment was cross-correlated using a 1D cross-correlation algorithm. The resulting 1D correlation arrays were combined using the maximum likelihood method which is based on the the probability of the observed results under the assumed model as a function of model parameters (Zucker, 2003). A robust non-linear least square curve fitting algorithm was employed in MPFIT in `IDL`, to fit the peak of the cross-correlation function and determine the RVs and the associated errors. The barycentric corrections were incorporated on individual data points by `IDL` routines.

Mt Abu-PARAS: The entire reduction and analysis for PARAS was carried out by the custom-designed pipeline in `IDL`-based on the REDUCE optimal extraction routines of Piskunov and Valenti (2002). The pipeline performs the routine tasks of cosmic ray correction, dark subtraction, order tracing, and order extraction. A complete thorium line list for the PARAS spectral range was utilized. The wavelength calibration algorithms were specifically optimized for PARAS as described in Ch. 2. The RV values were computed by cross-correlating the observed spectra against an F-type binary mask. The binary

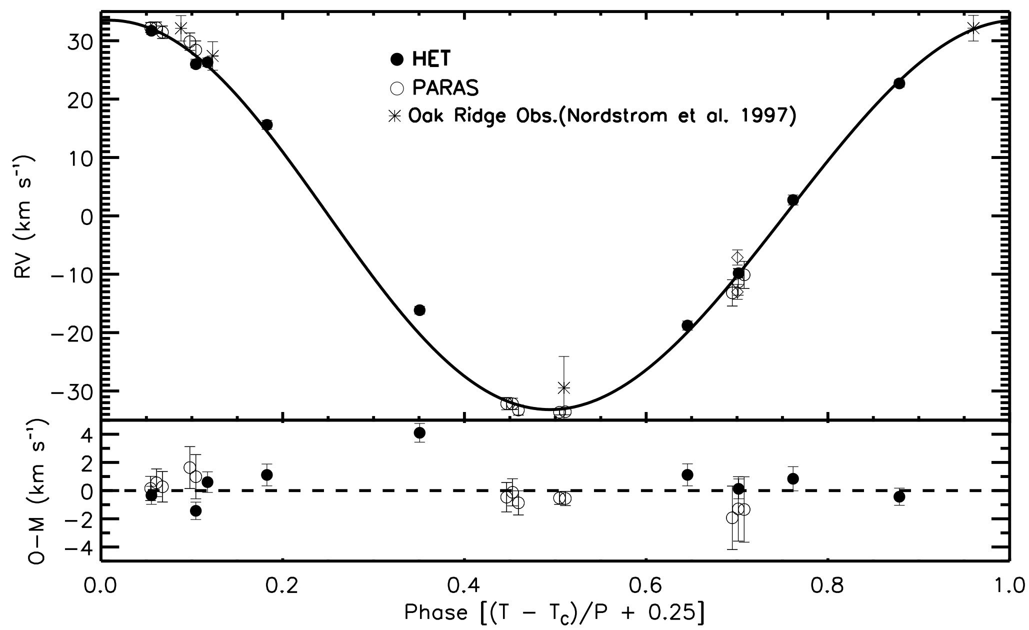

Figure 4.1: (Top panel) RV model curve for star HD 213597 obtained from EXOFAST is plotted against orbital phase. HRS-HET (filled circles) and PARAS, Mount Abu (open circles) observed data points along with the estimated errors are overplotted on the curve. The 4 RV measurements (not considered for RV fitting) from Nordstrom *et al.* (1997) are overplotted on the modelled data.
(Bottom panel) The residuals from best-fit are plotted below the RV plot. The residuals are not plotted for the points which are not considered for the RV fitting. For better visual representation, the x axis (Phase) is shifted by 0.25 so that the central primary transit crossing point (T_c) occurs at phase 0.25 instead of 0.

mask was created with the `SPECTRUM` program using Kurucz stellar atmosphere models (Kurucz, 1993) with a temperature of $T_{\rm eff} = 6750$ K, log $g = 4.0$ and a metallicity, $[M/H] = -0.2$ (refer Table 4.1) by retrieving a list of Fe I and Fe II lines having an intensity value between 1 and 0 depending on the strength of the transition. The central wavelength of each line was broadened to a width of 20 km s^{-1} (an average $v \sin i$ for F-type stars (Nordstrom *et al.*, 1997)). Barycentric corrected RV points are shown in Fig 4.1. Filled circles indicate data taken with HET-HRS and open circles indicate RV points observed by Mt Abu-PARAS. More details on the fitted model indicated as a solid line in the figure are discussed in § 4.2.2.6.

4.2.2.2 Errors on RV Measurements

The cross-correlation function (CCF) for each epoch was computed for the fully reduced and calibrated spectra as discussed in next section. RVs were determined by fitting the CCF with a Gaussian function. The co-variant errors obtained from fitting the peak of this CCF in `IDL` are reported as uncertainties on the HET data. The precision on RV measurements is dependent on photon noise errors as discussed in § 2.3. For PARAS spectra, errors based on photon noise were computed for each spectrum as discussed in Bouchy, Pepe and Queloz (2001). These authors defined a term quality factor, Q (described in § 2.3), which controls the RV precision as given:

$$\delta V_{rms} = \frac{c}{Q\sqrt{N_{e^-}}} \tag{4.1}$$

where,

$$Q = \frac{\sqrt{\sum W(i)}}{\sqrt{\sum A_0(i)}} \tag{4.2}$$

and A_0(i) is the intensity of a zero-velocity spectrum at the ith pixel and $W(i)$ is the optimum weight of the individual pixel, which is inversely proportional to the square of the individual velocity dispersion. As mentioned earlier, HD 213597 is an early F-type star with a rotational velocity of 40 km s^{-1}. Q deteriorates with increasing rotational velocity thereby increasing the RV uncertainty. The F-type star, HD 213597, consequently will have the RV uncertainty 20 times larger than a Sun-like star. While PARAS has much higher resolution than the HET-HRS mode that was used, SNR of its spectra are lower, leading to the PARAS RVs having larger uncertainties than the HET-HRS RVs. In order to compute errors by statistical approach, we randomly varied the signal on each pixel within the Poissonian uncertainty of $\pm\sqrt{N}$, where N is the signal on each pixel, and thereafter computed the CCF for each spectra. This process is repeated 100 times for each spectra and the standard deviation of the distribution of the obtained RV values is given as the 1 σ

uncertainty on the CCF fitting along with errors from photon noise on each RV point.

4.2.2.3 Spectral Analysis of HD 213597

The spectral analysis of HD 213597 was done by the SME (Valenti and Piskunov, 1996) spectral synthesis code using HET-HRS observed spectra. We also repeated the spectral analysis for this star from Mt Abu-PARAS observed spectra from the in-house built spectral analysis code, *PARAS SPEC*. The details are discussed as follows.

SME: SME is composed of a radiative transfer engine that generates synthetic spectra from a given set of trial stellar parameters and a Levenberg-Marquardt solver. This non-linear least square fitting method works on the principle where the parameters of the models are minimized to keep the sum of squares of the observed and model points minimal (Press *et al.*, 1992). It is used to find a set of parameters corresponding to a synthetic spectrum that best matches the observed input data in specific regions of the spectrum. The basic parameters used to define a synthetic spectrum are effective temperature ($T_{\rm eff}$), surface gravity ($\log g$), metallicity ($[M/H]$), iron abundance relative to solar ($[Fe/H]$) and projected rotational velocity ($v \sin i$). These five parameters were solved in order to match the observed spectrum.

SME was implemented by using the Advanced Computing Centre for Research and Education's (ACCRE) High-Performance Computing Centre at Vanderbilt University for a large number (150) of different initial conditions to fully explore the χ^2 space and find the optimal solution at the global minimum. In addition, a line list based on Stempels *et al.* (2007) suited for F-type stars and the MARCS model atmosphere grid in the radiative transfer engine was applied. The microturbulence ($v_{\rm micro}$) defined in Gómez Maqueo Chew *et al.* (2013) was obtained from the polynomial relation.

SME pipeline was applied to the high SNR HET spectrum of HD 213597 allowing all 5 parameters listed above to vary freely. The results of the execution

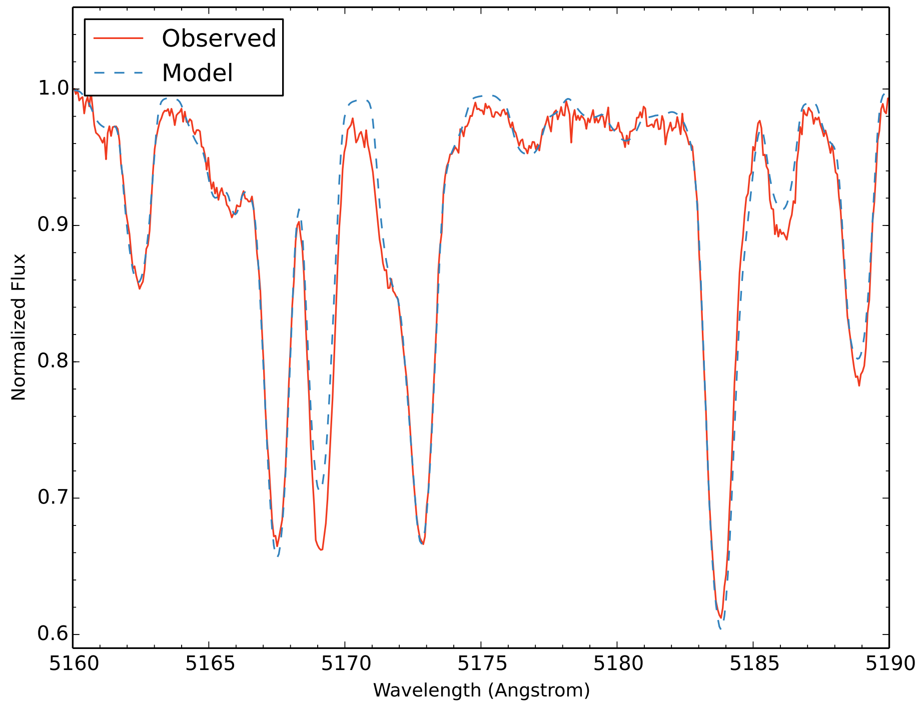

Figure 4.2: Observed normalized spectra for star HD 213597 (solid line) plotted across the wavelength region of 5160 − 5190 $\mathring{A}$ covering the Mg I triplet at 5167, 5172, and 5183 Å. Overplotted is the modelled spectra (dash line) obtained from SME analysis (when all parameters are kept free), with temperature value of $T_{\rm eff}$ of 6625 K, $[Fe/H]$ of 0.095 and log g of 3.72.

provide us with the following values: $T_{\rm eff} = 6625 \pm 121$ K, log $g = 3.72 \pm 0.22$, and $[Fe/H] = -0.095 \ \pm\ 0.08$. It is important to note that for hotter stars, uncertainties on the gravity derived from spectral synthesis increase because the wings of the Mg I b triplet at 5167, 5172, and 5183 Å used to constrain this parameter become narrower and less sensitive to gravity. SME pipeline was re-run, this time constraining log $g \ = \ 3.96 \pm 0.1$ based on the literature-cited value. In this set of 150 trials, we fixed the value of gravity to a randomly chosen value within the range of uncertainty and solve for the other 4 parameters. For the constrained run, we obtained $T_{\rm eff} \ = \ 6752 \ \pm \ 52$ K, iron abundance $([Fe/H]) = -0.025 \ \pm\ 0.05$ and metallicity $([M/H]) = -0.105 \ \pm 0.03$.

The formal 1-σ errors are based on the $\delta\chi^2$ statistics for the 5 free parameters. The systematic uncertainties on each parameter are obtained by

Table 4.3: Spectroscopically determined stellar parameters of HD 213597 (this work). The two measurements listed for each stellar parameter results from two SME run: (1) when all parameters are allowed to float; (2) when log g is fixed to a value determined by mass and radius measurements.

Stellar Parameter	Value (Free)	Uncertainty	Value (Constrained)	Uncertainty
$T_{\rm eff}$ (K)	6625	$\pm$ 121	6752	$\pm$ 52
log g	3.72	$\pm$ 0.22	3.96	$\pm$0.1
$[Fe/H]$	-0.095	$\pm$ 0.08	-0.025	$\pm$ 0.05
$[M/H]$	-0.156	$\pm$ 0.03	-0.105	$\pm$ 0.03
$v \sin i$ (km s^{-1})	39.53	$\pm$ 1.3	39.53	$\pm$ 1.3
$v_{\rm micro}$ (km s^{-1})	2	$--$	2	$--$

computing the mean absolute deviations from a comparison of the results of the pipeline with three independent datasets with parameters in the literature (Valenti and Fischer, 2005; Torres *et al.*, 2012; Huber *et al.*, 2013). The final results (both free and constrained log g) are listed in Table 4.3 along with their combined statistical and systematic uncertainties. Fig. 4.2 shows a sample of the observed spectrum (solid line) overlaid by the best-fit model (dotted line) obtained by a free parameter fit ($T_{\rm eff} = 6625$ K; $[Fe/H] = -0.095$; log $g = 3.72$). The observed and model spectra are shown across the wavelength region $5160 - 5190$ $\AA$, that includes the Mg I b triplet.

PARAS SPEC: *PARAS SPEC* was used for determination of stellar properties for HD 213597 from PARAS observed spectra. Though, the code has a provision of using both the synthetic spectral fitting and equivalent width (EW) methods, we could only use the first method of synthetic spectral fitting on this star. The EW method requires a set of unblended Fe I and Fe II lines for determination of stellar properties. Since, the star has a large $v \sin i$ of

40 km s^{-1}, the Fe II lines for this star were blended rendering the usage of EW method impossible on this star. A total of 15 observed spectra were co-added for the source to get a SNR of $90 - 120$ in the entire wavelength range to be used ($5050 - 6500$ $\AA$).

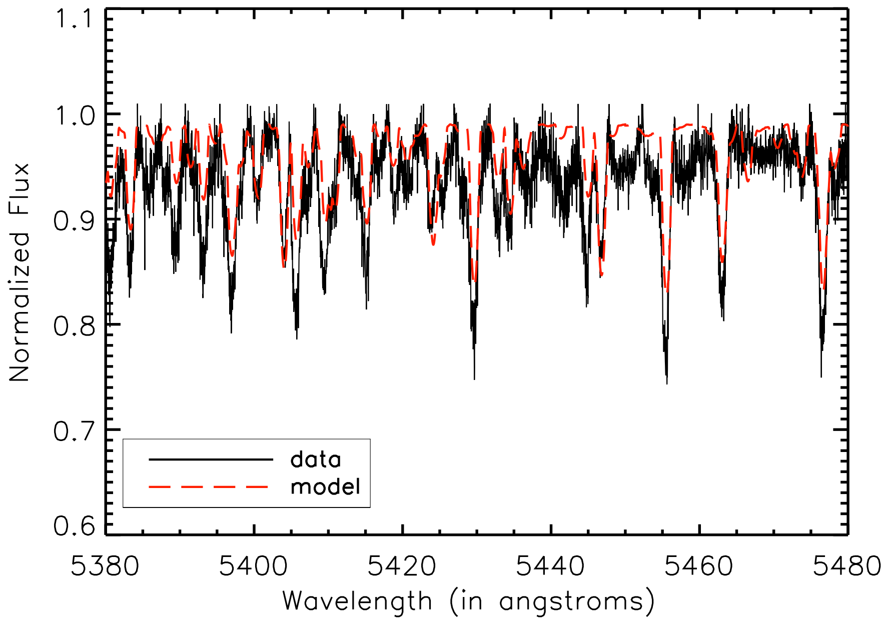

Figure 4.3: Observed normalized spectra for HD 213597 (solid black line) plotted across the wavelength region of $5380 - 5480$ $\AA$. Overplotted is the modelled spectra (red dash line) obtained from PARAS SPEC analysis, with temperature value of $T_{\rm eff} = 6550 \pm 100$ K, $[Fe/H] = -0.1 \pm 0.1$ and log $g = 4.0 \pm 0.1$.

Thus, we utilized the wavelength region of $5050 - 6500$ $\AA$ for spectral analysis. All three parameters, $T_{\rm eff} = 6550 \pm 100$ K, $[Fe/H] = -0.1 \pm 0.1$ and log $g = 4.0 \pm 0.1$ are determined by this method. The best-fit model spectra determined for HD 213597 is shown in Fig. 4.3.

4.2.2.4 Transit of HD 213597

***STEREO* archival data:** The *STEREO* images from Heliospheric Imager, HI-1A, L2 data were previously bias and flat-field corrected. These images have a field of view of $20° \times 20°$ imaged on a 2k $\times$ 2k CCD. The data were

2 × 2 binned to get a 1k × 1k image with a field of view of 70 arcsec × 70 arcsec per pixel.

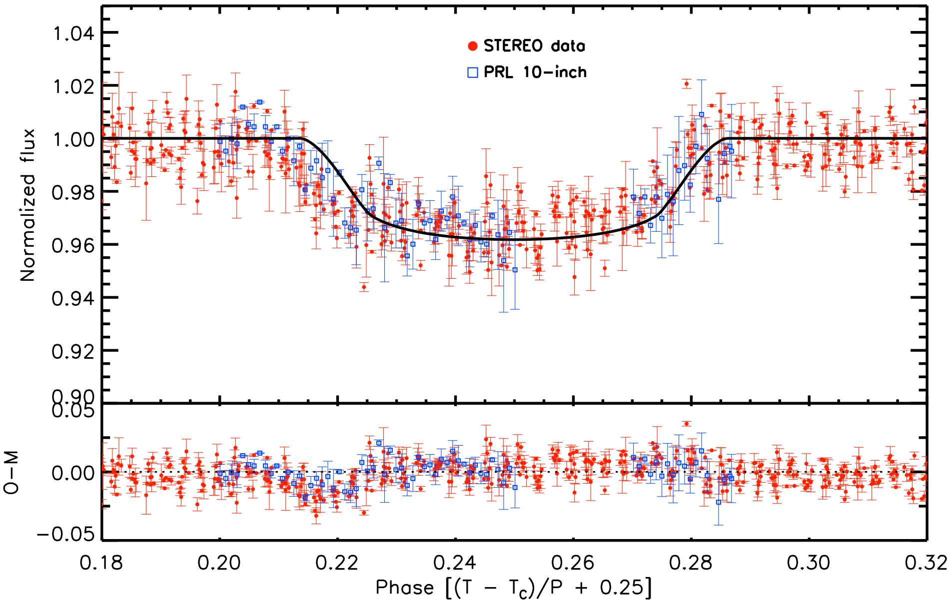

Figure 4.4: (Top panel) Transit curve obtained from *STEREO* data and PRL 10-inch telescope is plotted based on the parameters from EXOFAST. The *STEREO* data are plotted with red filled circles and the PRL 10-inch telescope data are plotted with open blue squares along with their individual error bars. (Colours are only in online version.) (Bottom panel) Observed-Fit residuals are plotted. For better visual representation, the x axis (Phase) is shifted by 0.25 so that the central primary transit crossing point (T_c) occurs at phase 0.25 instead of 0.

Each image is a sum of 30 exposures with a total exposure time of 20 min and an observational cadence of 40 min (Wraight *et al.*, 2011). The procedure given in Sangaralingam and Stevens (2011) was followed to do aperture photometry on the data. An aperture of 3.5 pixels was chosen for the same. The standard IRAF [2] `daophot` package for processing the photometry data was used. The flux computed by IRAF was detrended by fitting a 4^{th} order polyno-

[2]IRAF is distributed by the National Optical Astronomy Observatory, which is operated by the Association of Universities for Research in Astronomy, Inc., under cooperative agreement with the National Science Foundation.

mial to account for the CCD response function as discussed in Sangaralingam and Stevens (2011). The data were further normalized for each cycle. The `rms` scatter on the light curve for the entire data for the source star outside the transit time duration is 7 mmag. A total of 36 transits were obtained for the entire data of 6 cycles between the period January 2008 to October 2012.

Mt Abu data: For the ground-based photometry observations from Mt Abu on 21 October 2013, each individual frame had an exposure time of 2 s and a readout time of $\sim$ 1 s. Similar to the *STEREO* data, IRAF `daophot` package was used to perform aperture photometry on the data, after the frames were flat-fielded and dark-corrected.

For differential photometry, a comparison star is needed which is non-varying with time and is similar in colour and magnitude to the program star. In order to cross check the non-variability of the comparison star, another field star called 'check star' is required. Varying air-mass, and other local sky variations were accounted for, to an extent, by performing differential photometry on the comparison star and the check star. HD 213763 with spectral type F5V and a visual magnitude of 7.8 was chosen as the comparison star and HD 213598 of spectral type K0V with a visual magnitude of 9.14 was chosen as the check star. Although it is desirable to choose a check star of similar colour as that of the source and comparison stars, a K-type check star was selected due to unavailability of bright field stars in the near vicinity. Since, Bessel R-band was used for photometry observations, the effect of scattering by moonlight and the atmospheric extinction is minimal.

The average SNR of the source and the comparison star was between 300 and 350 respectively for individual frames. Sixty consecutive frames, of similar exposures were median combined to avoid the scintillation noise from sky which, otherwise, becomes the dominant source of noise. Thus, each binned data frame comprised a total exposure time of 120 s and a total time cadence of 202 s (including the read out time) making the SNR of the combined frame to be $\sim$ 2500 for the same stars. Differential photometry was performed on the program star, HD 213597 and the comparison and check stars (HD 213763 and HD 213598). Individual light curve of comparison and check stars showed a `rms` scatter of 12 mmag over the entire observation period. The `rms` scatter between the comparison and the check star reduced to 6 mmag after differential photometry. This scatter was considered as photometric errors on each data point in the light curve. The data from *STEREO* and PRL 10-inch telescope were combined to produce a phase-folded light curve as both the datasets were observed in R-band and have similar associated photometric errors. This phase-folded light curve is shown in Fig. 4.4 where red points indicate data from *STEREO* and blue points refer to Mt Abu 10 inch telescope data. Details on the model which is shown as a solid line in the figure are discussed in § 4.2.2.6.

4.2.2.5 EXOFAST: A tool to fit spectroscopy and photometry data

EXOFAST is a set of `IDL` routines designed to fit transit and/or RV variations (Eastman, Gaudi and Agol, 2013), and characterize the parameter uncertainties and covariances with a Differential Evolution Markov Chain Monte Carlo method (Johnson *et al.*, 2011). It can either fit RV and transit values exclusively or use both datasets to give a simultaneous fit. It also requires priors on T_{eff}, log g and iron abundance, $[Fe/H]$. EXOFAST uses empirical polynomial relations between masses and radii of stars as given in Eqns. 3.5 and 3.6; their log g, T_{eff}, and $[Fe/H]$ based on a large sample of non-interacting binary stars in which all of these parameters were well-measured (Torres, Andersen and Giménez, 2010). These priors are used as a convenient way of modelling isochrones and are fast enough to incorporate them at each step in Markov chain. The errors derived here are determined by evaluating the posterior probability density based on the range of a given parameter that encompasses some set fraction of the probability density for the given model. The errors reported here for the mass and radius of the secondary are formal errors from EXOFAST. These values and errors are themselves based on models and isochrones and should not be used as independent observational checks on these models until more precise values can be derived in the future by teasing out a double lined spectroscopy orbital solution for any of the EB system studied.

4.2.2.6 Orbital parameters derived for star HD 213597

The EXOFAST routine is executed with the combined RV datasets (HET-HRS and PARAS) and the combined photometry datasets (one from the transit light curve obtained by *STEREO* and the other one obtained by PRL 10-inch telescope). On varying the SME-derived parameters as input priors to EXOFAST, it is found that constraining log g with the same uncertainties as given in Table 4.3 yields the most consistent values for $T_{\rm eff}$ and $[Fe/H]$ (best simultaneous fit for RV and transit data). The results of the execution are summarized in Table 4.4. Fig. 4.1 illustrates the RV versus orbital phase for HD 213597. As discussed previously, solid and open circles (top panel) show RV measurements of the primary taken with the HRS and PARAS instruments, respectively. The figure also shows the residuals (Observed-Model) in the bottom panel. There were four RV measurements for this star from Nordstrom *et al.* (1997) observed with the 1.5-m Wyeth reflector at the Oak Ridge Observatory in Harvard, Massachusetts between October 1987 to July 1991. The offset in RV are corrected for and these points are overplotted in Fig. 4.1. However, these points are not included while modelling RV due to their relatively large errors. It is important to note that despite a long time-gap between the observations from this work and those of Nordstrom *et al.* (1997), their RV measurements (asterisks) lie reasonably close to the model curve as shown in Fig. 4.1.

Fig. 4.4 (upper panel) shows the simultaneous fit for the transit light curve obtained by analysing *STEREO* archival data (filled circles) and PRL 10-inch telescope data (open squares), overplotted with the model derived from EXOFAST (solid curve). The residuals are plotted in lower panel. The simultaneous fit gives us a transit depth of $0.0317^{+0.0013}_{-0.0012}$ mag, angle of inclination of $84.9^{\circ}{}^{+0.62}_{-0.5}$ and a transit time duration of 274^{+5}_{-4} min. The transit depth cited here is consistent with the refined analysis of *STEREO* light curve by Whittaker, Stevens and Sangaralingam (2013). We obtain the mass of the secondary

Table 4.4: Results obtained from EXOFAST by simulataneous fitting of RV and transit data for HD 213597 with a 68% confidence interval.

Parameter	Units	Values
HD 213597A:		
M_A	Mass ($M_\odot$)	$1.293^{+0.12}_{-0.1}$
R_A	Radius ($R_\odot$)	$1.973^{+0.085}_{-0.080}$
L_A	Luminosity ($L_\odot$)	$7.04^{+0.60}_{-0.52}$
ρ_A	Density (cgs)	$0.2377^{+0.0054}_{-0.0053}$
$\log g_A$	Surface gravity (cgs)	3.96 ± 0.01
$T_{\rm eff}$	Effective temperature (K)	6699^{+53}_{-52}
[Fe/H]	Iron Abundance	$-0.065^{+0.050}_{-0.048}$
HD 213597B:		
e	Eccentricity	$0.0198^{+0.0094}_{-0.0091}$
ω_*	Argument of periastron (degrees)	72^{+12}_{-18}
P	Period (days)	$2.4238503^{+0.000017}_{-0.0000019}$
a	Semi-major axis (AU)	$0.04112^{+0.00058}_{-0.00057}$
M_B	Mass ($M_\odot$)	$0.286^{+0.012}_{-0.01}$
R_B	Radius ($R_\odot$)	$0.344^{+0.097}_{-0.01}$
ρ_B	Density (cgs)	$9.32^{+0.43}_{-0.41}$
$\log g_B$	Surface gravity	$4.803^{+0.0093}_{-0.0097}$
RV Parameters:		
$e\cos\omega_*$	$0.0056^{+0.0043}_{-0.0042}$	
$e\sin\omega_*$	$0.0184^{+0.0096}_{-0.0097}$	
T_P	Time of periastron (BJD)	$2455392.09^{+0.087}_{-0.12}$
K	RV semi-amplitude m s^{-1}	33390^{+290}_{-280}
M_B/M_A	Mass ratio	0.2218 ± 0.0045
γ	Systemic RV m s^{-1}	-4420^{+180}_{-190}
$f(m)$	Mass function * ($M_\odot$)	0.0091 ± 0.000048
Transit Parameters:		
T_C	Time of transit (BJD)	$2455392.2014^{+0.0015}_{-0.0016}$
R_B/R_A	Radius of secondary in terms of primary radius	0.178 ± 0.001
i	Inclination (degrees)	$84.9^{+0.61}_{-0.50}$
a/R_A	Semi-major axis in stellar radii	$4.48^{+0.039}_{-0.038}$
δ	Transit depth	$0.0317^{+0.0013}_{-0.0012}$
T_{14}	Total transit duration (minutes)	274^{+5}_{-4}

* By BOOTTRAN (`IDL`).

as $0.286^{+0.012}_{-0.01}$ $M_{\odot}$ and a radius of $0.344^{+0.097}_{-0.01}$ $R_{\odot}$. The mass function for this system is also calculated by using the IDL BOOTTRAN package (Wang *et al.*, 2012). The results obtained by the combined RV and transit datasets are consistent with the period 2.4238 d (Wraight *et al.*, 2012; Whittaker, Stevens and Sangaralingam, 2013) with a semi-major axis of 4.48 R_{star} (0.041 AU) and a RV semi-amplitude of 33.39 km s^{-1}. Based on the mass limits, it can be concluded that the secondary star is an early M dwarf (Baraffe and Chabrier, 1996).

4.2.3 Results obtained on HD 213597

The detailed spectral analysis of the high SNR HET spectra gives us the following stellar parameters: $T_{\rm eff}$= 6752 $\pm$ 52 K and $[Fe/H]$ = -0.025 $\pm$ 0.05, for log g = 3.96 $\pm$ 0.1. The temperature indicates an F-type primary star. It may be mentioned that Masana, Jordi and Ribas (2006) obtained a $T_{\rm eff}$ of 6936 $\pm$ 70 K based on V and 2MASS *JHK* photometry, while Casagrande *et al.* (2011) reported a value of 6837 $\pm$ 80 K based on improved colour calibration of the same bands. Our results are more reliable than the earlier ones, as they are based on detailed spectral analysis from high SNR spectra. Furthermore, these results are substantiated by the fact that the RV and photometry data are not able to constrain a solution in EXOFAST by using the previously cited $T_{\rm eff}$ value of 6936 $\pm$ 70 K. Using $T_{\rm eff}$, $[Fe/H]$ and log g derived from this work, the mass and radius of the primary star obtained from Mass-Radius relationship (Torres, Andersen and Giménez, 2010) are 1.48 $M_{\odot}$ and 2.11 $R_{\odot}$, respectively, consistent with the values reported in literature (see Table 4.1).

Using high-resolution spectroscopy data taken with the HET-HRS, PARAS spectrographs and photometry with the *STEREO*, PRL 10-inch telescope, it is concluded that HD 213597 is an EB system with an F3-type primary and an early M4-type secondary (spectral types are estimated based on mass (Pecaut and Mamajek, 2013)). The estimated secondary mass from RV measurements is M_B = $0.286^{+0.012}_{-0.01}$ $M_{\odot}$ with an accuracy of $\sim$ 3 $-$ 4% (formal errors). Based on the transit depth of $0.0317^{+0.0013}_{-0.0012}$ mag, the radius of the secondary is estimated to be $R_B = 0.344^{+0.097}_{-0.01}$ $R_\odot$ with an accuracy of $\sim$ $5-6\%$ (formal errors). The radius estimated here is in good agreement with the value given by Wraight *et al.* (2012).

4.3 Mass and orbital parameters for a mid-M dwarf star, HD 23765B

HD 23765 is the second EB target chosen for our study shortlisted from the *STEREO* catalogue. It has a visual magnitude of 9.5 and a spectral type of F8 (Wraight *et al.*, 2012). In addition to *STEREO*, this source was also observed by SW.

Table 4.5: Stellar properties of host star HD 23765 based on photometry

Parameters	Value
V magnitude	9.53
T_{eff}	5746 K
Spectral Type	F8
Period (P)	1.6865 ± 0.0004 d
Transit Depth	0.049±17 mag
Transit Epoch	2454213.264019 MJD
R_A	$0.98R_\odot$
R_B	$\geqslant 0.22R_\odot$
RA(epoch=2000)	03h 48 m 28.93 s
Dec(epoch=2000)	+ 21d 47m 50.85 s

Observations from both these surveys confirm the eclipse depth of this source to be $\sim$ 49 ± 17 mmag. Wraight *et al.* (2012) reported evidence of a slight tidal distortion in the host star. The radius of the secondary ($\sim$ $0.22R_\odot$) based on transit depth of 49 mmag occurring indicates that the primary star hosts a low mass companion. This motivated us to choose this star for PARAS RV observations. Table 4.5 lists the previously studied parameters for this source based on literature.

4.3.1 Spectroscopic and Photometric Observations of HD 23765

4.3.1.1 Spectroscopy

HD 23765 was followed up with PARAS in the months between October to November 2013.

Table 4.6: PARAS observation log for the star HD 23765

UT Date	T-2,400,000 (BJD-TDB)	Exp. Time (sec.)	RV (km s^{-1})	σ-RV (km s^{-1})
2013 Oct 22	56588.375	1200	19.178	0.212
2013 Oct 22	56588.391	1200	19.688	0.293
2013 Oct 23	56589.394	1200	−68.773	0.559
2013 Oct 23	56589.410	1200	−68.387	0.752
2013 Oct 24	56590.394	1200	−49.062	1.052
2013 Oct 24	56590.410	1200	−50.596	0.919
2013 Oct 25	56591.403	1200	−33.882	1.522
2013 Oct 26	56592.383	1200	−72.317	0.357
2013 Oct 26	56592.399	1200	−74.609	0.675
2013 Oct 27	56593.399	1200	20.061	0.932
2013 Oct 27	56593.415	1200	20.828	0.959
2013 Nov 12	56609.434	1200	−74.248	0.939
2013 Nov 14	56611.390	1200	−63.691	0.329
2013 Nov 19	56616.387	1200	−71.586	0.603

A set of 14 RV observations of this source were obtained. The spectra were taken in the simultaneous ThAr reference mode of PARAS at a resolving power of 67,000. The exposure times for each RV observation were kept at 1200 s resulting in SNR between 14 to 20 per pixel at the blaze wavelength. The observation log for the source is given in Table 4.6. The time in UT and BJD-TDB are mentioned in first two columns followed by exposure time and barycentric corrected RV in third and fourth column respectively. The next column has RV errors, the procedure for which is in § 4.2.2.2.

4.3.1.2 Photometry

HD 23765 was observed by both *STEREO* and *SuperWasp* missions.

***SuperWasp*:** SW photometry data were taken for this source between July 2004 to February 2007. A long periodic variability of over a year is speculated from the SW light curve by Wraight *et al.* (2012). We retrieved the available SW photometry data and found that based on observation times, the data were taken in three intervals, first interval in July 2004, second interval between September - December 2006 and the last interval between January - February 2007. The data from the first interval of 2004 have a vertical offset in the normalized flux values as compared to the remaining data. Since, the reason for offset was unknown, we could not correct for it in the dataset. Therefore, this interval of data was discarded for our work. The third interval, 2007, was also discarded because it had relatively large error bars of the order of $5-10\%$ in comparison to $1-2\%$ error bars for the second interval of dataset. The data finally considered was from the second interval, year 2006, which consisted of 75 % of the total data.

***STEREO*:** *STEREO* data were taken between the period $2007-2011$ for this star. *STEREO* observations do not show a similar variability as shown from SW data but there are hints of sinusoidal trend with a period of about seven times the orbital period (Wraight *et al.*, 2012). Moreover, *STEREO* photometry data for each year was fitted with a 4^{th} order polynomial as a part of their reduction procedure to remove instrumental effects which might have removed any signature of longer periodicity (Wraight *et al.*, 2011). This will require further ground-based observations spreaded over a few years to confirm or refute the claim.

4.3.2 Data Analysis of HD 23765

4.3.2.1 Radial Velocity Analysis

The data reduction and analysis techniques were applied by the standard pipeline, PARAS PIPELINE as discussed in Ch 2. The zero velocity mask for a F-type star was used to compute the cross-correlation function for HD 23765 similar to the star HD 213597 as discussed in § 4.2.2.1. The phase-folded RV points are plotted in blue filled circles in Fig 4.5.

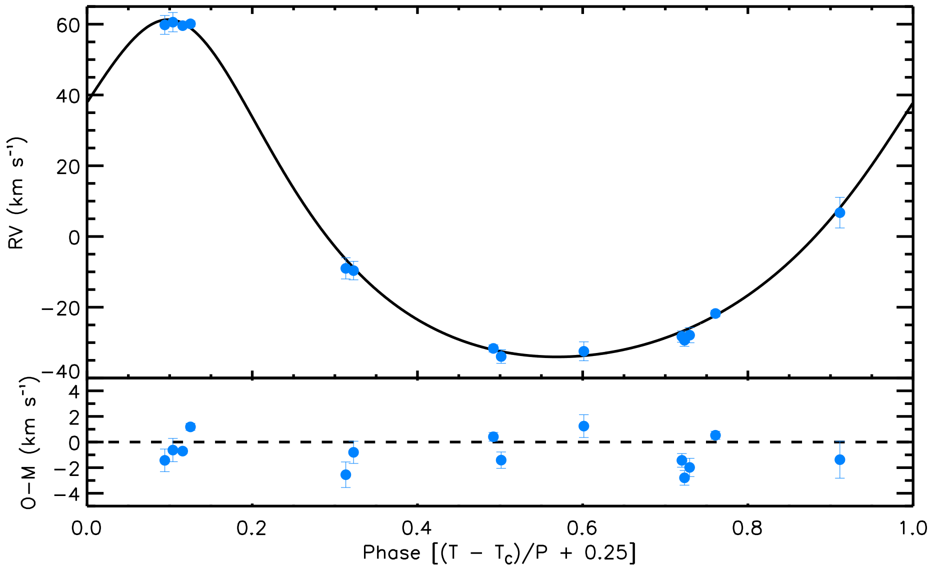

Figure 4.5: (Top panel) RV model curve for star HD 23765 obtained from EXOFAST is plotted against orbital phase. PARAS, Mount Abu (solid blue circles) observed data points along with the estimated errors are overplotted on the curve. (Bottom panel) The residuals from best-fitting are plotted below the RV plot. For better visual representation, the x axis (Phase) is shifted by 0.25 so that the central primary transit crossing point (T_c) occurs at phase 0.25 instead of 0.

More details on the model indicated by the solid line to be discussed in

§ 4.3.2.3.

4.3.2.2 Spectral analysis of HD 23765

PARAS SPEC was used to compute the stellar properties of the source (for details see Ch 3). All 14 observed epochs for the source HD 23765 were combined. The SNR/pixel for the 14 combined epochs was $\sim 75 - 80$ in the red region of the CCD and between $55 - 75$ in the blue region.

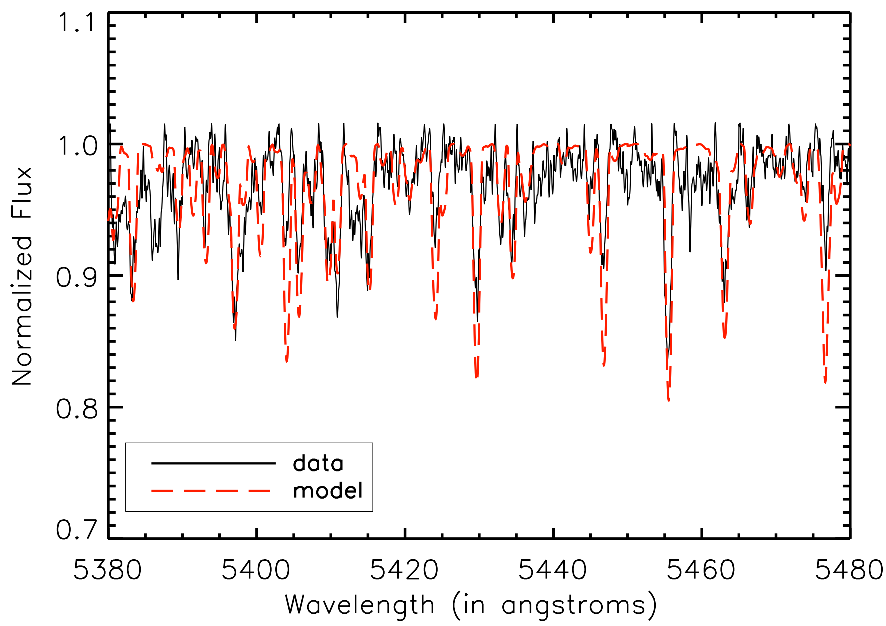

Figure 4.6: Observed normalized spectra (solid line) plotted across the wavelength region of $5380 - 5480$ $\mathring{A}$ for HD 23765. Overplotted is the modelled spectra (dash line) obtained from PARAS SPEC, with temperature value of $T_{\rm eff}$ of 6375 K, $[Fe/H]$ of -0.1 and log g of 4.1

SNR/pixel of $75 - 80$ is the lower limit at which synthetic spectral fitting method can be used. Since, HD 23765 is an F type star, there is more information in the blue region of the spectra. Thus, we smoothened the spectra to resolving power of ~ 44000 to improve the SNR/pixel in the blue region of the spectra. Thus, the wavelength region $5200 - 5700$ $\mathring{A}$ of the spectra was used for synthetic spectral fitting method. Since, the spectra have lower SNR/pixel, the stellar continuum is much noisier than the continuum of a synthetic model.

The continuum matching errors as discussed in Ch 3 causes relatively larger error bars of the order of ±100 K for $T_{\rm eff}$ and ±0.1 dex for $[Fe/H]$ and log g.

Table 4.7: Spectral lines used for EW method for HD 23765 in *PARAS SPEC*

Wavelength (Å)	Element	Wavelength (Å)	Element
4961.90	Fe I	5794.02	Fe I
5225.52	Fe I	5806.79	Fe I
5228.30	Fe I	5848.12	Fe I
5285.10	Fe I	6012.23	Fe I
5321.12	Fe I	6098.25	Fe I
5466.42	Fe I	6336.83	Fe I
5584.79	Fe I	6481.82	Fe I
5619.60	Fe I	6533.96	Fe I
5641.53	Fe I	6238.30	Fe II
5649.99	Fe I	6247.53	Fe II
5662.50	Fe I	6432.75	Fe II
5731.78	Fe I	6516.00	Fe II

The star has a magnitude of 9.5 and has a relatively large rotational velocity (32 km s^{-1}). The number of Fe I and Fe II lines identified for abundance determination through EW were limited, as most of the lines considered here were blended.The list of unblended spectral lines considered for analysis by the EW method are given in Table 4.7.

The iron abundance, $[Fe/H]$, was determined by synthetic spectral fitting method. Other physical parameters, $T_{\rm eff}$, log g and $v_{\rm micro}$ were determined by EW method. The results obtained from *PARAS SPEC* are summarized in Table 4.8. The rotational velocity was determined by the width of the CCF function and was kept fixed during analysis. The value on each parameter

Table 4.8: Spectral properties of HD 23765 as derived by *PARAS SPEC*

Parameters	Value	Error
T_{eff}	6375	± 100
$[Fe/H]$	-0.1	± 0.1
log g	4.1	± 0.15
v_{micro}	1.3	± 0.15
$v \sin i$	32 (fixed)	± 2

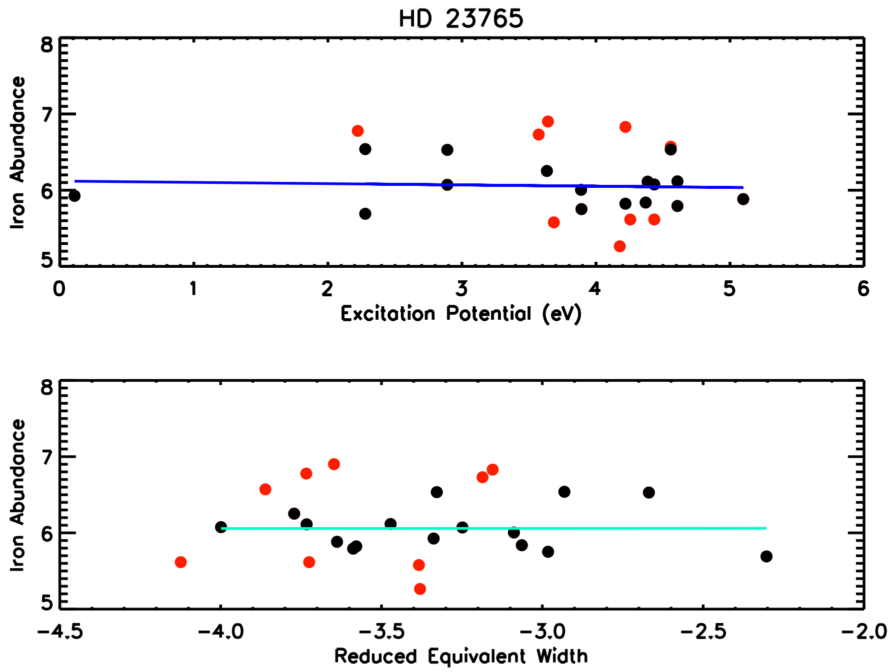

Figure 4.7: (Top panel) Iron abundance for HD 23765 is plotted against EP for each Fe I or Fe II line from the line list. The blue line is the least-square fit plotted for the minimum slope for the best-determined T_{eff}. (Bottom panel) Iron abundance is plotted against reduced EW and the blue-green line indicates the least-square fit for the minimum slope indicative of best-determined v_{micro}. The red points are the discarded points having standard deviation beyond 1 σ (not considered for the fit). The best-fit determined parameters are: T_{eff}=6375 K, $[Fe/H]$=-0.1, log g = 4.1, v_{micro}=1.3 km s^{-1}

along with the error bars are listed in the table. Fig. 4.6 shows a sample of the observed spectrum (solid line) overlaid by the best-fit model obtained from *PARAS SPEC* (dotted line) shown across a sample wavelength region 5380 – 5480 $\AA$. Fig. 4.7 shows two scatter plots. The top panel is a plot of iron abundances vs EP. The upper panel of the figure also shows a solid line in blue obtained by a least-square fit having a minimum slope of $0.020^{+0.01}_{-0.009}$ for iron abundances vs EP slope indicative of best-fit $T_{\rm eff}$ of 6375 K.

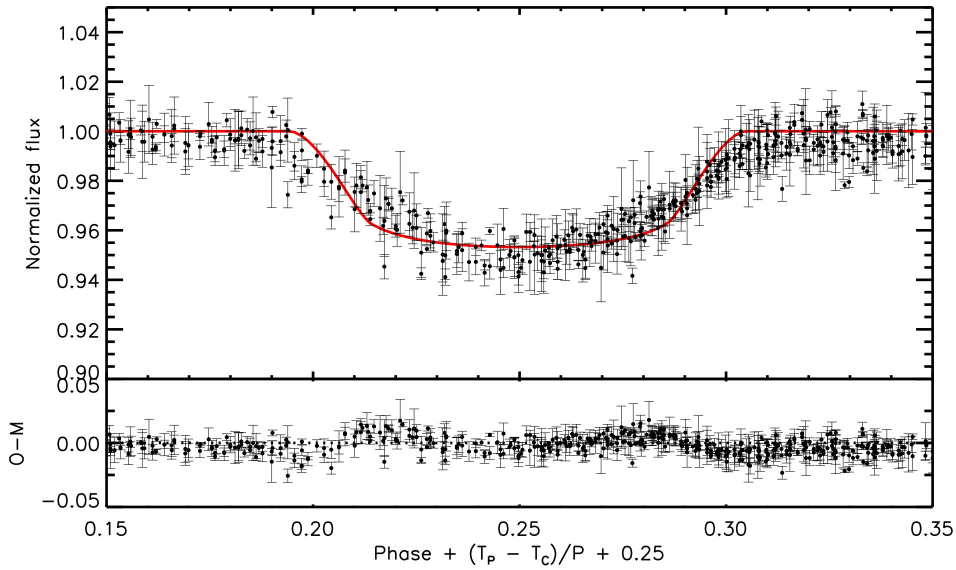

Figure 4.8: (Top panel) Transit curve for HD 23765 obtained from SW data is plotted based on the parameters from EXOFAST. (Bottom panel) Observed-Fit residuals are plotted. For better visual representation, the x axis (Phase) is shifted by 0.25 so that the central primary transit crossing point (T_c) occurs at phase 0.25 instead of 0.

In the bottom panel, a plot of iron abundance vs reduced EW is shown. A solid line in blue-green obtained by a least-square fit having a minimum slope of $0.012^{+0.008}_{-0.009}$ indicative of best-fit $v_{\rm micro}$ of 1.3 km s^{-1} is also shown in the bottom panel. Fe I-Fe II difference for HD 23765 is given as $0.003^{+0.007}_{-0.002}$ indicative of a log g value of 4.1

4.3.2.3 Orbital parameters derived for HD 23765

The fitting algorithm EXOFAST was run with the RV dataset from PARAS and SW photometry dataset belonging to the year 2006 (for details of EXOFAST refer § 4.2.2.5). The values for $T_{\rm eff} = 6375$ K; $[Fe/H] = -0.1$; $\log g = 4.1$ obtained by spectral analysis are used as priors on EXOFAST. The periodicity obtained is 1.6866 d which is close to the value quoted by the *STEREO* and SW catalogues. The RV semi-amplitude for the EB system is 47.6 km s^{-1} and the orbital separation is 0.034 AU. Fig. 4.5 illustrates the RV versus orbital phase for HD 23765. Solid blue circles (top panel) show RV measurements for HD 23765 taken with PARAS. The figure also shows the residuals (Observed-Model) in the bottom panel. The photometry data was fitted simultaneously with the RV data to determine the value of period, the depth and duration of the transit. Simultaneous fitting of photometry data yielded a transit depth of 0.039±0.001 mag and a transit duration of 266 ± 6 min. Fig. 4.8 (upper panel) shows the fit for the transit light curve obtained by analysing SW archival data overplotted with the model derived from EXOFAST (solid curve). The residuals are plotted in lower panel. The photometry data were noisy as seen in the plot. The parameters derived from this fit are given in Table 4.9.

4.3.3 Results obtained on HD 23765

With PARAS high-resolution spectroscopy observations and photometry transit data available from SW photometry, the second EB system HD 23765 has been studied. The primary of this system is an F6 type star and the secondary is inferred as an M3 type based on its mass (Pecaut and Mamajek, 2013). Based on the stellar parameter estimation through PARAS SPEC, the mass of the primary is derived as $1.507^{+0.086}_{-0.071}$ $M_\odot$ and radius as $2.29^{+0.12}_{-0.11}$ $R_\odot$. Based on the mass-radius relation, the values of mass and radius are 1.42 $M_\odot$ and 2.17 $R_\odot$ which are in close agreement to the values derived from our work. The mass of the secondary derived from the combined RV and photometry measurements is $0.393^{+0.014}_{-0.013}$ $M_\odot$ and the radius is 0.449 ± 0.025 $R_\odot$. The for-

Table 4.9: Results obtained from EXOFAST by fitting of RV and transit data for HD 23765 with a 68% confidence interval.

Parameter	Value
HD 23765A:	
M_A ($M_\odot$)	$1.507^{+0.086}_{-0.071}$
R_A ($R_\odot$)	$2.29^{+0.12}_{-0.11}$
L_A ($L_\odot$)	$7.87^{+1.1}_{-0.82}$
ρ_A (cgs)	$0.177^{+0.14}_{-0.13}$
log g_A (cgs)	$3.90^{+0.088}_{-0.087}$
$T_{\rm eff}$ (K)	6392^{+98}_{-100}
[Fe/H]	-0.063 ± 0.10
HD 23765B:	
e	$0.290^{+0.087}_{-0.096}$
ω_* (degrees)	$9.1^{+2.2}_{-2.3}$
P	1.68668 ± 0.00039
a	$0.03433^{+0.00064}_{-0.00056}$
M_B ($M_\odot$)	$0.393^{+0.014}_{-0.013}$
R_B ($R_\odot$)	0.449 ± 0.025
RV Parameters:	
$e \cos \omega_*$	0.286 ± 0.022
$e \sin \omega_*$	$0.046^{+0.027}_{-0.026}$
T_P	$2456593.436^{+0.026}_{-0.027}$
K (m/s)	47590^{+690}_{-570}
M_B/M_A	$0.2604^{+0.0079}_{-0.0072}$
γ m s^{-1}	-41490^{+940}_{-910}
Transit Parameters:	
T_C (BJD)	$2456593.6688^{+0.0093}_{-0.0094}$
R_B/R_A	$0.202^{+0.029}_{-0.019}$
i (degrees)	$87.2^{+2.0}_{-2.9}$
a/R_A	$3.226^{+0.094}_{-0.096}$
δ	0.039 ± 0.001
T_{14} (minutes)	266 ± 6

mal errors on the measurements for secondary mass and radius are $\sim 7-8\%$. *PARAS SPEC* routine applied on this star gives us $T_{\rm eff}$ = 6375 $\pm$ 100 K, $[Fe/H] = -0.1 \pm 0.1$ for $\log g = 4.1 \pm 0.15$. As derived from photometry, the system has an inclination angle of $87.2^{\circ}{}^{+2.0}_{-2.9}$, transit depth of 0.039 ± 0.001 mag and transit duration of 266 $\pm$ 6 min. This system is a short period EB having a period of 1.6866 d similar to the first EB studied, namely, HD 213597, which has a periodicity of 2.4238 d. Despite its short orbital period, the system has a considerable eccentricity of $\sim$ 0.3 as against the EB HD 213597 which has an eccentricity of $\sim$ 0.02. The mass for HD 23765B ($\sim$ 0.4 $M_{\odot}$) lies on the boundary for transition between completely convective and partially radiative interiors for stars and thus serves a crucial EB system for mass and radius measurements at high accuracies.

4.4 Detection of a mid-M dwarf, SAO 106989B, from SW photometry

The third and last EB candidate described in this Chapter, SAO 106989, is shortlisted from ground-based SW photometry catalogue (Street *et al.*, 2007). This EB candidate has a reported periodicity of 4.4 d and a transit depth of 13.5 mmag. SW photometry has listed many exoplanet host and EB candidates in short periods between $2-3$ days (Street *et al.*, 2007). Thus, a periodicity of 4.4 d is relatively long in SW sampling standards and thereby limited number of transits are monitored for this star. Based on the radius estimation, the secondary could be a hot Jupiter or a M dwarf companion (both the objects have comparable sizes).

The archival transit photometry data for this source has not been made public. Thus, we could not independently fit the data to verify SW transit results on this source. Ground-based observations will be desirable in future to assess the radius of the components and inclination for the system at high accuracies. The primary star, SAO 106989, is a late F type star, giving us another opportunity to study F+M EB systems. The stellar parameters are

Table 4.10: Data on SAO 106989 by SW photometry as discussed in (Street *et al.*, 2007)

Parameters	Value
V magnitude	9.3
Spectral Type	F8
Period (P)	4.400381 d
Transit Depth	0.0135 mag
Transit Duration (t)	2.424 h
R_A	$1.24R_\odot$
R_B	$1.23R_J$
RA(epoch=2000)	$21h$ 16 m 45.22 s
Dec(epoch=2000)	+ 19d 21m 36.79 s

listed in Table 4.10 (Street *et al.*, 2007).

4.4.1 RV observations of SAO 106989 with PARAS

SAO 106989 was followed up with PARAS in the months between October to November 2013. A set of 17 RV observations of this source were obtained. The spectra were taken in the simultaneous reference mode with ThAr lamp as the calibration source at a resolving power of 67,000. The exposure times for each RV observation was kept at 1200 s resulting in SNR between 12 to 20 per pixel at the blaze wavelength. The observation nights used for data collection were spectroscopic in nature. The observation log for the source is given in Table 4.11. The time in UT and BJD-TDB are mentioned in first two columns followed by exposure time and barycentric corrected RV in third and fourth column respectively. The next column has RV errors computed in a way similar for the other two sources.

4.4.2 Data Analysis for SAO 106989

4.4.2.1 RV analysis of SAO 106989

PARAS pipeline, as discussed in Ch 2, was used for the data reduction and analysis procedure. The reduction followed the same procedure as for the previous sources.

Table 4.11: Observations for the star SAO 106989.

UT Date	T-2,400,000 (BJD-TDB)	Exp. Time (sec.)	RV (km s^{-1})	σ-RV (km s^{-1})
2013 Oct 22	56588.193	1200	−26.373	0.116
2013 Oct 22	56588.209	1200	−26.566	0.086
2013 Oct 22	56588.226	1200	−26.517	0.099
2013 Oct 23	56589.180	1200	−16.733	0.107
2013 Oct 23	56589.196	1200	−15.638	0.151
2013 Oct 24	56590.176	1200	8.325	0.202
2013 Oct 24	56590.193	1200	9.055	0.318
2013 Oct 24	56590.212	1200	9.361	0.215
2013 Oct 25	56591.203	1200	27.662	0.102
2013 Oct 25	56591.219	1200	27.856	0.113
2013 Oct 25	56591.234	1200	27.813	0.160
2013 Oct 26	56592.188	1200	−19.679	0.098
2013 Oct 26	56592.203	1200	−20.613	0.133
2013 Oct 26	56592.219	1200	−20.016	0.214
2013 Oct 27	56593.219	1200	−21.047	0.191
2013 Oct 27	56593.235	1200	−22.113	0.192
2013 Nov 19	56616.132	1200	−2.911	0.052

Since SAO 106989 is a F9 type star (Pecaut and Mamajek, 2013), the zero velocity mask of G2 type star was used for cross correlation to compute RV measurements. The difference in temperature for the mask and SAO 106989

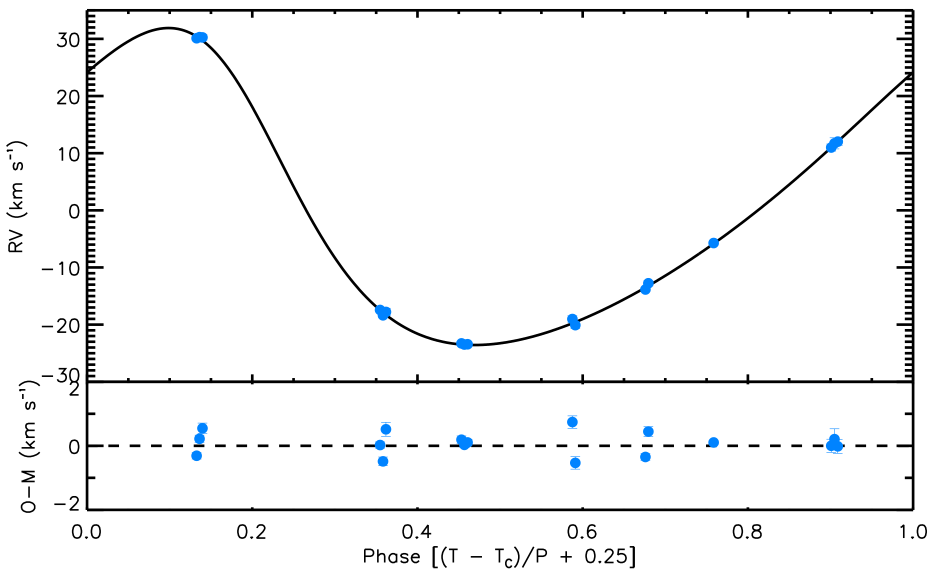

Figure 4.9: (Top panel) RV model curve for star SAO 106989 obtained from EXOFAST is plotted against orbital phase. PARAS, Mount Abu (solid blue circles) observed data points along with the estimated errors are overplotted on the curve. (Bottom panel) The residuals from best-fitting are plotted below the RV plot. For better visual representation, the x axis in Phase is shifted by 0.25 so that the central primary transit crossing point (T_c) occurs at phase 0.25 instead of 0.

is $\sim$ 250 K and thus it is the most suitable choice for the stellar mask. The barycentric-corrected phase-folded RV points are shown in Fig. 4.9 with filled blue circles. The solid line is the model, details of which are discussed in § 4.4.2.3.

4.4.2.2 ***PARAS SPEC*** analysis of SAO 106989

PARAS SPEC was used to compute the stellar properties for this source. We follow both the synthetic spectral fitting and EW methods for determination of stellar atmospheric properties. Similar to the previous target, SAO 106989 is a F type star. Thus, due to low SNR, we followed the same procedure as followed for the case of HD 23765 and concentrated on the wavelength region between 5200 – 5700 $\mathring{A}$. The results obtained are summarized in Table 4.12. The rotational velocity is obtained from the width of CCF and is kept fixed during the analysis of *PARAS SPEC*.

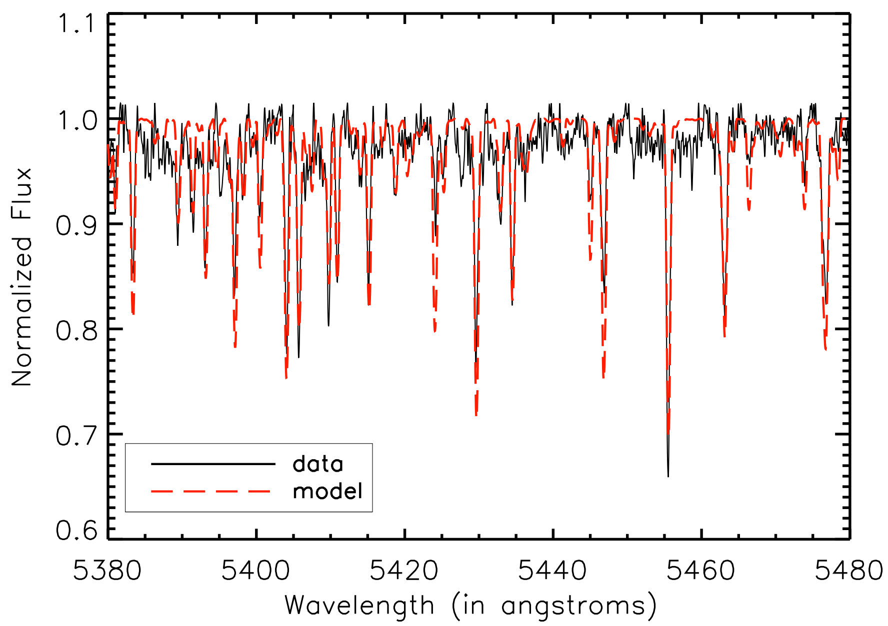

Figure 4.10: Observed normalized spectra (solid line) plotted across the wavelength region of 5380 – 5480 Å. Overplotted is the modelled spectra (dash line) obtained from PARAS SPEC, with temperature value of $T_{\rm eff}$ of 5975 K, $[Fe/H]$ of 0.0 and log g of 4.3

Fig. 4.10 shows a sample of the observed spectrum (solid line) overlaid by the best-fit model ($T_{\rm eff}$ = 5925 K; $[Fe/H]$ = −0.2; log g = 4.25; dotted line). The observed sample and model spectra are shown across the wavelength region 5380 – 5480 Å.

The list of unblended spectral lines considered for analysis by the EW method are given in Table 4.13. In Fig. 4.11, a least-square fit line having a minimum slope for iron abundances vs. EP obtained for best-fit $T_{\rm eff}$ for SAO 106989 is shown in the upper panel. In the bottom panel, a plot of iron abundance vs reduced EW is shown with a least-square fit line having a minimum slope for the best-fit $v_{\rm micro}$.

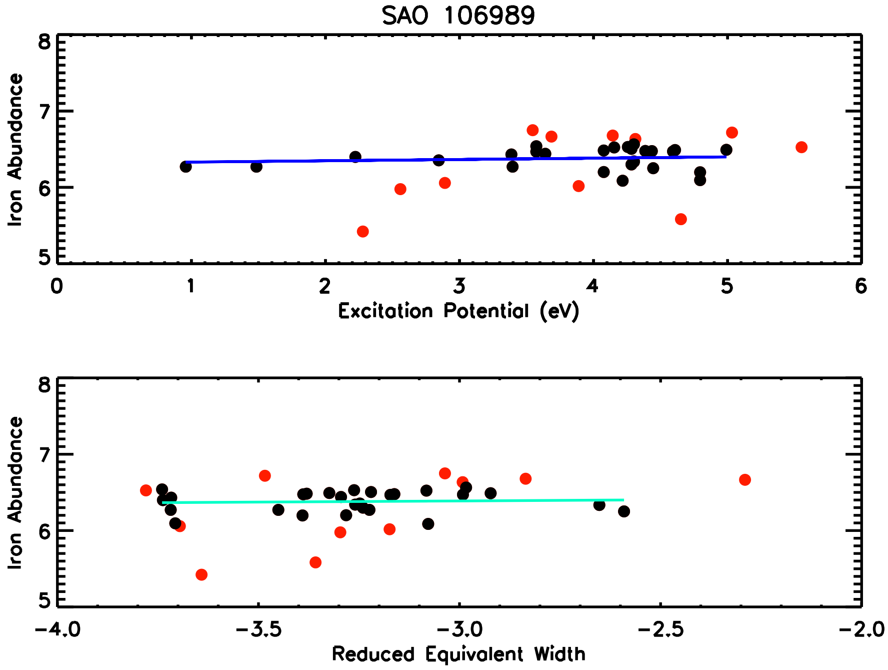

Figure 4.11: (Top panel) Iron abundance for SAO 106989 is plotted against EP for each Fe I or Fe II line from the line list. The blue line is the least-square fit to each data point seen in the scatter plot indicating the minimum slope for the best-determined $T_{\rm eff}$. (Bottom panel) Iron abundance is plotted against reduced EW and the blue-green line indicates the minimum slope for the least-square fit obtained on the data for best determined $v_{\rm micro}$. The red points are the discarded points having standard deviation beyond 1 σ (not considered for the fit). The best-fit determined parameters are: $T_{\rm eff}$ = 5925 K, $[Fe/H] = -0.2$, log $g = 4.25$, $v_{\rm micro} = 0.65$ km s^{-1}

Table 4.12: Spectral properties of SAO 106989 as derived by *PARAS SPEC*

Parameters	Value	Error
$T_{\rm eff}$	5925	±100
$[Fe/H]$	-0.2	±0.1
log g	4.25	±0.1
v$_{\rm micro}$	0.65	±0.15
$v \sin i$	20 (fixed)	±1

Table 4.13: Spectral lines used for EW method for SAO 106989 in *PARAS SPEC*

Wavelength (Å)	Element	Wavelength (Å)	Element
4869.39	Fe I	5741.86	Fe I
4892.88	Fe I	5784.71	Fe I
5012.64	Fe I	5806.78	Fe I
5023.16	Fe I	5853.07	Fe I
5088.27	Fe I	5902.47	Fe I
5109.61	Fe I	5905.73	Fe I
5197.77	Fe I	6012.42	Fe I
5285.03	Fe I	6229.24	Fe I
5326.18	Fe I	6315.90	Fe I
5398.34	Fe I	6336.80	Fe I
5441.42	Fe I	6338.99	Fe I
5494.35	Fe I	6364.50	Fe I
5576.98	Fe I	6481.92	Fe I
5584.88	Fe I	6498.95	Fe I
5587.54	Fe I	6609.14	Fe I
5619.63	Fe I	5256.92	Fe II
5636.54	Fe I	5627.50	Fe II
5691.45	Fe I	6238.34	Fe II
5732.22	Fe I	6383.78	Fe II

4.4.2.3 Orbital parameters derived for SAO 106989

Since transit data was unavailable, EXOFAST routine was executed with the RV dataset only. The results of the execution are summarized in Table 4.14.

Table 4.14: Results obtained from EXOFAST by simultaneous fitting of RV and transit data for SAO 106989 with a 68% confidence interval.

Parameter	Units	Values
SAO 106989A:		
M_A	Mass ($M_\odot$)	$1.099^{+0.055}_{-0.049}$
R_A	Radius ($R_\odot$)	$1.29^{+0.17}_{-0.15}$
L_A	Luminosity ($L_\odot$)	$1.86^{+0.57}_{-0.43}$
ρ_A	Density (cgs)	$0.72^{+0.36}_{-0.25}$
$\log g_A$	Surface gravity (cgs)	$4.25^{+0.10}_{-0.097}$
$T_{\rm eff}$	Effective temperature (K)	5929^{+110}_{-100}
[Fe/H]	Iron Abundance	-0.2 ± 0.1
SAO 106989B:		
e	Eccentricity	$0.254^{+0.01}_{-0.009}$
ω_*	Argument of periastron (degrees)	53 ± 5
P	Period (days)	$4.426^{+0.026}_{-0.023}$
a	Semi-major axis (AU)	$0.0545^{+0.0009}_{-0.0008}$
$M_B \sin i$	Projected Mass ($M_\odot$)	$0.254^{+0.008}_{-0.007}$
RV Parameters:		
$e \cos \omega_*$		$0.151^{+0.024}_{-0.022}$
$e \sin \omega_*$		$0.204^{+0.01}_{-0.009}$
T_P	Time of periastron (BJD)	2456595.883 ± 0.071
K	RV semi-amplitude m s^{-1}	27770^{+240}_{-200}
M_B/M_A	Mass ratio	$0.2305^{+0.0043}_{-0.0045}$
γ	Systemic RV m s^{-1}	-400 ± 1400

The EB periodicity of 4.426 d obtained from the analysis is close to the value obtained from SW photometry. The RV semi-amplitude for the EB system is 27780^{+240}_{-200} m s^{-1} with an eccentricity of $0.255^{+0.01}_{-0.009}$ at an orbital separation of $0.0545^{+0.0009}_{-0.0008}$ AU. Fig. 4.9 illustrates the RV versus orbital phase for SAO 106989A. Solid blue circles (top panel) show RV measurements of the star taken with PARAS. The figure also shows the residuals (Observed-Model) in the bottom panel.

4.4.3 Results obtained for SAO 106989

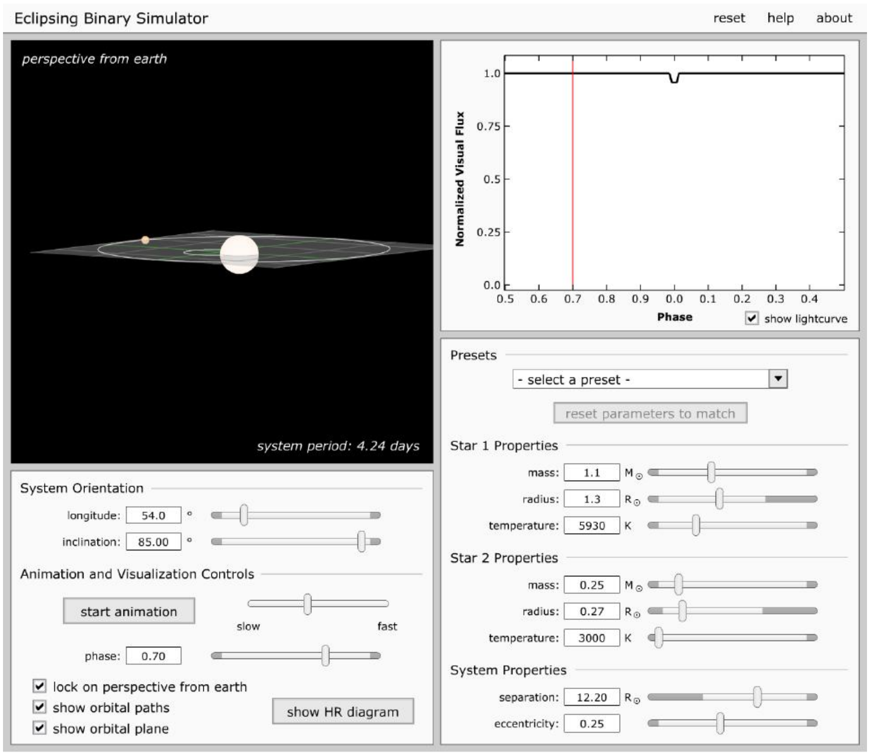

Figure 4.12: Screenshot of the Eclipsing Binary Simulator (Left panel) Orbital path of the two stars in the EB (Right panel) Light curve of the system as seen from Earth. (Bottom panel) Inputs on the masses, radii of the two components, P, a, and ω of the orbit given to the EB simulator. (Credit: The University of Nebraska-Lincoln astronomy education group)

PARAS SPEC routine applied on this star gives T_{eff} = 5925 $\pm$ 100 K, $[Fe/H]$ = -0.2 $\pm$ 0.1 for log g = 4.25 $\pm$ 0.1. The mass and radius for the primary of the EB system, SAO 106989, based on the spectroscopic analysis and Torres relation (Torres, Andersen and Giménez, 2010) are $1.099^{+0.055}_{-0.049}$ $M_\odot$

and $1.29^{+0.17}_{-0.15}$ R$_\odot$ respectively. The projected mass of the secondary derived here is $0.254^{+0.008}_{-0.007}$ M$_\odot$ determined at an accuracy of $\sim$ 3− 4 per cent (formal errors). Though, the photometry data are unavailable to derive the angle of inclination, i, for the orbit, we did simulations with the eclipsing binary simulator (http://astro.unl.edu/naap/ebs/animations/ebs.html) and it was estimated that for eclipses to be visible for an EB with the derived orbital parameters, i should be atleast 82°. A screenshot of the EB simulator attached in Fig 4.12. The left panel indicates the orbital path and plane whereas the right panel indicates the light curve for the EB system. The input parameters supplied to the simulator were the results obtained from Table 4.14. In such a case, an upper limit of $M_B = 0.256$ M$_\odot$ for the secondary can be assigned. Both these values are within error bars of each other. Thus, unavailability of i value does not affect the secondary mass estimation. However, the radius measurement was not possible. The radius value predicted for SAO 106989B from SW photometry is $R_B = 0.126 R_\odot$. This is much lower than theoretically expected radius value derived for a star having a mass of $M_B = 0.256$ M$_\odot$. SW photometry data have accuracies of $\sim 6 - 7$ mmag (Street *et al.*, 2007). Thus, a transit depth of 13.5 mmag is recorded with 2 σ accuracy. We suspect poor data quality which could lead to incorrect transit depth measurement and thereby incorrect radius estimation. Since, we do not have access to SW data, we will have to observe this source independently to cross-check the radius value.

4.5 Discussion and Conclusions

Based on the study of three F+M EBs presented here, some common inferences are presented here as follows:

4.5.1 M-R relationship

We matched our observationally derived radii estimations on the three EB systems (VLMS components) with Baraffes's models. The models used at the initial stages of the research work were the models released in the year 1998. However, with the availability of new improved models (Baraffe *et al.*, 2015), we used these new models to check our estimations. The recent models have updated molecular linelists and revised solar abundances. The line opacities for several important molecules have been updated. These models have been able to account for some of the flaws such as predicting optical colours of the stars that are too blue (Baraffe *et al.*, 2015). However, M-R relations for solar metallicity stars for the age $\sim$ 1 Gyr do not have any changes for VLMS objects (below 0.6 $M_{\odot}$), similar to the ones studied by us. It is important to note that the computations have been made for solar metallicity case only unlike the previous models (Baraffe *et al.*, 1998) where the comparison could also be made for $[M/H] = -0.5$. Thus, the comparisons of the observations made here with both the models (Baraffe *et al.* (1998) and Baraffe *et al.* (2015)) yield similar results. A detailed discussion on the M-R relationship is presented below.

Metallicity and the iron abundance of the EB system, **HD 213597**, are accurately determined in this work as -0.105 ± 0.03 and -0.025 ± 0.05 respectively (see Table 4.3) by spectroscopic analysis. From the models for M dwarfs (Baraffe *et al.*, 1998), the $T_{\rm eff}$ of the secondary star, for a mass of $\sim$ 0.3 $M_{\odot}$ (from this work) and an age of $\sim$ 2 Gyr (Casagrande *et al.*, 2011), is estimated as 3437 K for a $[M/H]$ of 0.0, and 3643 K for a $[M/H]$ of -0.5. From Baraffe *et al.* (1998) models, the radius for a star of mass 0.3 $M_{\odot}$ turns out to be 0.29 $R_{\odot}$ for $[M/H] = 0.0$ and 0.28 $R_{\odot}$ for $[M/H] = -0.5$. Clearly, these theoretically derived radius values are lower than the observations presented here. Similar results are obtained when verified with the latest models (Baraffe *et al.*, 2015).

Meibom *et al.* (2015) have predicted the age of Sun like stars in solar neighbourhood based on their rotational periods. In order to get a handle on the age of the system, the rotational period of the star must be determined. We estimate the age of EB **HD 23765** to be between 0.7−−1 Gyr based on its rotational velocity of 32 km s^{-1} (Meibom *et al.*, 2015). Thus, from the Baraffe *et al.* (2015) models, for HD 23765B, the radius of 0.392 $M_{\odot}$ star to be around 0.37 $R_{\odot}$. The radius of the secondary derived from photometry measurements is 0.449 ± 0.025. A conclusion can be thus drawn that the observed value is higher than the theoretically predicted radius from Baraffe models. The discrepancy seen between the observational and theoretical radius values is evident in the regime of early type M dwarfs.

Extending this comparison to the third system, we find that **SAO 106989** has a mass of $0.254^{+0.008}_{-0.007}$ M$_{\odot}$. From Baraffe *et al.* (2015) models, the radius for 0.25 $M_{\odot}$ turns out to be 0.26 $R_{\odot}$ for [M/H] = 0.0. The value given by SW photometry is $R_B = 0.126 R_{\odot}$. This value is less than half of the expected value. This result is in sharp contrast to the discrepancies observed so far in modelling of EBs. Thus, this system requires accurate photometric monitoring to shed more light on the contrasting result that the observationally derived value of radius is much smaller than the theoretical one.

It has been the prime objective of the thesis to look at EBs having masses between 0.08 − 0.4 M$_{\odot}$ as this mass regime has been poorly studied. Thereby, we decided to look into all the previously studied sources in literature between the mass range of 0.08 − 0.4 M$_{\odot}$ which have masses and radii measured at accuracies better than or at best equal to 10%. Table 4.15 is a non-exhaustive compilation of the stars having masses and radii determined at accuracies better than 10%. The first three columns contain the name of the object, its mass and radius. The systems are SB1 or SB2 by nature. The classification of the EB, based on spectral types, is mentioned in the penultimate column. The literature references in which the sources are studied are cited in the last column of the table.

In order to compare our work with the previous work, a theoretical M-R diagram is plotted in Fig. 4.13 for the M dwarfs having masses between 0.08−0.4 M$_{\odot}$ based on Baraffe models (Baraffe *et al.*, 2015) for 1 Gyr isochrone and solar metallicity (most of the objects studied here have this age and metallicity). We have overplotted objects studied in literature from Table 4.15 with their respective error bars on masses and radii on the theoretical M-R diagram.

Table 4.15: A compilation of known VLMS other than our work for masses and radii measured at accuracies better than or at best equal to 10%.

Object	Mass	Radius	EB System	References
J1219-39B	0.091 ± 0.002	$0.1174^{+0.0071}_{-0.0050}$	**K+M**	(1)
HAT-TR-205	0.124 ± 0.01	0.167 ± 0.006	F+M	(2)
KIC 1571511B	$0.14136^{+0.0051}_{-0.0042}$	$0.17831^{+0.0013}_{-0.0016}$	F+M	(3)
WTS19g4-020B	0.143 ± 0.006	0.174 ± 0.006	M+M	(4)
J0113+31B	0.186 ± 0.010	0.209 ± 0.011	**G+M**	(5)
T-Lyr1-01622B	0.198 ± 0.012	0.238 ± 0.007	M+M	(6)
KEPLER16B	$0.20255^{+0.00066}_{-0.00065}$	$0.22623^{0.00059}_{-0.00053}$	**K+M**	(7)
KOI-126C	0.2127 ± 0.0026	0.2318 ± 0.0013	M+M	(8)
CM Dra A	0.2130 ± 0.0009	0.2534 ± 0.0019	M+M	(9)
CM Dra B	0.2141 ± 0.0010	0.2396 ± 0.0015	M+M	(9)
T-Lyr0-08070B	0.240 ± 0.019	0.265 ± 0.010	M+M	(6)
KOI-126B	0.2413 ± 0.003	0.2543 ± 0.0014	M+M	(8)
OGLE-TR-78B	0.243 ± 0.015	0.240 ± 0.013	F+M	(10)
1RXSJ154727A	0.2576 ± 0.0085	0.2895 ± 0.0068	M+M	(11)
1RXSJ154727B	0.2585 ± 0.0080	0.2895 ± 0.0068	M+M	(11)
LSPMJ1112B	0.2745 ± 0.0012	0.2978 ± 0.005	M+M	(12)
GJ3236B	0.281 ± 0.015	0.3 ± 0.015	M+M	(13)
LP133-373A	0.34 ± 0.02	0.330 ± 0.014	M+M	(14)
LP133-373B	0.34 ± 0.02	0.330 ± 0.014	M+M	(14)
19e-3-08413B	0.351 ± 0.019	0.375 ± 0.020	M+M	(15)
OGLE-TR-6B	0.359 ± 0.025	0.393 ± 0.018	F+M	(16)
GJ3236A	0.376 ± 0.016	0.3795 ± 0.0084	M+M	(13)
19c-3-01405B	0.376 ± 0.024	0.393 ± 0.019	M+M	(15)
MG1-2056316B	0.382 ± 0.001	0.374 ± 0.002	M+M	(17)
LSPMJ1112A	0.3946 ± 0.0023	0.3860 ± 0.005	M+M	(12)
CuCnCB	0.3980 ± 0.0014	0.3908 ± 0.0094	M+M	(18)

References: (1) Triaud *et al.* (2013); (2) Beatty *et al.* (2007); (3) Ofir *et al.* (2012); (4) Nefs *et al.* (2013); (5) Gómez Maqueo Chew *et al.* (2014); (6)Fernandez *et al.* (2009); (7) Doyle *et al.* (2011); (8) Carter *et al.* (2011); (9) Morales *et al.* (2009); (10) Pont *et al.* (2005b); (11) Hartman *et al.* (2011); (12) Irwin *et al.* (2011); (13) Irwin *et al.* (2009); (14) Vaccaro *et al.* (2007); (15) Birkby *et al.* (2012); (16) Bouchy *et al.* (2005); (17) Kraus *et al.* (2011); (18) Ribas (2003)

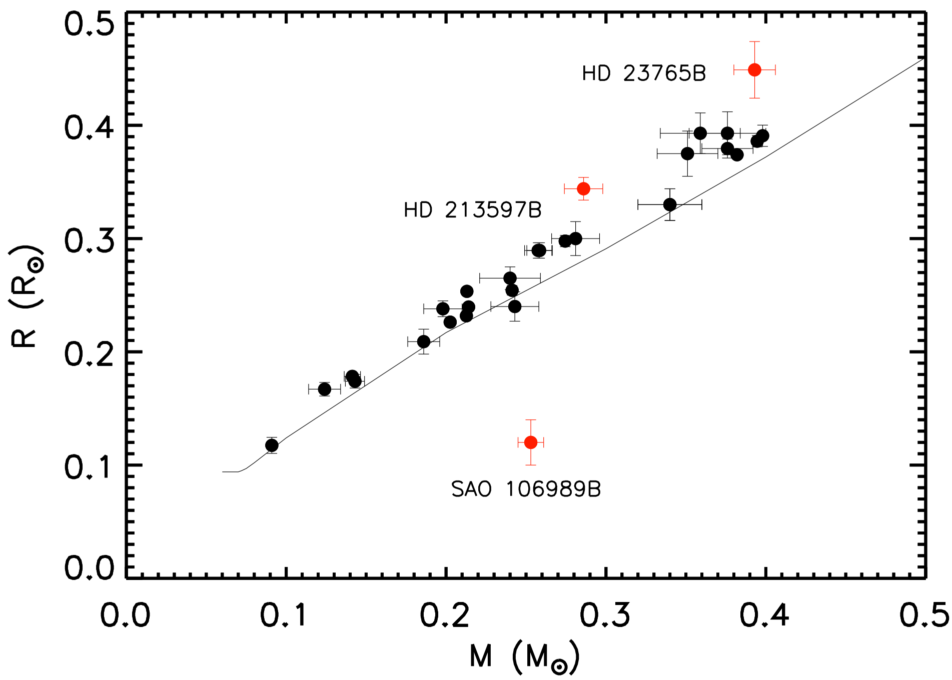

Figure 4.13: Mass-Radius diagram for M dwarfs based on Barffe models for 1 Gyr isochrone and solar metallicity. Overplotted are the previously studied M dwarfs listed in Table 4.15 with black filled circles with their reported uncertainties. The three M dwarfs discovered by PARAS in F+M EBs are also overplotted in red filled circles with their respective error bars. HD 23765B and HD 213597B have both masses and radii determined from this work whereas for SAO 106989B, the projected mass is derived from this work and the radius is based on measurement from SW photometry. Fresh photometry observations for SAO 106989B are desirable in future.

Objects studied as a part of this thesis are also overplotted with their respective error bars on masses and radii in red on the theoretical M-R diagram. The current research work has contributed three objects to the existing 26 samples previously studied in literature at accuracies better than 10 %. Out of which, two sources, namely, HD 213597B and HD 23765B, have masses and radii measured by us and for one of the sources, SAO 106989B, we do not have radius measurement verified and the reported measurements are quoted from the photometry transit (Street *et al.*, 2007). This source needs to be followed up for transit measurements in future.

As seen from Fig. 4.13, many of the stars studied in literature fall above the theoretical M-R plot clearly indicative of the M dwarf radius problem. Similarly as seen from the sources studied in our work, stars HD 213597B and HD 23765B, clearly fall above the M-R relation curve. The masses of these two objects are close to the boundary of the transition between convective and radiative core ($0.3 - 0.4$ $M_{\odot}$). Such objects are commonly known to report inconsistencies in radius measurements between theoretical models and observations ((Torres, Andersen and Giménez, 2010) and references therein) as shown by the samples overplotted.

4.5.2 Tidal interaction

The binary system, **HD 213597**, has an inclination angle of $84^{\circ}.9^{+0.61}_{-0.5}$. The rotational velocity of the primary star obtained by SME analysis, as mentioned in Table 4.3, is 40 km s^{-1}, which matches when measured by the width of the cross-correlation function. This value is comparatively lower than the reported rotational velocities for similar F-type stars (Głębocki and Gnaciński, 2005). With the knowledge of rotational velocity of the primary star and its radius of $\sim$ 2.03 $R_{\odot}$ from Table 4.1, the projected spin period, P/sin i of the primary star is calculated to be 2.422 d, which is close to the observed orbital period of the system. The eccentricity of the system, calculated as 0.0198, makes it close to circular. Since the orbital and rotational periods for the star are synchronous, this star forms another evidence for tidal circularization playing role in a close binary system (Mazeh, 2008).

Based on the work by Zahn (1977), it is estimated that for **HD 23765** the orbital synchronization and circularization timescales are $\sim$ 0.03 Myr and 27 Myr respectively. These are much smaller than the age of the system ($0.7 - 1$ Gyr). Thus, it is expected that both the stars should be tidally locked to each other and the orbits be circularized. However, this is not the case as seen by the eccentricity of ~ 0.3 for the system. The large eccentricity may also indicate the presence of a tertiary body. Moreover, slight indications of long periodicity of 1 yr in the SW photometry data needs to be carefully examined by high precision ground-based follow-up photometry. The rotational velocity for the star based on the CCF width from RV measurements is 32 km s^{-1}. Hence the projected rotational period of the late F type star is 3.16 d. This is more than the orbital period of 1.69 d for the system (Zahn, 1977). It can be expected that the orbit should be evolving for such a system. Thus, there is a possibility that the star has spun-up and may continue to avoid the fall of the M dwarf onto the primary (Bouchy *et al.*, 2011a). It will be imperative to study the orbital evolution of this system in future.

The system, **SAO 106989**, like the previously studied case of HD 23765, has a large eccentricity (e $\sim$ 0.25) despite its short orbital period. The rotational velocity of the star is $\sim$ 20 km s^{-1} based on the CCF width from RV computation. Based on its orbital period, the orbital velocity is also $\sim$ 20 km s^{-1}. From Zahn (1977), we estimate the synchronization time scale for this star to be $\sim$ 30 Myr. Since, the age of the star is more than this, we rightly see the orbital and rotational velocity for the star synchronized with each other. Synchronization of orbital and rotational velocity of the star is another indication of stable evolution of the orbit for the star. In contrast, the circularization period for the star is 5.6 Gyr, which is always larger than the synchronization time scales. It might be a possibility that the orbit of the star might circularize over time based on the tidal force exerted by its F type companion (Zahn, 1977; Hut, 1981). Studying long term evolution of this system will also be crucial.

Future spectroscopic and detailed photometry observations for both these stars during transit may enable us to observe the Rossiter-McLaughlin (RM) effect (Gaudi and Winn, 2007), and help determine whether the secondary star is in retrograde or prograde orbital motion with respect to the rotation of the primary. This may lead to a better understanding of the binary formation mechanisms at a primordial stage. M dwarfs peak more in the near infra-red and we expect the spectra of the secondary to be seen with a larger telescope, the case of SB2 systems. Since the companions are M dwarfs, future near-infrared observations with better sensitivity (larger telescope) will be able to provide dynamical masses of the systems.

Chapter 5

A Rare Discovery of a star with mass less than 0.1 $M_\odot$ in an Eclipsing Binary system

5.1 Introduction

It has been mentioned in the preceding Chapters that M dwarfs that have masses more than 0.3 $M_\odot$ show significant discrepancies between observed and theoretically derived radius estimates. However, objects which have masses less than 0.3 $M_\odot$ seem to agree with the Baraffe models (Baraffe *et al.*, 2015) in a better way. The interiors of such stars are completely convective (López-Morales, 2007). If one chooses to concentrate on very low mass stars (VLMS) with masses $\leqslant 0.1$ $M_\odot$, there is a dearth of such samples discovered with accuracies $\leqslant 5 - 6\%$. There have been only a handful of EB systems studied at such high accuracies in which one of the components is VLMS object with mass ≤ 0.1 $M_\odot$ (Wisniewski *et al.*, 2012; Triaud *et al.*, 2013; Gómez Maqueo Chew *et al.*, 2014; Ofir *et al.*, 2012; Tal-Or *et al.*, 2013; Beatty *et al.*, 2007) where masses of the objects have been determined at high accuracies. Thus, we decided to focus on candidates which were reported to have the companion radius ~ 1 R$_J$ since VLMS objects $\leqslant 0.1\ M_\odot$ will have radii of that order. One such candidate, J234318.41+295556.5A, (J2343+29) is identified from *Super-Wasp* (SW) photometry by Christian *et al.* (2006) and Collier Cameron *et al.* (2007). The observations, analysis and results for the candidate J2343+29 discovered by SW photometry catalogue are presented here. This Chapter will describe the details of observations, analysis and results on this source in the following sections.

Table 5.1: Data on J2343+29 by SW photometry as discussed in Collier Cameron *et al.* (2007)

Parameters	Value
V magnitude	10.7
$T_{\rm eff}$	5034 K
Spectral Type	K3
Period (P)	4.24098 d
Transit Depth	0.021 mag
Transit Duration (t)	0.030 t/P
Transit Epoch	2453245.1886 HJD
R_A	0.85 $R_\odot$
R_B	1.2 R_J
RA(epoch=2000)	23h 43 m 18.41 s
Dec(epoch=2000)	+ 29d 55m 56.55 s

Observations taken from the SW North listed the primary star, J2343+29, likely to host an extrasolar planet having a temperature of 5034 K. The spectral type K3, a radius of $R_A =\ 0.85\ R_\odot$ and a transit depth of 21 mmag are estimated from SW photometry. The source showed substantial amount of scatter in the transit light curve and was suspected to be a stellar binary system as per preliminary observations done by SOPHIE (Collier Cameron *et al.*, 2007). Table 5.1 summarizes the basic stellar parameters for this source listed in the literature (Collier Cameron *et al.*, 2007). The primary stars in most of the EB systems discovered have F type primaries, some of these were discussed in Ch 4. Our programme object here is one of the three EB systems discovered yet which have K type primaries (Triaud *et al.*, 2013; Doyle *et al.*, 2011).

5.2 RV observations of J2343+29 with PARAS

High-resolution spectroscopic observations of the star J2343+29 were taken with the fiber-fed echelle spectrograph, PARAS at the 1.2 m telescope at Gurushikhar Observatory, Mount Abu, India. The details of the spectrograph, procedure adopted for observations and the data analysis techniques are discussed in Ch 2. The spectra were recorded in the simultaneous reference mode with ThAr as the calibration lamp. All the nights of observations were spectroscopic in nature. The magnitude of the source in the V band is ~ 10.7 which is the faint limit of observations possible with the 1.2m telescope and the PARAS combination. A set of 20 observations of the source acquired between November 2013 and January 2014 were used for fitting the orbital parameters of the system. The exposure time for the observations was chosen to be 1800 s to get a signal to noise ratio (SNR) between $12 - 14$ pixel^{-1} at 5500 Å for each spectra. The RV points that have a SNR less than 12 pixel^{-1} due to poor weather conditions or/and high air mass (Air Mass $\geqslant 1.5$) during observations were not considered for determination of orbital parameters. Table 5.2 gives details of the observation log. The first two columns represent the observation time in UT and BJD respectively. The exposure time and observed RV are given in the following columns. The RV error on each data point is given in the last column.

5.3 Results

5.3.1 Radial Velocity analysis

The PARAS data analysis pipeline, discussed in 4.2.2.1, is used for data reduction and analysis on J2343+29. RVs are derived by cross-correlating the target spectra with a suitable numerical mask. See Ch 2 for the details on the mask. In the present case, the numerical mask for K spectral type is used. Error on each RV measurement is based on the effect of photon noise (Bouchy, Pepe and Queloz, 2001) as described in § 4.2.2.2. The barycentric corrected RV values along with errors are in Table 5.2.

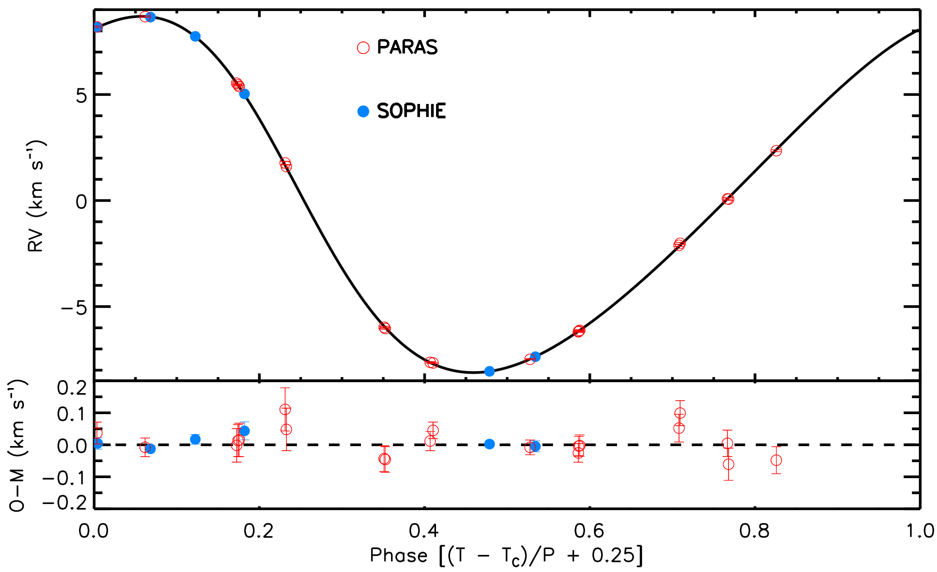

Figure 5.1: (Top panel) RV model curve for star for star J2343+29 obtained from EXOFAST is plotted against orbital phase. SOPHIE (filled blue circles) and PARAS, Mount Abu (open red circles) observed data points along with the estimated errors are overplotted on the curve. (Bottom panel) The residuals from best-fitting are plotted below the RV plot. For better visual representation, the x axis (Phase) is shifted by 0.25 so that the central primary transit crossing point (T_c) occurs at phase 0.25 instead of 0. P indicates the period.

In order to extend the timeline of observational date, we have combined

Table 5.2: RV Observations for the star J2343+29 taken with Mt Abu-PARAS.

UT Date	T-2,400,000 (BJD-TDB)	Exp. Time (sec.)	RV (m s^{-1})	σRV (m s^{-1})
2013 Nov 12	56609.15187	1800	−15367	35
2013 Nov 13	56610.14686	1800	−19126	39
2013 Nov 16	56613.12378	1800	−28527	43
2013 Nov 19	56616.16537	1800	−27088	29
2013 Dec 16	56643.08719	1800	−15443	15
2013 Dec 16	56643.10986	1800	−15517	22
2013 Dec 17	56644.07896	1800	−19293	45
2013 Dec 19	56646.08593	1800	−26868	17
2013 Dec 19	56646.10865	1800	−26928	24
2013 Dec 20	56647.09027	1800	−28554	29
2013 Dec 22	56649.08018	1800	−28379	26
2013 Dec 23	56650.07829	1800	−27054	26
2013 Dec 23	56650.10118	1800	−27016	40
2014 Jan 11	56669.09172	1800	−23005	32
2014 Jan 11	56669.11451	1800	−22908	43
2014 Jan 12	56670.08510	1800	−20812	37
2014 Jan 12	56670.10783	1800	−20825	58
2014 Jan 13	56671.08817	1800	−18543	42
2014 Jan 16	56674.09761	1800	−12707	53
2014 Jan 17	56675.08732	1800	−12219	56

SOPHIE archival data between August 2006 to August 2007 with PARAS observations. A set of 6 observations of the star during the aforementioned period was retrieved from the SOPHIE archival data [1]. The SOPHIE observations for the source J2343+29 were obtained in the High Efficiency (HE) mode of

[1]http://atlas.obs-hp.fr/sophie/

Table 5.3: Archival data obtained for the star J2343+29 from SOPHIE observations.

UT Date	T-2,400,000 (BJD-TDB)	Exp. Time (sec.)	RV (m s^{-1})	σRV (m s^{-1})
2006 Aug 31	53978.50771	900	-12981	16
2006 Sep 01	53979.59139	900	-12502	10
2006 sep 02	53980.51167	900	-13410	08
2006 Sep 03	53981.52070	900	-16122	10
2007 Aug 30	54342.57369	1500	-29170	08
2007 Aug 31	54343.51469	1800	-28481	06

SOPHIE having a resolving power of $\sim$ 40000 covering the wavelength region $3872-6943$ Å. SOPHIE data were processed by the standard SOPHIE pipeline and passed through weighted cross-correlation with a numerical mask (Pepe *et al.*, 2002). As per the header information in the downloaded archival data the SNR for each epoch varied in the range between $\sim 25 - 75$ pixel^{-1} at 5500 Å. The errors on RV were calculated by the semi-empirical estimator $\sigma_{RV} = A \times \sqrt{FWHM}/(SNR \times C)$ as suggested by West *et al.* (2009) for SOPHIE data. External systematic errors of 2 m s^{-1} (spectrograph drift uncertainty) and 4 m s^{-1} (guiding errors) were quadratically added (Boisse *et al.*, 2010) to the obtained statistical errors. The RV values from SOPHIE archival data along with observation log and the errors on each point are given in Table 5.3.

Using EXOFAST (Eastman, Gaudi and Agol, 2013) (See § 4.2.2.5 for details), the spectroscopy data from PARAS and SOPHIE spectrograph were fitted. The priors of $T_{\rm eff} = 5125 \pm 50$ K, $[Fe/H] = 0.1 \pm 0.05$, and $\log g = 4.6 \pm 0.1$ were provided to EXOFAST. These priors are estimated on the basis of detailed spectroscopic analysis done by the code *PARAS SPEC* as discussed in Ch 3. RV values were corrected for the offset between the two spectrographs which amounted to 257 m s^{-1}. The obtained results are summarised in Table 5.4 of column *"RV only"*. The period of the EB is determined as $\sim$ 16.953 d with a RV semi-amplitude of 8394 m s^{-1}. Fig. 5.1 illustrates the RV variation with orbital phase for J2343+29. Red open circles (top panel) show RV measurements of the star taken with the PARAS and solid blue circles denote those taken with SOPHIE. The solid black curve indicates the best-fit model from EXOFAST based on the parameters listed in Table 5.4. The bottom panel in Fig. 5.1 shows the model fit and the residuals (Observed-Model).

5.3.2 *SuperWASP* photometry

The light curve for J2343+29 as seen in Fig. 17 of Christian *et al.* (2006) shows a moderate amount of scatter and an ellipsoidal amplitude of 2.9 hinting a possibility of stellar binary. These authors identified a period of 4.24 d whereas RV data (this work) shows a periodicity of 16.953 d. The misidentification in the period by SW photometry could be due to the fact that the automated SW pipeline is intended to search for short period planets typically less than 5 d. The probability to search for transits by SW photometry which are integral multiples of 1 d or 1.5 d is comparatively low at around $\sim$ 35% (Street *et al.*, 2007) due to this inadequate sampling. Since, J2343+29 has a RV determined period of 16.953 d (which is much higher than 5 d and also a close integral multiple of 1 d), there is greater likelihood of not sampling the source well in phase during the entire transit duration of the source. There are 6 transits detected for this source at $\sim$ 4.24 d periodicity as reported in Christian *et al.* (2006). Due to relatively less number of recorded transits, the phase coverage of the transit event is expected to be poor with fewer data points.

The transit data-set was fitted individually. For this execution, the period was kept fixed to 16.953 d (value obtained from the *"RV only"* result) by supplying it as an additional prior to EXOFAST along with the pre-existing priors on $T_{\rm eff}$ and $[Fe/H]$. It was possible to independently obtain the log g value of $4.62^{+0.19}_{-0.17}$ from the transit data alone. The log g value derived is consistent when compared with the one derived from spectral analysis (this work) as discussed in §4. It is also in close agreement to the results obtained from the log g value obtained from the *"RV only"* execution by EXOFAST. The log g derived from only photometry has larger error bars associated due to the sparse and noisy photometry data. A comparison of individual values has been put up in Table 5.4. The results from transit data is included in the column of *"Transit: fixed period"*.

5.3.3 Simultaneous spectroscopy and photometry fitting

Fitting separately RV and transit data, the combined RV datasets and light curve data points were then fitted simultaneously in order to impose better constraints on the execution by EXOFAST.

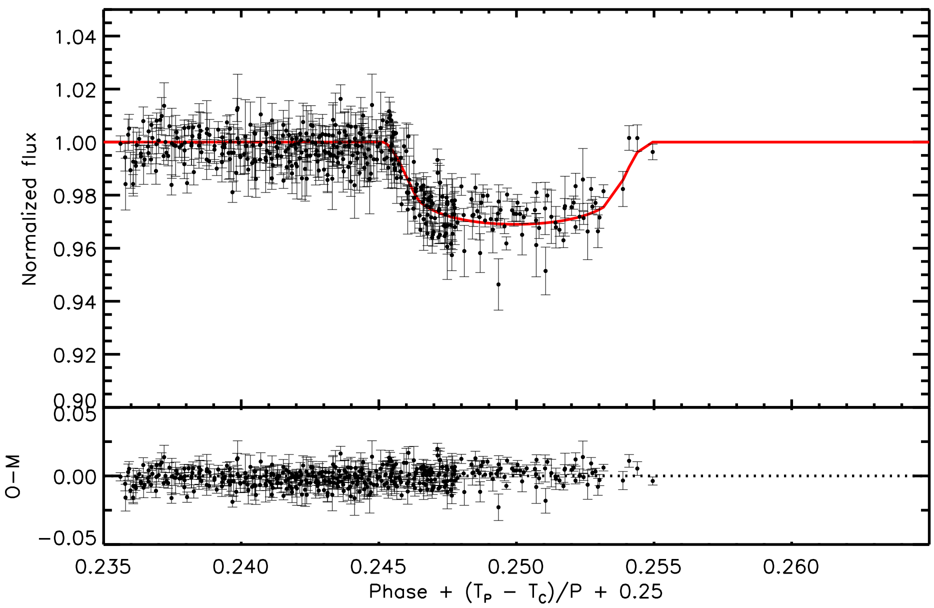

Figure 5.2: (Top panel) Transit curve obtained for star J2343+29 from SW data. The transit model obtained from EXOFAST is overplotted on the data points. (Bottom panel) Observed-Fit residuals are plotted. For better visual representation, the x axis (Phase) is shifted by 0.25 so that the central primary transit crossing point (T_c) occurs at phase 0.25 instead of 0.

Table 5.4: Results obtained from EXOFAST for J2343+29

Parameter	RV only	Transit-fixed period	Combined RV-Transit
Component A:			
M_A (M⊙)	$0.871^{+0.021}_{-0.020}$	$0.865^{+0.050}_{-0.027}$	$0.874^{+0.044}_{-0.041}$
R_A (R⊙)	$0.771^{+0.047}_{-0.041}$	$0.75^{+0.17}_{-0.14}$	$0.825^{+0.030}_{-0.027}$
$\log(g_A)$	$4.600^{+0.048}_{-0.049}$	$4.62^{+0.19}_{-0.17}$	$4.547^{+0.024}_{-0.025}$
$T_{\rm eff}$ (K)	5125^{+51}_{-49}	5116^{+57}_{-56}	5132 ± 48
[Fe/H]	$0.099^{+0.070}_{-0.073}$	$0.088^{+0.068}_{-0.057}$	0.097 ± 0.069
Component B:			
e	0.1586 ± 0.0016	$0.28^{+0.35}_{-0.17}$	0.1599 ± 0.0012
ω_* (degree)	$78.04^{+0.59}_{-0.58}$	40^{+100}_{-140}	77.64 ± 0.41
P (days)	16.95346 ± 0.00007	16.95349 ± 0.00004	16.95351 ± 0.00003
a (AU)	0.123 ± 0.001	$0.123^{+0.002}_{-0.001}$	0.128 ± 0.002
M_B (M⊙)	$0.098 \ \pm 0.002$	-	$0.098 \ \pm 0.003$
R_B (R⊙)	-	$0.120^{+0.004}_{-0.003}$	$0.127^{0.005}_{-0.004}$
RV Parameters:			
T_P(BJD)	$2454914.723^{+0.026}_{-0.025}$	$2453593.3^{+1.6}_{-3.6}$	2453592.326 ± 0.014
K (m s^{-1})	8394 ± 7	-	8399 ± 6
M_B/M_A	$0.1124^{+0.0001}_{-0.0009}$	-	0.1124 ± 0.0019
γ (m s^{-1})	-21014 ± 10	-	-21021 ± 8
Transit Parameters:			
T_C (BJD)	-	$2453592.7430^{+0.0019}_{-0.0014}$	$2453592.7431^{+0.0019}_{-0.0017}$
R_B/R_A	-	$0.1603^{+0.0030}_{-0.0026}$	0.1586 ± 0.0020
i (degree)	-	$89.79^{+0.17}_{-0.54}$	$89.80^{+0.14}_{-0.19}$
a/R_A	-	$35.1^{+8.5}_{-6.2}$	$33.36^{+0.94}_{-1.00}$
δ		0.026 ± 0.001	0.025 ± 0.001
T_{14} (min)	-	229^{+6}_{-5}	229 ± 6

The results of the execution are summarized in Table 5.4 in the column of *"Combined RV-transit"*. The period of the EB is determined as 16.95351 ± 0.00003 d with a RV semi-amplitude of 8399 ± 6 km s^{-1}. The orbital separation between the EB components is 0.128 ± 0.002 AU. Fig. 5.2 (upper panel) shows the simultaneous fit for the transit light curve obtained by analyzing SW photometry data (filled circles) overplotted with the model derived from EXOFAST (solid curve). The residuals are plotted in lower panel. The simultaneous fit gives us a transit depth of 0.025 ± 0.001 mag, angle of inclination of $89.80^{+0.14\circ}_{-0.19}$ and a transit time duration of 229 ± 6 min. Although a clear transit dip is seen in the light curve, it is noticed that there are fewer data points close to the egress of the transit.

5.3.4 Spectral analysis using *PARAS SPEC*

PARAS SPEC was used for determination of stellar properties for J2343+29. The code uses both the methods of synthetic spectral fitting and EW method for estimation of stellar properties. A total of 28 observed spectra were co-added for the source to get a SNR of $65 - 70$ in the blue end ($5000 - 6000$ $\AA$). This SNR per pixel obtained is less than 80 and thereby as mentioned in Ch 3, is insufficient for the synthetic spectral fitting method to operate in the blue end. Hence, the red end of the spectra ($6000 - 6500$ $\AA$) is utilized for which the SNR per pixel for the co-added spectra is ~ 85. $T_{\rm eff}$ and $[Fe/H]$ are determined by the synthetic spectral fitting method but log g could not be determined by this method due to omission of the wavelength region having Mg lines ($5160 - 5190$ $\AA$). Thus, for estimation of log g with other stellar parameters, the EW method is applied on the star J2343+29. For a fixed value of $[Fe/H]$, we calculated $T_{\rm eff}$, log g and $v_{\rm micro}$. The list of unblended spectral lines considered for analysis by the EW method are given in Table 5.6. The spectral properties determined by PARAS SPEC for J2343+29 are summarized in Table 5.5.

The $T_{\rm eff}$ determined for the star is close to the photometry derived $T_{\rm eff}$ as given in Collier Cameron *et al.* (2007). The best-fit model spectra determined

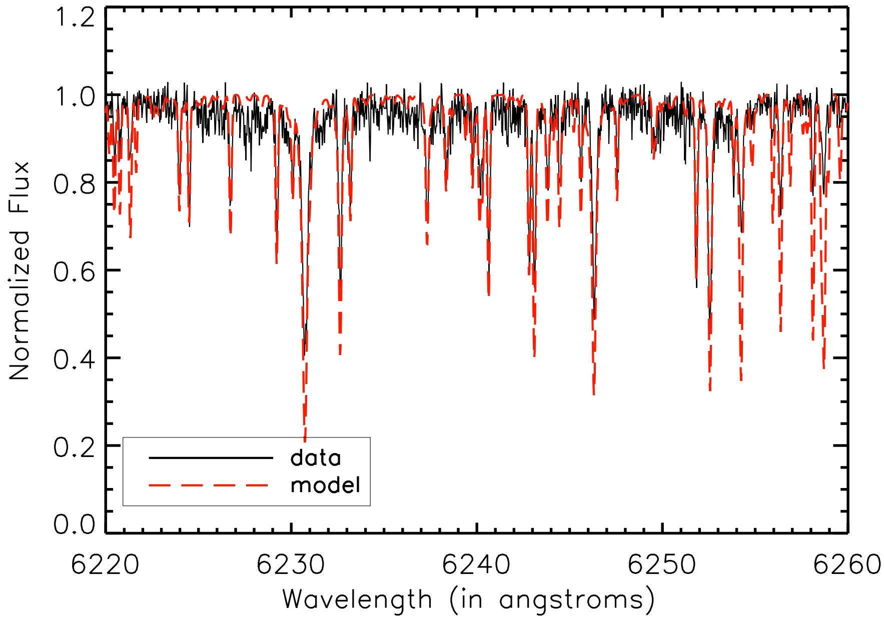

Figure 5.3: Observed normalized spectra for J2343+29 (solid black line) plotted across the wavelength region of $6220 - 6260$ $\mathring{A}$. Overplotted is the modelled spectra (red dash line) obtained from PARAS SPEC analysis, with temperature value of $T_{\rm eff}$ of 5125 K, $[Fe/H]$ of +0.1 and log g of 4.6.

Table 5.5: Spectral properties of J2343+29 as derived by *PARAS SPEC*

Parameters	Value	Error
$T_{\rm eff}$	5125	± 50
$[Fe/H]$	0.1	± 0.1
log g	4.6	± 0.1
$v_{\rm micro}$	1.2	± 0.05
$v \sin i$	3.16 (fixed)	± 0.5

for J2343+29 is shown in Fig. 5.3. The red solid line indicates the observed normalized spectra from PARAS and the overlaid black dotted line is the best-fit model determined from this work.

Table 5.6: Spectral lines used for EW method for J2343+29 in *PARAS SPEC*

Wavelength (Å)	Element	Wavelength (Å)	Element
4962.58	Fe I	5704.72	Fe I
5012.72	Fe I	5752.04	Fe I
5049.85	Fe I	5775.09	Fe I
5074.76	Fe I	5838.38	Fe I
5088.16	Fe I	5883.83	Fe I
5197.96	Fe I	5930.18	Fe I
5225.52	Fe I	5934.69	Fe I
5228.39	Fe I	6005.59	Fe I
5281.79	Fe I	6008.56	Fe I
5285.13	Fe I	6078.49	Fe I
5294.55	Fe I	6096.67	Fe I
5295.32	Fe I	6127.91	Fe I
5307.36	Fe I	6165.35	Fe I
5373.71	Fe I	6232.64	Fe I
5398.28	Fe I	6246.33	Fe I
5417.04	Fe I	6315.81	Fe I
5436.30	Fe I	6421.35	Fe I
5441.35	Fe I	6430.85	Fe I
5466.40	Fe I	6481.87	Fe I
5466.99	Fe I	6496.47	Fe I
5494.46	Fe I	6498.94	Fe I
5619.60	Fe I	6569.21	Fe I
5635.80	Fe I	6574.23	Fe I
5638.26	Fe I	5132.62	Fe II
5641.44	Fe I	5234.63	Fe II
5651.47	Fe I	5534.84	Fe II
5653.85	Fe I	6238.35	Fe II
5655.17	Fe I		

In Fig. 5.4, a least-square fit line in blue having minimum slope for iron abundances vs. excitation potential indicative of best-fit T_{eff} for J2343+29 is shown in the upper panel.In the bottom panel, a plot of iron abundance vs reduced EW is shown. The blue-green colour line overplotted indicates the least-square fit line for minimum slope indicating the best-fit v_{micro}.

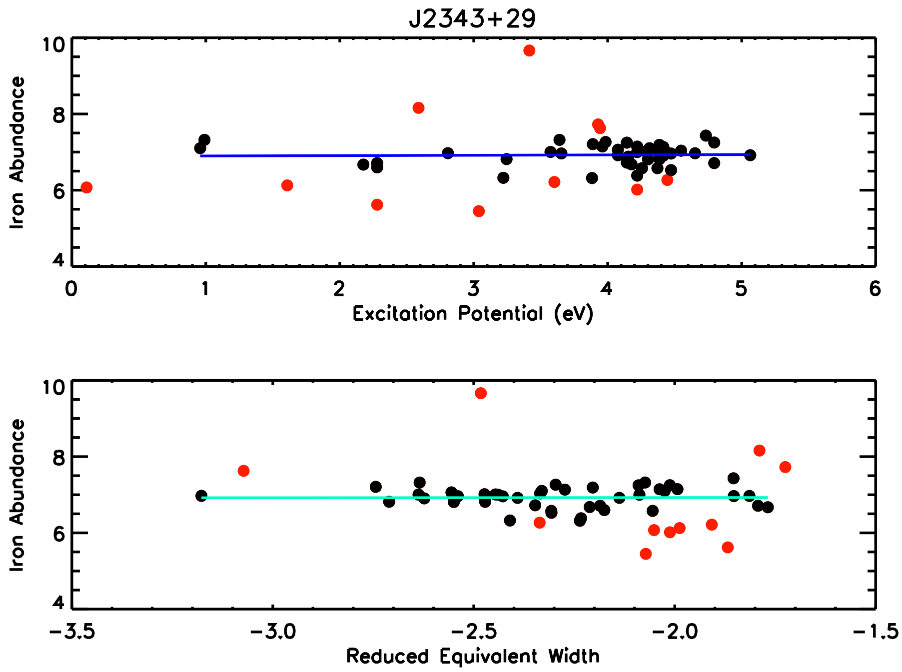

Figure 5.4: (Top panel) Iron abundance for J2343+29 is plotted against excitation potential for each Fe I or Fe II line from the line list. The blue line is the least-square fit for the minimum slope for the best-determined model temperature. (Bottom panel) Iron abundance is plotted against reduced EW and the blue-green line indicates the least-square slope for minimum slope for best-determined v_{micro}. The red points are the discarded points having standard deviation beyond 1 σ (not considered for the fit). The best-fit determined parameters are: T_{eff} = 5125 K, $[Fe/H]$ = 0.1, log g = 4.6, v_{micro} = 1.2 km s^{-1}

5.4 Discussion

Based on spectral analysis and modelling from EXOFAST, the mass and radius are determined and thereby the spectral type of the primary star is concluded to be K1 instead of K3 as listed in Table 5.1. With an angle of inclination determined at $89.80°^{+0.14}_{-0.19}$ and the RV semi-amplitude (K) to be 8399 ± 6 m s^{-1} from the combined spectroscopy and photometry fitting, the mass of the secondary star is derived to be 0.098 ± 0.003 M$_\odot$.

Based on the primary star's $T_{\rm eff}$ and spectral type, the absolute magnitude of the star can be roughly estimated as $\sim$ 6.4 (Cox, 2000). A knowledge of apparent and absolute magnitudes of the same star helps us to determine its distance; $\sim$80 pc for this case, indicative of it lying in the solar neighbourhood. In order to compute the age of the system, the rotational period of the star must be determined (Meibom *et al.*, 2015). Thus the $v \sin i$ of 3.16 km s^{-1} is determined based on its CCF width. Since the radius of the primary star derived from this work is $\sim$ 0.82 $R_\odot$, the rotational period of 13.3 d is calculated. The calculated rotational period of the star, helps in estimating the age of the star to be between 1-2 Gyr (Meibom *et al.*, 2015). The estimated circularization and synchronization times for the system estimated based on Zahn (1977) is more than the age of the system. The observations reflect the same, as the EB has yet not synchronized with the rotational velocity of the star and has an eccentricity of $\sim$0.16.

From Baraffe *et al.* (1998) models, the theoretical radius for $\sim$0.098 $M_\odot$ turns out to be 0.12 ± 0.01 $R_\odot$ for $[M/H] = 0.0$. The value of radius determined from observations based on transit depth is $R_B = 0.127^{+0.005}_{-0.004}$ $R_\odot$. Although the observational value of radius is dependent on the accuracy of the models used, within the error bars of the fitting for orbital parameters, it can be concluded that nearly no discrepancy is seen to be associated between the observed and theoretically derived radius. This substantiates the claim by López-Morales (2007) that observations for stars having masses sufficiently less than 0.3 $M_\odot$ match well within the models.

In order to examine the M-R relation in the VLMS region, it is very important to increase the statistical sample size of such objects studied at high precision. Out of 26 systems studied previously in literature, in the mass range of $0.08 - 0.4$ $M_\odot$ as shown in Table 4.15, there have been only 6 systems having masses between $0.08 - 0.2\ M_{\odot}$ studied with accuracies better than a few per cent (Beatty *et al.*, 2007; Doyle *et al.*, 2011; Triaud *et al.*, 2013; Nefs *et al.*, 2013; Fernandez *et al.*, 2009). We replot the previously shown M-R plot (Fig 4.13) in Ch 4 as Fig. 5.5 by adding the recently studied source, J2343+29B. This plot consists of the VLMS objects studied from this thesis work (red circles), three M dwarfs detected in F+M systems (refer Ch 4) and the one, J2343+29B, discussed in this Chapter along with the VLMS objects previously studied in literature (black circles). J2343+29 is the EB wherein the companion is the second least massive star studied at a high accuracy of $4 - 5\%$ for mass and radius measurements, second only to system J1219−39 as seen from Table 4.15 as well as Fig. 5.5. Most of the EBs form in M+M systems, with F type primaries being the second most probable primary hosts for M dwarfs, which is evident from Table 4.15 (Bouchy *et al.*, 2011a). The rotational velocities of G and K dwarfs are between $2 - 3$ km s^{-1} (Gray, 1984) and thereby the effect of tides raised by shorter period companions is considerable (Counselman, 1973). There are only 3 EB systems discovered which have G/K type primaries, the ones highlighted in boldface in the table. Out of the three systems, J0113+31 and KEPLER16 have relatively longer periods of ~ 14 and 41 d respectively, similar to the EB studied here, (J2343+29 with a ~ 17 d period). As shown by Zahn (1977) and references therein, the orbital separation of the system will decay only if the spin period of the star is larger than the orbital period of the system. Since the rotational period of J2343+29 (13.3 d, calculated by the knowledge of rotational velocity) is smaller than the orbital period (16.953 d), a stable orbit for the system is envisaged. For the case of K+M systems, long period EBs are thereby expected to have a stable evolution and hence, J0113+31 and KEPLER16 will have a stable orbit. In this context, it will be worthy enough to study J1219-39B for its stability which has a relatively short period of ~ 6 d.

As seen from the figure, there are only 6 objects including the system J2343+29B which have masses $\leqslant 0.2$ M$_{\odot}$. These objects tend to follow the theoretical M-R relationship much closely than compared to more massive stars

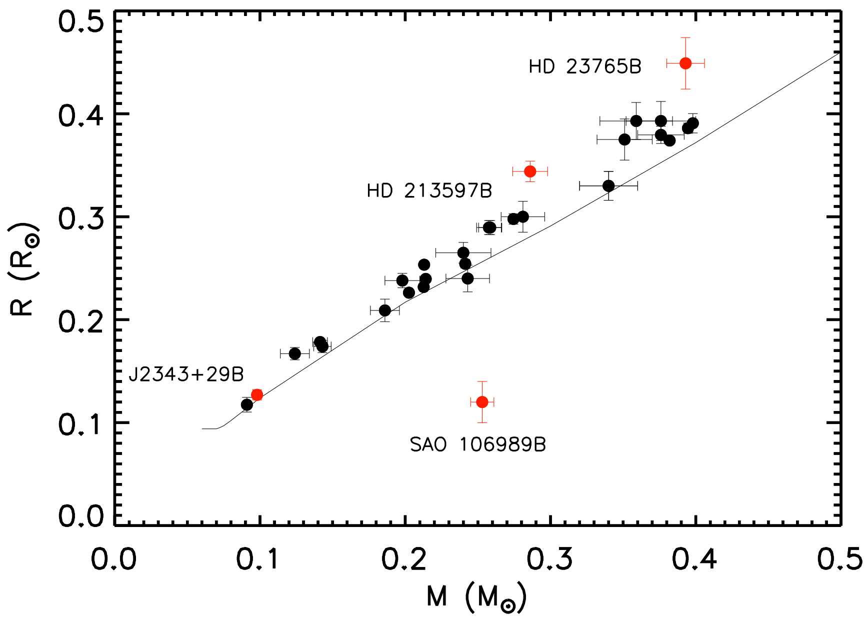

Figure 5.5: Mass-Radius diagram for M dwarfs based on Barffe models for 1 Gyr isochrone and solar metallicity. Overplotted are the previously studied M dwarfs listed in Table 4.15 with black filled circles with their reported uncertainties. All the four M dwarfs discovered by PARAS (in three F+M EBs and in one K+M EB) with error bars. HD 23765B, HD 213597B and J2343+29B have both masses and radii determined from this work whereas for SAO 106989B, the projected mass is derived from this work and the radius is based on measurement from SW photometry

(Fig 4.13). However, there are relatively fewer samples in this mass-regime to substantiate this claim. We have contributed one VLMS object in this mass regime (J2343+29B), which clearly falls on the 1 Gyr isochrone agreeing to the theoretically predicted radius measurement.

The q ($= M_B/M_A$) of this system is (~ 0.1) which is a rarity amongst short orbital period EBs. (See Figure 9 of Wisniewski *et al.* (2012)). Due to its low q value, this object seems to reside in a mass ratio - period deficit for low mass stellar binaries. Short period, low q companions are, for the above mentioned reasons, more probable to be found around F type stars in contrast to G and K type stars. A variety of similar EBs with VLMS as one of the components should be studied in detail to assess our understanding of evolutionary mechanism of such systems. The fitting errors reported here on the orbital parameters are dependent on the models in the SB1 system. Thus, J2343+29 serves as a benchmark VLMS studied in EB, which can be followed up in future for a SB2 (double-lined eclipsing binary) solution to constrain the mass and radii of the components more precisely.

5.5 Summary of the results for J2343+29

The important results for J2343+29 are summarized here as follows:

- By spectroscopic analysis, stellar parameters for J2343+29A are determined to be $T_{\rm eff} = 5125 \pm 51$ K, $[Fe/H] = 0.1 \pm 0.05$ and $\log g = 4.6 \pm 0.1$. Hence, the primary J2343+29A has a mass of $0.874^{+0.043}_{-0.041}$ M⊙ and a radius of $0.825^{+0.030}_{-0.027}$ R⊙.

- Using high-resolution spectroscopy taken with PARAS and combining SOPHIE archival data for RV and SW archival data for photometry, the RV semi amplitude for J2343+29 is determined as 8399 ± 6 m s^{-1}. The secondary mass from RV measurements is $M_B = 0.098 \pm 0.003\ M_\odot$ with an accuracy of $\sim$ 3 per cent (formal errors). Hence, it is concluded that J2343+29 is an EB with a K1 primary and a M7 secondary (Pecaut and Mamajek, 2013). The period of the EB, based on combined RV and SW photometry measurements is corrected to 16.953 d as against that of previously reported value of 4.24 d. Inadequate phase coverage while searching for intended short period planets by the automated SW pipeline is thought to be the reason for incorrect determination of the period.

- The light curve data for J2343+29A is fitted simultaneously with RV data to determine the depth which is 25 mmag. Based on the transit depth, the radius of the J2343+29B is estimated as $R_B = 0.127^{+0.005}_{-0.004}\ R_\odot$ with an accuracy of $\sim$ 5 per cent (formal errors). The observed radius is consistent with the theoretically derived value from Baraffe models.

- Based on the calculation of orbital period (16.953 d) and spin period (13.3 d) of the star J2343+29A, it can be concluded that the K+M system studied here will have a stable orbit. However, it needs to spend some more time before it circularizes by the tidal forces existing between the components.

Chapter 6

Summary and Future Work

We have presented in the preceding Chapters the work done for obtaining and interpreting the physical and orbital parameters of very low mass stars (VLMS) in the mass range of $0.085 - 0.4$ $M_{\odot}$ occurring in eclipsing binary (EB) systems using the techniques of precision spectroscopy and photometry. As a part of the EB program carried out at PRL, radial velocity (RV) observations with Physical research laboratory Advanced Radial velocity Abu sky Search (PARAS) coupled to the 1.2 m telescope and follow-up photometry (ground-based or space-based) were used to estimate the mass and radius of VLMS in a selection of 4 EB systems. In this Chapter, we summarize the important results obtained from the dissertation work followed up by the proposed scientific plans which can be pursued in future.

6.1 Summary

The important results on the four EBs are highlighted in Table 6.1. It lists the masses, radii, spectral types of both the components in the binary system along with their orbital period.

Table 6.1: Summary of the results for VLMS in EB systems discovered by PARAS

Parameters	HD 213597	HD 23765	SAO 106989	J23343+295
M_A ($M_\odot$)	$1.293^{+0.12}_{-0.1}$	$1.507^{+0.086}_{-0.071}$	$1.1099^{+0.055}_{-0.049}$	$0.874^{+0.044}_{-0.041}$
R_A ($R_\odot$)	$1.973^{+0.085}_{-0.080}$	$2.29^{+0.12}_{-0.11}$	$1.29^{+0.17}_{-0.15}$	$0.825^{+0.030}_{-0.027}$
Spectral Type (A)	F3	F6	F9	K1
M_B ($M_\odot$)	$0.286^{+0.012}_{-0.01}$	$0.393^{+0.014}_{-0.013}$	$0.254^{+0.008}_{-0.007}$	0.097 ± 0.069
R_B (Observed) ($R_\odot$)	$0.344^{+0.097}_{-0.01}$	0.449 ± 0.025	0.12 ± 0.02	$0.127^{0.005}_{-0.004}$
R_B (Theoretical) ($R_\odot$)	0.28 ± 0.01	0.372 ± 0.02	0.25 ± 0.02	0.12 ± 0.02
Spectral Type (B)	M4	M3	M4	M7
Period (days)	$2.4238503^{+0.000017}_{-0.0000019}$	1.68668 ± 0.00039	$4.426^{+0.026}_{-0.023}$	16.95351 ± 0.00003

As seen from the table, we have detected three F+M EBs, wherein the M dwarfs have mass range close to the transition between radiative and convective zones ($\sim$ 0.3 $M_\odot$). The fourth EB is a K+M EB, wherein the M dwarf is the second least massive star studied for its mass and radius at such high precisions. Out of the four M dwarfs studied as part of EBs, the radii estimated for two M dwarfs, namely, HD 213597B and HD 23765B are higher than the theoretical values as seen in Fig. 5.5. The radius estimated for the third M dwarf, SAO 106989B is less than the theoretically derived value. Since, this result is not verified by us independently, we seek independent transit photometry measurements to draw any conclusion. The radius for the last M dwarf, J2343+29B, is consistent with the theoretical models. This research work has contributed $\sim$ 12% more samples to the existing 26 samples with masses and radii measurements at accuracies $\leqslant$ 10%. Since, some of the sources still do not follow the theoretical models, between the convective and radiative boundary zone, we believe that the models need to be carefully inspected further. The latest Baraffe *et al.* (2015) models used here for comparison are only for solar metallicity. Extension of this work for non-solar metallicity might help us draw a better estimation on the comparison of observations with the models. The mixing length parameter (α) used for the models is kept fixed in this case. However, it depends on the metallicity of the star (Bonaca *et al.*, 2012). This study concludes that results obtained by fitting stellar models constructed with solar values of α for all kind of stars without accounting for non-solar values of mixing-length parameter are likely to have large systematic errors. This aspect needs to be further taken into account for a better match of models with observations.

As a part of the thesis work, a software code, *PARAS SPEC* was developed for determination of spectral properties of the stars studied with PARAS. The two main approaches used here are, (i) the synthetic spectral fitting method and (ii) the EW fitting method. These methods when applied to some well-known stars agreed well within error bars with the values reported in literature.

6.2 Scope for Future Study

Study of M-R relation for VLMS objects and comparing them with theoretical isochrones require a large number of unbiased samples over a range of different ages and metallicities. Precise determination of masses and radii requires observation of objects in double-lined EBs. The objects studied as a part of this thesis require follow-up observations on larger telescopes (eg. HET, VLT) that can be taken up in future in order to obtain a double-lined EB solution for a precise study of their masses and radii. For the current work, we have concentrated on objects lying in the mass range of $0.085 - 0.4$ $M_\odot$, as the objects in this mass regime were not previously studied extensively. We aim to increase the sample size and also extend our study below the hydrogen burning mass limit by looking for brown dwarfs around solar like stars. It is found that fewer brown dwarfs reside in close proximity (within 5 AU) of their host stars; an issue termed as brown dwarf desert (Grether and Lineweaver, 2006). We plan to search and characterize such brown dwarfs with PARAS in future.

Efforts are underway at PRL to install and commission a 2.5 m telescope by $2019 - 2020$ and PARAS (with a few modifications) will be one of the core focal plane instrument at the new telescope. Doubling the primary aperture shall quadruple the SNR obtained on each stellar spectra for similar exposure time. This will enhance our capabilities with PARAS at the 2.5 m telescope for fainter targets. With the current existing 1.2 m telescope, we are able to observe stars having magnitude as faint as 10.5. With the advent of the new telescope, we will be able to observe stars as faint as 12^{th} magnitude with a similar SNR per pixel for same exposure time. With several new upcoming missions such as Kepler's K2 NASA mission (Howell *et al.*, 2014), TESS (Transiting Exoplanet Survey Satellite) (Ricker *et al.*, 2015), PLATO (PLAnetary Transits and Oscillations of stars) (Catala, 2009), CHEOPS (CHaracterising ExOPlanet Satellite) (Fortier *et al.*, 2014), there shall be a plethora of new exoplanets and EB candidates which can be studied by the RV technique. Most of the candidates will be studied with high precision and shall have magnitudes between $9 - 12$ which can serve as excellent follow-up candidates with PARAS.

To operate hand-in-hand with PARAS, we also plan to observe the transits of Jupiter-like objects or VLMS objects across F, G or K type stars to complement the RV observations made by PARAS. For this purpose, a 43 cm aperture telescope is being commissioned in the near future with a field of view close to $1° \times 1°$ to monitor stars at $1 - 2$ mmag accuracies. A 20 arcmin $\times$ 20 arcmin CCD attached with the 2.5 m telescope will be advantageous to do photometry at high precision with sub-mmag accuracies. Some of the objects can be studied for RV measurements simultaneously during their transits. Such studies can focus on studying the Rossiter-McLaughlin effect (Gaudi and Winn, 2007). This helps to determine whether the secondary star is in retrograde or prograde orbital motion with respect to the rotation of the primary. Such studies can be helpful to investigate the formation mechanisms of binary stars.

There is scope for improvement in the *PARAS SPEC* pipeline. We will generalize the routine so that it can handle data from different spectrographs at different resolving powers. In order to study the chemically peculiar stars, non-solar abundances must be incorporated in the code. F type stars have relatively higher temperatures and have more absorption features in the blue region of the spectra ($5000 - 6000$ Å). For fainter stars, SNR per pixel in the blue region of the spectra is less. Methods will be developed to match the stellar continuum in a better way for accurate determination of stellar parameters. Moreover, we cannot use Mg I lines ($5160 - 5190$ Å) for the estimation of $\log g$ for stars having low SNR. In K type stars, Ca I line (6162.17 Å) can be used for determination of $\log g$. Algorithms will be developed to accommodate these options in the *PARAS SPEC* pipeline.

References

Ammler-von Eiff, M., Reiners, A.: 2012, New measurements of rotation and differential rotation in A-F stars: are there two populations of differentially rotating stars? *Astron. Astrophys.* **542**, A116.

Anders, E., Grevesse, N.: 1989, Abundances of the elements - Meteoritic and solar. *Geochimica et Cosmochimica Acta* **53**, 197 – 214.

Andersen, J.: 1975, Spectroscopic observations of eclipsing binaries IV. Absolute dimensions of the giant system SZ Centauri. *Astron. Astrophys.* **45**, 203 – 208.

Andersen, J.: 1991, Accurate masses and radii of normal stars. *Astron. Astrophys. Rev.* **3**, 91 – 126.

Andersen, J.: 1998, Proceedings of the Twenty-third General Assembly of the IAU. *Highlights of Astronomy* **11**.

Andersen, J., Clausen, J.V.: 1989, Absolute dimensions of eclipsing binaries. XV - EM Carinae. *Astron. Astrophys.* **213**, 183 – 194.

Armitage, P.J., Bonnell, I.A.: 2002, The brown dwarf desert as a consequence of orbital migration. *Mon. Not. Roy. Astron. Soc.* **330**, L11 – L14.

Asplund, M., Grevesse, N., Sauval, A.J.: 2005, The Solar Chemical Composition. In: Barnes, T.G. IIIBash, F.N. (eds.) *Cosmic Abundances as Records of Stellar Evolution and Nucleosynthesis*, *Astronomical Society of the Pacific Conference Series* **336**, 25.

Asplund, M., Grevesse, N., Sauval, A.J., Scott, P.: 2009, The Chemical Composition of the Sun. *ARA&A* **47**, 481 – 522.

Ballard, S., Johnson, J.A.: 2014, The Kepler Dichotomy among the M Dwarfs: Half of Systems Contain Five or More Coplanar Planets. *ArXiv e-prints*.

Baraffe, I., Chabrier, G.: 1996, Mass–Spectral Class Relationship for M Dwarfs. *Astrophys. J. Lett.* **461**, L51.

Baraffe, I., Chabrier, G., Barman, T.: 2008, Structure and evolution of super-Earth to super-Jupiter exoplanets. I. Heavy element enrichment in the interior. *Astron. Astrophys.* **482**, 315 – 332.

Baraffe, I., Chabrier, G., Allard, F., Hauschildt, P.H.: 1998, Evolutionary models for solar metallicity low-mass stars: mass-magnitude relationships and color-magnitude diagrams. *Astron. Astrophys.* **337**, 403 – 412.

Baraffe, I., Homeier, D., Allard, F., Chabrier, G.: 2015, New evolutionary models for pre-main sequence and main sequence low-mass stars down to the hydrogen-burning limit. *Astron. Astrophys.* **577**, A42.

Baranne, A.: 1972, Equipement spectrographique du foyer coudé du télescope de 3.60 mètres. Etude de faisabilité d'un spectrographe universel. In: Laustsen, S.Reiz, A. (eds.) *Auxiliary Instrumentation for Large Telescopes*, 227 – 239.

Baranne, A., Queloz, D., Mayor, M., Adrianzyk, G., Knispel, G., Kohler, D., Lacroix, D., Meunier, J.P., Rimbaud, G., Vin, A.: 1996, ELODIE: A spectrograph for accurate radial velocity measurements. *Astron. Astrophys. Suppl.* **119**, 373 – 390.

Beatty, T.G., Fernández, J.M., Latham, D.W., Bakos, G.Á., Kovács, G., Noyes, R.W., Stefanik, R.P., Torres, G., Everett, M.E., Hergenrother, C.W.: 2007, The Mass and Radius of the Unseen M Dwarf Companion in the Single-Lined Eclipsing Binary HAT-TR-205-013. *Astrophys. J.* **663**, 573 – 582.

Bender, C.F., Mahadevan, S., Deshpande, R., Wright, J.T., Roy, A., Terrien, R.C., Sigurdsson, S., Ramsey, L.W., Schneider, D.P., Fleming, S.W.: 2012, The SDSS-HET Survey of Kepler Eclipsing Binaries: Spectroscopic Dynamical Masses of the Kepler-16 Circumbinary Planet Hosts. *Astrophys. J. Lett.* **751**, L31.

Berger, D.H., Gies, D.R., McAlister, H.A., ten Brummelaar, T.A., Henry, T.J., Sturmann, J., Sturmann, L., Turner, N.H., Ridgway, S.T., Aufdenberg, J.P., Mérand, A.: 2006, First Results from the CHARA Array. IV. The Interferometric Radii of Low-Mass Stars. *Astrophys. J.* **644**, 475 – 483.

Birkby, J., Nefs, B., Hodgkin, S., Kovács, G., Sipőcz, B., Pinfield, D., Snellen, I., Mislis, D., Murgas, F., Lodieu, N., de Mooij, E., Goulding, N., Cruz, P., Stoev, H., Cappetta, M., Palle, E., Barrado, D., Saglia, R., Martin, E., Pavlenko, Y.: 2012, Discovery and characterization of detached M dwarf eclipsing binaries in the WFCAM Transit Survey. *Mon. Not. Roy. Astron. Soc.* **426**, 1507 – 1532.

Blackwell, D.E., Booth, A.J., Petford, A.D.: 1984, Is there an abundance anomaly for the 2.2 eV Fe I lines in the solar spectrum? *Astron. Astrophys.* **132**, 236 – 239.

Blanco-Cuaresma, S., Soubiran, C., Heiter, U., Jofré, P.: 2014, Determining stellar atmospheric parameters and chemical abundances of FGK stars with iSpec. *Astron. Astrophys.* **569**, A111.

Boisse, I., Eggenberger, A., Santos, N.C., Lovis, C., Bouchy, F., Hébrard, G., Arnold, L., Bonfils, X., Delfosse, X., Desort, M., Díaz, R.F., Ehrenreich, D., Forveille, T., Gallenne, A., Lagrange, A.M., Moutou, C., Udry, S., Pepe, F., Perrier, C., Perruchot, S., Pont, F., Queloz, D., Santerne, A., Ségransan, D., Vidal-Madjar, A.: 2010, The SOPHIE search for northern extrasolar planets. III. A Jupiter-mass companion around HD 109246. *Astron. Astrophys.* **523**, A88.

Bonaca, A., Tanner, J.D., Basu, S., Chaplin, W.J., Metcalfe, T.S., Monteiro, M.J.P.F.G., Ballot, J., Bedding, T.R., Bonanno, A., Broomhall, A.M., Bruntt, H., Campante, T.L., Christensen-Dalsgaard, J., Corsaro, E., Elsworth, Y., García, R.A., Hekker, S., Karoff, C., Kjeldsen, H., Mathur, S., Régulo, C., Roxburgh, I., Stello, D., Trampedach, R., Barclay, T., Burke, C.J., Caldwell, D.A.: 2012, Calibrating Convective Properties of Solar-like Stars in the Kepler Field of View. *Astrophys. J. Lett.* **755**, L12.

Borucki, W.J., Koch, D.G., Lissauer, J., Basri, G., Brown, T., Caldwell, D.A., Jenkins, J.M., Caldwell, J.J., Christensen-Dalsgaard, J., Cochran, W.D., Dunham, E.W., Gautier, T.N., Geary, J.C., Latham, D., Sasselov, D., Gilliland, R.L., Howell, S., Monet, D.G., Batalha, N.: 2007, KEPLER Mission Status. In: Afonso, C., Weldrake, D., Henning, T. (eds.) *Transiting Extrapolar Planets Workshop*, *Astronomical Society of the Pacific Conference Series* **366**, 309.

Borucki, W., Koch, D., Batalha, N., Caldwell, D., Christensen-Dalsgaard, J., Cochran, W.D., Dunham, E., Gautier, T.N., Geary, J., Gilliland, R., Jenkins, J., Kjeldsen, H., Lissauer, J.J., Rowe, J.: 2009, KEPLER: Search for Earth-Size Planets in the Habitable Zone. In: Pont, F., Sasselov, D., Holman, M.J. (eds.) *IAU Symposium*, *IAU Symposium* **253**, 289 – 299.

Bouchy, F., Sophie Team: 2006, SOPHIE: the successor of the spectrograph ELODIE for extrasolar planet search and characterization. In: Arnold, L., Bouchy, F., Moutou, C. (eds.) *Tenth Anniversary of 51 Peg-b: Status of and prospects for hot Jupiter studies*, 319 – 325.

Bouchy, F., Pepe, F., Queloz, D.: 2001, Fundamental photon noise limit to radial velocity measurements. *Astron. Astrophys.* **374**, 733 – 739.

Bouchy, F., Pont, F., Melo, C., Santos, N.C., Mayor, M., Queloz, D., Udry, S.: 2005, Doppler follow-up of OGLE transiting companions in the Galactic bulge. *Astron. Astrophys.* **431**, 1105 – 1121.

Bouchy, F., Bonomo, A.S., Santerne, A., Moutou, C., Deleuil, M., Díaz, R.F., Eggenberger, A., Ehrenreich, D., Gry, C., Guillot, T., Havel, M., Hébrard, G., Udry, S.: 2011a, SOPHIE velocimetry of Kepler transit candidates. III. KOI-423b: an 18 M_{Jup} transiting companion around an F7IV star. *Astron. Astrophys.* **533**, A83.

Bouchy, F., Deleuil, M., Guillot, T., Aigrain, S., Carone, L., Cochran, W.D., Almenara, J.M., Alonso, R., Auvergne, M., Baglin, A., Barge, P., Bonomo, A.S., Bordé, P., Csizmadia, S., de Bondt, K., Deeg, H.J., Díaz, R.F., Dvorak, R., Endl, M., Erikson, A., Ferraz-Mello, S., Fridlund, M., Gandolfi, D., Gazzano, J.C., Gibson, N., Gillon, M., Guenther, E., Hatzes, A., Havel, M., Hébrard, G., Jorda, L., Léger, A., Lovis, C., Llebaria, A., Lammer, H., MacQueen, P.J., Mazeh, T., Moutou, C., Ofir, A., Ollivier, M., Parviainen, H., Pätzold, M., Queloz, D., Rauer, H., Rouan, D., Santerne, A., Schneider, J., Tingley, B., Wuchterl, G.: 2011b, Transiting exoplanets from the CoRoT space mission. XV. CoRoT-15b: a brown-dwarf transiting companion. *Astron. Astrophys.* **525**, A68.

Butler, R.P., Vogt, S.S., Marcy, G.W., Fischer, D.A., Henry, G.W., Apps, K.: 2000, Planetary Companions to the Metal-rich Stars BD -10deg3166 and HD 52265. *Astrophys. J.* **545**, 504 – 511.

Campbell, B., Auman, J., Walker, G., Yang, S.: 1979, Precision Radial Velocities with the Hydrogen Fluoride Absorption Cell. In: *Bulletin of the American Astronomical Society*, *Bulletin of the American Astronomical Society* **11**, 647.

Carroll, B.W., Ostlie, D.A.: 2006, *An introduction to modern astrophysics and cosmology.*

Carter, J.A., Fabrycky, D.C., Ragozzine, D., Holman, M.J., Quinn, S.N., Latham, D.W., Buchhave, L.A., Van Cleve, J., Cochran, W.D., Cote, M.T., Endl, M., Ford, E.B., Haas, M.R., Jenkins, J.M., Koch, D.G., Li, J., Lissauer, J.J., MacQueen, P.J., Middour, C.K., Orosz, J.A., Rowe, J.F., Steffen, J.H., Welsh, W.F.: 2011, KOI-126: A Triply Eclipsing Hierarchical Triple with Two Low-Mass Stars. *Science* **331**, 562.

Casagrande, L., Schönrich, R., Asplund, M., Cassisi, S., Ramírez, I., Meléndez, J., Bensby, T., Feltzing, S.: 2011, New constraints on the chemical evolution of the solar neighbourhood and Galactic disc(s). Improved astrophysical parameters for the Geneva-Copenhagen Survey. *Astron. Astrophys.* **530**, A138.

Catala, C.: 2009, PLATO: PLAnetary Transits and Oscillations of stars. *Experimental Astronomy* **23**, 329 – 356.

Chabrier, G.: 2003, Galactic Stellar and Substellar Initial Mass Function. *Pub. Astron. Soc. Pac.* **115**, 763 – 795.

Chabrier, G., Baraffe, I.: 1997a, Structure and evolution of low-mass stars. *Astron. Astrophys.* **327**, 1039 – 1053.

Chabrier, G., Baraffe, I.: 1997b, Theory of low mass stars, brown dwarfs and extra-solar giant planets. In: Bedding, T.R., Booth, A.J., Davis, J. (eds.) *IAU Symposium*, *IAU Symposium* **189**, 331 – 340.

Chabrier, G., Baraffe, I.: 2000, Theory of Low-Mass Stars and Substellar Objects. *ARA&A* **38**, 337 – 377.

Chabrier, G., Gallardo, J., Baraffe, I.: 2007, Evolution of low-mass star and brown dwarf eclipsing binaries. *Astron. Astrophys.* **472**, L17 – L20.

Chabrier, G., Baraffe, I., Leconte, J., Gallardo, J., Barman, T.: 2009, The mass-radius relationship from solar-type stars to terrestrial planets: a review. In: Stempels, E. (ed.) *15th Cambridge Workshop on Cool Stars, Stellar Systems, and the Sun*, *American Institute of Physics Conference Series* **1094**, 102 – 111.

Chakraborty, A., Richardson, E.H., Mahadevan, S.: 2008, PRL advanced radial-velocity all-sky search (PARAS): an efficient fiber-fed spectrograph for planet searches. In: *Society of Photo-Optical Instrumentation Engineers (SPIE) Conference Series*, *Society of Photo-Optical Instrumentation Engineers (SPIE) Conference Series* **7014**, 4.

Chakraborty, A., Mahadevan, S., Roy, A., Pathan, F.M., Shah, V., Richardson, E.H., Ubale, G., Shah, R.: 2010, First light results from PARAS: the PRL Echelle Spectrograph. In: *Society of Photo-Optical Instrumentation Engineers (SPIE) Conference Series*, *Society of Photo-Optical Instrumentation Engineers (SPIE) Conference Series* **7735**, 4.

Chakraborty, A., Mahadevan, S., Roy, A., Dixit, V., Harvey Richardson, E., Dongre, V., Pathan, F.M., Chaturvedi, P., Shah, V., Ubale, G.P., Anandarao, B.G.: 2014, The PRL Stabilized High-Resolution Echelle Fiber-fed Spectrograph: Instrument Description and First Radial Velocity Results. *Pub. Astron. Soc. Pac.* **126**, 133 – 147.

Chaturvedi, P., Deshpande, R., Dixit, V., Roy, A., Chakraborty, A., Mahadevan, S., Anandarao, B.G., Hebb, L., Janardhan, P.: 2014, Determination of mass and orbital parameters of a low-mass star HD 213597B. *Mon. Not. Roy. Astron. Soc.* **442**, 3737 – 3744.

Christian, D.J., Pollacco, D.L., Clarkson, W.I., Collier Cameron, A., Evans, N., Fitzsimmons, A., Haswell, C.A., Hellier, C., Hodgkin, S.T., Horne, K., Kane, S.R., Keenan, F.P., Lister, T.A., Norton, A.J., Ryans, R., Skillen, I., Street, R.A., West, R.G., Wheatley, P.J.: 2005, Current status of the SuperWASP project. In: Favata, F., Hussain, G.A.J., Battrick, B. (eds.) *13th Cambridge Workshop on Cool Stars, Stellar Systems and the Sun*, *ESA Special Publication* **560**, 475.

Christian, D.J., Pollacco, D.L., Skillen, I., Street, R.A., Keenan, F.P., Clarkson, W.I., Collier Cameron, A., Kane, S.R., Lister, T.A., West, R.G., Enoch, B., Evans, A., Fitzsimmons, A., Haswell, C.A., Hellier, C., Hodgkin, S.T., Horne, K., Irwin, J., Norton, A.J., Osborne, J., Ryans, R., Wheatley, P.J., Wilson, D.M.: 2006, The SuperWASP wide-field exoplanetary transit survey: candidates from fields 23 h < RA < 03 h. *Mon. Not. Roy. Astron. Soc.* **372**, 1117 – 1128.

Clarkson, W.I., Enoch, B., Haswell, C.A., Norton, A.J., Christian, D.J., Collier Cameron, A., Kane, S.R., Horne, K.D., Lister, T.A., Street, R.A., West, R.G., Wilson, D.M., Evans, N., Fitzsimmons, A., Hellier, C., Hodgkin, S.T., Irwin, J., Keenan, F.P., Osborne, J.P., Parley, N.R., Pollacco, D.L., Ryans, R., Skillen, I., Wheatley, P.J.: 2007, SuperWASP-North extrasolar planet candidates between 3^h < RA < 6^h. *Mon. Not. Roy. Astron. Soc.* **381**, 851 – 864.

Collier Cameron, A., Wilson, D.M., West, R.G., Hebb, L., Wang, X.B., Aigrain, S., Bouchy, F., Christian, D.J., Clarkson, W.I., Enoch, B., Esposito, M., Guenther, E., Haswell, C.A., Hébrard, G., Hellier, C., Horne, K., Irwin, J., Kane, S.R., Loeillet, B., Lister, T.A., Maxted, P., Mayor, M., Moutou, C., Parley, N., Pollacco, D., Pont, F., Queloz, D., Ryans, R., Skillen, I., Street, R.A., Udry, S., Wheatley, P.J.: 2007, Efficient identification of exoplanetary transit candidates from SuperWASP light curves. *Mon. Not. Roy. Astron. Soc.* **380**, 1230 – 1244.

Counselman, C.C. III: 1973, Outcomes of Tidal Evolution. *Astrophys. J.* **180**, 307 – 316.

Cox, A.N.: 2000, *Allen's astrophysical quantities.*

Doyle, L.R., Carter, J.A., Fabrycky, D.C., Slawson, R.W., Howell, S.B., Winn, J.N., Orosz, J.A., Prćaronsa, A., Welsh, W.F., Quinn, S.N., Latham, D., Torres, G., Buchhave, L.A., Marcy, G.W., Fortney, J.J., Shporer, A., Ford, E.B., Lissauer, J.J., Ragozzine, D., Rucker, M., Batalha, N., Jenkins, J.M., Borucki, W.J., Koch, D., Middour, C.K., Hall, J.R., McCauliff, S., Fanelli, M.N., Quintana, E.V., Holman, M.J., Caldwell, D.A., Still, M., Stefanik, R.P., Brown, W.R., Esquerdo, G.A., Tang, S., Furesz, G., Geary, J.C., Berlind, P., Calkins, M.L., Short, D.R., Steffen, J.H., Sasselov, D., Dunham, E.W., Cochran, W.D., Boss, A., Haas, M.R., Buzasi, D., Fischer, D.: 2011, Kepler-16: A Transiting Circumbinary Planet. *Science* **333**, 1602.

Dressing, C.D., Charbonneau, D.: 2013, The Occurrence Rate of Small Planets around Small Stars. *Astrophys. J.* **767**, 95.

Duquennoy, A., Mayor, M.: 1991, Multiplicity among solar-type stars in the solar neighbourhood. II - Distribution of the orbital elements in an unbiased sample. *Astron. Astrophys.* **248**, 485 – 524.

Eastman, J., Gaudi, B.S., Agol, E.: 2013, EXOFAST: A Fast Exoplanetary Fitting Suite in IDL. *Pub. Astron. Soc. Pac.* **125**, 83 – 112.

Edvardsson, B., Andersen, J., Gustafsson, B., Lambert, D.L., Nissen, P.E., Tomkin, J.: 1993, The Chemical Evolution of the Galactic Disk - Part One - Analysis and Results. *Astron. Astrophys.* **275**, 101.

Emerson, D.: 1996, *Interpreting Astronomical Spectra*.

Feiden, G.A.: 2015, Eclipsing Binary Systems as Tests of Low-Mass Stellar Evolution Theory. In: Rucinski, S.M., Torres, G., Zejda, M. (eds.) *Living Together: Planets, Host Stars and Binaries*, *Astronomical Society of the Pacific Conference Series* **496**, 137.

Fernandez, J.M., Latham, D.W., Torres, G., Everett, M.E., Mandushev, G., Charbonneau, D., O'Donovan, F.T., Alonso, R., Esquerdo, G.A., Hergenrother, C.W., Stefanik, R.P.: 2009, Mass and Radius Determinations for Five Transiting M-Dwarf Stars. *Astrophys. J.* **701**, 764 – 775.

Fischer, D.A., Marcy, G.W.: 1992, Multiplicity among M dwarfs. *Astrophys. J.* **396**, 178 – 194.

Fleming, T.A., Gioia, I.M., Maccacaro, T.: 1989, The relation between X-ray emission and rotation in late-type stars from the perspective of X-ray selection. *Astrophys. J.* **340**, 1011 – 1023.

Fortier, A., Beck, T., Benz, W., Broeg, C., Cessa, V., Ehrenreich, D., Thomas, N.: 2014, CHEOPS: a space telescope for ultra-high precision photometry of exoplanet transits. In: *Society of Photo-Optical Instrumentation Engineers (SPIE) Conference Series*, *Society of Photo-Optical Instrumentation Engineers (SPIE) Conference Series* **9143**, 2.

Gaudi, B.S., Winn, J.N.: 2007, Prospects for the Characterization and Confirmation of Transiting Exoplanets via the Rossiter-McLaughlin Effect. *Astrophys. J.* **655**, 550 – 563.

Ghezzi, L., Dutra-Ferreira, L., Lorenzo-Oliveira, D., Porto de Mello, G.F., Santiago, B.X., De Lee, N., Lee, B.L., da Costa, L.N., Maia, M.A.G., Ogando, R.L.C., Wisniewski, J.P., González Hernández, J.I., Stassun, K.G., Fleming, S.W., Schneider, D.P., Mahadevan, S., Cargile, P., Ge, J., Pepper, J., Wang, J., Paegert, M.: 2014, Accurate Atmospheric Parameters at Moderate Resolution Using Spectral Indices: Preliminary Application to the MARVELS Survey. *Astron. J.* **148**, 105.

Głębocki, R., Gnaciński, P.: 2005, Systematic errors in the determination of stellar rotational velocities. In: Favata, F., Hussain, G.A.J., Battrick, B. (eds.) *13th Cambridge Workshop on Cool Stars, Stellar Systems and the Sun*, *ESA Special Publication* **560**, 571.

Gómez Maqueo Chew, Y., Faedi, F., Cargile, P., Doyle, A.P., Ghezzi, L., Sousa, S., Barros, S.C.C., Hebb, L., Cunha, K., Schuler, S.C., Smith, V.V., Collier Cameron, A., Pollacco, D., Santos, N.C., Smalley, B., Stassun, K.G.: 2013, The Homogeneous Study of Transiting Systems (HoSTS). I. The Pilot Study of WASP-13. *Astrophys. J.* **768**, 79.

Gómez Maqueo Chew, Y., Morales, J.C., Faedi, F., García-Melendo, E., Hebb, L., Rodler, F., Deshpande, R., Mahadevan, S., McCormac, J., Barnes, R., Triaud, A.H.M.J., Lopez-Morales, M., Skillen, I., Collier Cameron, A., Joner, M.D., Laney, C.D., Stephens, D.C., Stassun, K.G., Cargile, P.A., Montañés-Rodríguez, P.: 2014, The EBLM project. II. A very hot, low-mass M dwarf in an eccentric and long-period, eclipsing binary system from the SuperWASP Survey. *Astron. Astrophys.* **572**, A50.

Gray, D.F.: 1984, Measurements of rotation and turbulence in F, G, and K dwarfs. *Astrophys. J.* **281**, 719 – 722.

Gray, R.O.: 1999, *SPECTRUM: A stellar spectral synthesis program*, Astrophysics Source Code Library.

Grether, D., Lineweaver, C.H.: 2006, How Dry is the Brown Dwarf Desert? Quantifying the Relative Number of Planets, Brown Dwarfs, and Stellar Companions around Nearby Sun-like Stars. *Astrophys. J.* **640**, 1051 – 1062.

Grevesse, N., Sauval, A.J.: 1998, Standard Solar Composition. *Space Sci. Rev.* **85**, 161 – 174.

Grevesse, N., Asplund, M., Sauval, A.J.: 2007, The Solar Chemical Composition. *Space Sci. Rev.* **130**, 105 – 114.

Griffin, R., Griffin, R.: 1973, Accurate wavelengths of stellar and telluric absorption lines near lambda 7000 Angstroms. *Mon. Not. Roy. Astron. Soc.* **162**, 255.

Guinan, E.F., Fitzpatrick, E.L., DeWarf, L.E., Maloney, F.P., Maurone, P.A., Ribas, I., Pritchard, J.D., Bradstreet, D.H., Giménez, A.: 1998, The Distance to the Large Magellanic Cloud from the Eclipsing Binary HV 2274. *Astrophys. J. Lett.* **509**, L21 – L24.

Hart, M.H.: 1978, The evolution of the atmosphere of the earth. *Icarus* **33**, 23 – 39.

Hartman, J.D., Bakos, G.Á., Noyes, R.W., Sipőcz, B., Kovács, G., Mazeh, T., Shporer, A., Pál, A.: 2011, A Photometric Variability Survey of Field K and M Dwarf Stars with HATNet. *Astron. J.* **141**, 166.

Haswell, C.A.: 2010, *Transiting Exoplanets*.

Hatzes, A.P., Cochran, W.D.: 1992, Spectrograph Requirements for Precise Radial Velocity Measurements. In: Ulrich, M.H. (ed.) *European Southern Observatory Conference and Workshop Proceedings*, *European Southern Observatory Conference and Workshop Proceedings* **40**, 275.

Hayashi, C., Nakano, T.: 1963, Evolution of Stars of Small Masses in the Pre-Main-Sequence Stages. *Progress of Theoretical Physics* **30**, 460 – 474.

Herschel, W.: 1802, Catalogue of 500 New Nebulae, Nebulous Stars, Planetary Nebulae, and Clusters of Stars; With Remarks on the Construction of the Heavens. *Philosophical Transactions of the Royal Society of London Series I* **92**, 477 – 528.

Horch, E.P., Howell, S.B., Everett, M.E., Ciardi, D.R.: 2014, Most Subarcsecond Companions of Kepler Exoplanet Candidate Host Stars are Gravitationally Bound. *Astrophys. J.* **795**, 60.

Howell, S.B., Sobeck, C., Haas, M., Still, M., Barclay, T., Mullally, F., Troeltzsch, J., Aigrain, S., Bryson, S.T., Caldwell, D., Chaplin, W.J., Cochran, W.D., Huber, D., Marcy, G.W., Miglio, A., Najita, J.R., Smith, M., Twicken, J.D., Fortney, J.J.: 2014, The K2 Mission: Characterization and Early Results. *Pub. Astron. Soc. Pac.* **126**, 398 – 408.

Huber, D., Chaplin, W.J., Christensen-Dalsgaard, J., Gilliland, R.L., Kjeldsen, H., Buchhave, L.A., Fischer, D.A., Lissauer, J.J., Rowe, J.F., Sanchis-Ojeda, R., Basu, S., Handberg, R., Hekker, S., Howard, A.W., Isaacson, H., Karoff, C., Latham, D.W., Lund, M.N., Lundkvist, M., Marcy, G.W., Miglio, A., Silva Aguirre, V., Stello, D., Arentoft, T., Barclay, T., Bedding, T.R., Burke, C.J., Christiansen, J.L., Elsworth, Y.P., Haas, M.R., Kawaler, S.D., Metcalfe, T.S., Mullally, F., Thompson, S.E.: 2013, Fundamental Properties of Kepler Planet-candidate Host Stars using Asteroseismology. *Astrophys. J.* **767**, 127.

Hut, P.: 1981, Tidal evolution in close binary systems. *Astron. Astrophys.* **99**, 126 – 140.

Irwin, J.M., Quinn, S.N., Berta, Z.K., Latham, D.W., Torres, G., Burke, C.J., Charbonneau, D., Dittmann, J., Esquerdo, G.A., Stefanik, R.P., Oksanen, A., Buchhave, L.A., Nutzman, P., Berlind, P., Calkins, M.L., Falco, E.E.: 2011, LSPM J1112+7626: Detection of a 41 Day M-dwarf Eclipsing Binary from the MEarth Transit Survey. *Astrophys. J.* **742**, 123.

Irwin, J., Charbonneau, D., Berta, Z.K., Quinn, S.N., Latham, D.W., Torres, G., Blake, C.H., Burke, C.J., Esquerdo, G.A., Fürész, G., Mink, D.J., Nutzman, P., Szentgyorgyi, A.H., Calkins, M.L., Falco, E.E., Bloom, J.S., Starr, D.L.: 2009, GJ 3236: A New Bright, Very Low Mass Eclipsing Binary System Discovered by the MEARTH Observatory. *Astrophys. J.* **701**, 1436 – 1449.

Johnson, J.A., Marcy, G.W., Fischer, D.A., Henry, G.W., Wright, J.T., Isaacson, H., McCarthy, C.: 2006, An Eccentric Hot Jupiter Orbiting the Subgiant HD 185269. *Astrophys. J.* **652**, 1724 – 1728.

Johnson, J.A., Payne, M., Howard, A.W., Clubb, K.I., Ford, E.B., Bowler, B.P., Henry, G.W., Fischer, D.A., Marcy, G.W., Brewer, J.M., Schwab, C., Reffert, S., Lowe, T.B.: 2011, Retired A Stars and Their Companions. VI. A Pair of Interacting Exoplanet Pairs Around the Subgiants 24 Sextanis and HD 200964. *Astron. J.* **141**, 16.

Kallrath, J., Milone, E.F.: 2000, Book Review: Eclipsing binary stars : modelling and analysis. *The Observatory, Springer* **120**, 150.

Kane, S.R., Clarkson, W.I., West, R.G., Wilson, D.M., Christian, D.J., Collier Cameron, A., Enoch, B., Lister, T.A., Street, R.A., Evans, A., Fitzsimmons, A., Haswell, C.A., Hellier, C., Hodgkin, S.T., Horne, K., Irwin, J., Keenan, F.P., Norton, A.J., Osborne, J., Parley, N.R., Pollacco, D.L., Ryans, R., Skillen, I., Wheatley, P.J.: 2008, SuperWASP-N extrasolar planet candidates from fields $06^h < \mathrm{RA} < 16^h$. *Mon. Not. Roy. Astron. Soc.* **384**, 1097 – 1108.

Kirkpatrick, J.D.: 2005, New Spectral Types L and T. *ARA&A* **43**, 195 – 245.

Koch, D., Borucki, W., Basri, G., Brown, T., Caldwell, D., Christensen-Dalsgaard, J., Cochran, W., Devore, E., Dunham, E., Gautier, T.N., Geary, J., Gilliland, R., Gould, A., Jenkins, J., Kondo, Y., Latham, D., Lissauer, J., Monet, D.: 2007, The Kepler Mission and Eclipsing Binaries. In: Hartkopf, W.I., Harmanec, P., Guinan, E.F. (eds.) *IAU Symposium*, *IAU Symposium* **240**, 236 – 243.

Kopparapu, R.K., Ramirez, R.M., SchottelKotte, J., Kasting, J.F., Domagal-Goldman, S., Eymet, V.: 2014, Habitable Zones around Main-sequence Stars: Dependence on Planetary Mass. *Astrophys. J. Lett.* **787**, L29.

Kraus, A.L., Tucker, R.A., Thompson, M.I., Craine, E.R., Hillenbrand, L.A.: 2011, The Mass-Radius(-Rotation?) Relation for Low-mass Stars. *Astrophys. J.* **728**, 48.

Kuiper, G.P.: 1938, The Empirical Mass-Luminosity Relation. *Astrophys. J.* **88**, 472.

Kumar, S.S.: 1963, The Structure of Stars of Very Low Mass. *Astrophys. J.* **137**, 1121.

Kurucz, R.: 1993, ATLAS9 Stellar Atmosphere Programs and 2 km/s grid. *ATLAS9 Stellar Atmosphere Programs and 2 km/s grid. Kurucz CD-ROM No. 13. Cambridge, Mass.: Smithsonian Astrophysical Observatory, 1993.* **13**.

Lacy, C.H.S., Claret, A., Sabby, J.A., Hood, B., Secosan, F.: 2004, Absolute Properties of the Eclipsing Binary Star V396 Cassiopeiae. *Astron. J.* **128**, 3005 – 3011.

Larson, R.B.: 2001, Implications of Binary Properties for Theories of Star Formation. In: Zinnecker, H.Mathieu, R. (eds.) *The Formation of Binary Stars*, *IAU Symposium* **200**, 93.

Lister, T.A., West, R.G., Wilson, D.M., Collier Cameron, A., Clarkson, W.I., Street, R.A., Enoch, B., Parley, N.R., Christian, D.J., Kane, S.R., Evans, A., Fitzsimmons, A., Haswell, C.A., Hellier, C., Hodgkin, S.T., Horne, K., Irwin, J., Keenan, F.P., Norton, A.J., Osborne, J., Pollacco, D.L., Ryans, R., Skillen, I., Wheatley, P.J., Barnes, J.R.: 2007, SuperWASP-North extrasolar planet candidates: candidates from fields 17h<RA<18h. *Mon. Not. Roy. Astron. Soc.* **379**, 647 – 662.

López-Morales, M.: 2007, On the Correlation between the Magnetic Activity Levels, Metallicities, and Radii of Low-Mass Stars. *Astrophys. J.* **660**, 732 – 739.

López-Morales, M., Ribas, I.: 2005, GU Bootis: A New 0.6 M_{solar} Detached Eclipsing Binary. *Astrophys. J.* **631**, 1120 – 1133.

Lovis, C., Pepe, F.: 2007, A new list of thorium and argon spectral lines in the visible. *Astron. Astrophys.* **468**, 1115 – 1121.

Lovis, C., Pepe, F., Bouchy, F., Lo Curto, G., Mayor, M., Pasquini, L., Queloz, D., Rupprecht, G., Udry, S., Zucker, S.: 2006, The exoplanet hunter HARPS: unequalled accuracy and perspectives toward 1 cm s $^{-1}$ precision. In: *Society of Photo-Optical Instrumentation Engineers (SPIE) Conference Series*, *Society of Photo-Optical Instrumentation Engineers (SPIE) Conference Series* **6269**, 0.

Malkov, O.Y., Oblak, E., Snegireva, E.A., Torra, J.: 2006, A catalogue of eclipsing variables. *Astron. Astrophys.* **446**, 785 – 789.

Mandel, K., Agol, E.: 2002, Analytic Light Curves for Planetary Transit Searches. *Astrophys. J. Lett.* **580**, L171 – L175.

Marcy, G.W., Butler, R.P.: 2000, Planets Orbiting Other Suns. *Pub. Astron. Soc. Pac.* **112**, 137 – 140.

Markwardt, C.B.: 2009, Non-linear Least-squares Fitting in IDL with MP-FIT. In: Bohlender, D.A., Durand, D., Dowler, P. (eds.) *Astronomical Data Analysis Software and Systems XVIII*, *Astronomical Society of the Pacific Conference Series* **411**, 251.

Masana, E., Jordi, C., Ribas, I.: 2006, Effective temperature scale and bolometric corrections from 2MASS photometry. *Astron. Astrophys.* **450**, 735–746.

Mason, J.W.: 2008, *Exoplanets.*

Mazeh, T.: 2008, Observational Evidence for Tidal Interaction in Close Binary Systems. In: Goupil, M.J.Zahn, J.P. (eds.) *EAS Publications Series*, *EAS Publications Series* **29**, 1–65.

McDonald, I., Zijlstra, A.A., Boyer, M.L.: 2012, Fundamental parameters and infrared excesses of Hipparcos stars. *Mon. Not. Roy. Astron. Soc.* **427**, 343–357.

Meibom, S., Barnes, S.A., Platais, I., Gilliland, R.L., Latham, D.W., Mathieu, R.D.: 2015, A spin-down clock for cool stars from observations of a 2.5-billion-year-old cluster. *Nature* **517**, 589–591.

Mera, D., Chabrier, G., Baraffe, I.: 1996, Determination of the Low-Mass Star Mass Function in the Galactic Disk. *Astrophys. J. Lett.* **459**, L87.

Morales, J.C., Ribas, I., Jordi, C., Torres, G., Gallardo, J., Guinan, E.F., Charbonneau, D., Wolf, M., Latham, D.W., Anglada-Escudé, G., Bradstreet, D.H., Everett, M.E., O'Donovan, F.T., Mandushev, G., Mathieu, R.D.: 2009, Absolute Properties of the Low-Mass Eclipsing Binary CM Draconis. *Astrophys. J.* **691**, 1400–1411.

Mortier, A., Sousa, S.G., Adibekyan, V.Z., Brandão, I.M., Santos, N.C.: 2014, Correcting the spectroscopic surface gravity using transits and asteroseismology. No significant effect on temperatures or metallicities with ARES and MOOG in local thermodynamic equilibrium. *Astron. Astrophys.* **572**, A95.

Mullan, D.J., MacDonald, J.: 2001, Are Magnetically Active Low-Mass M Dwarfs Completely Convective? *Astrophys. J.* **559**, 353–371.

Nakajima, T., Oppenheimer, B.R., Kulkarni, S.R., Golimowski, D.A., Matthews, K., Durrance, S.T.: 1995, Discovery of a cool brown dwarf. *Nature* **378**, 463 – 465.

Nefs, S.V., Birkby, J.L., Snellen, I.A.G., Hodgkin, S.T., Sipőcz, B.M., Kovács, G., Mislis, D., Pinfield, D.J., Martin, E.L.: 2013, A highly unequal-mass eclipsing M-dwarf binary in the WFCAM Transit Survey. *Mon. Not. Roy. Astron. Soc.* **431**, 3240 – 3257.

Nordstrom, B., Stefanik, R.P., Latham, D.W., Andersen, J.: 1997, Radial velocities, rotations, and duplicity of a sample of early F-type dwarfs. *Astron. Astrophys. Suppl.* **126**, 21 – 30.

Nordström, B., Mayor, M., Andersen, J., Holmberg, J., Pont, F., Jørgensen, B.R., Olsen, E.H., Udry, S., Mowlavi, N.: 2004, The Geneva-Copenhagen survey of the Solar neighbourhood. Ages, metallicities, and kinematic properties of 14 000 F and G dwarfs. *Astron. Astrophys.* **418**, 989 – 1019.

Ofir, A., Gandolfi, D., Buchhave, L., Lacy, C.H.S., Hatzes, A.P., Fridlund, M.: 2012, KIC 1571511B: a benchmark low-mass star in an eclipsing binary system in the Kepler field. *Mon. Not. Roy. Astron. Soc.* **423**, L1 – L5.

Paletou, F., Gebran, M., Houdebine, E.R., Watson, V.: 2015, Principal component analysis-based inversion of effective temperatures for late-type stars. *Astron. Astrophys.* **580**, A78.

Pecaut, M.J., Mamajek, E.E.: 2013, Intrinsic Colors, Temperatures, and Bolometric Corrections of Pre-main-sequence Stars. *Astrophys. J. Supplement.* **208**, 9.

Pepe, F., Mayor, M., Galland, F., Naef, D., Queloz, D., Santos, N.C., Udry, S., Burnet, M.: 2002, The CORALIE survey for southern extra-solar planets VII. Two short-period Saturnian companions to HD 108147 and HD 168746. *Astron. Astrophys.* **388**, 632 – 638.

Pepe, F., Rupprecht, G., Avila, G., Balestra, A., Bouchy, F., Cavadore, C., Eckert, W., Fleury, M., Gillotte, A., Gojak, D., Guzman, J.C., Kohler, D., Lizon, J.L., Mayor, M., Megevand, D., Queloz, D., Sosnowska, D., Udry, S., Weilenmann, U.: 2003, Performance verification of HARPS: first laboratory results. In: Iye, M.Moorwood, A.F.M. (eds.) *Instrument Design and Performance for Optical/Infrared Ground-based Telescopes*, *Society of Photo-Optical Instrumentation Engineers (SPIE) Conference Series* **4841**, 1045 – 1056.

Pietrzyński, G., Thompson, I.B., Graczyk, D., Gieren, W., Udalski, A., Szewczyk, O., Minniti, D., Kołaczkowski, Z., Bresolin, F., Kudritzki, R.P.: 2009, The Araucaria Project. Determination of the Large Magellanic Cloud Distance from Late-Type Eclipsing Binary Systems. I. OGLE-051019.64-685812.3. *Astrophys. J.* **697**, 862 – 866.

Piskunov, N.E., Valenti, J.A.: 2002, New algorithms for reducing cross-dispersed echelle spectra. *Astron. Astrophys.* **385**, 1095 – 1106.

Pollacco, D.L., Skillen, I., Collier Cameron, A., Christian, D.J., Hellier, C., Irwin, J., Lister, T.A., Street, R.A., West, R.G., Anderson, D.R., Clarkson, W.I., Deeg, H., Enoch, B., Evans, A., Fitzsimmons, A., Haswell, C.A., Hodgkin, S., Horne, K., Kane, S.R., Keenan, F.P., Maxted, P.F.L., Norton, A.J., Osborne, J., Parley, N.R., Ryans, R.S.I., Smalley, B., Wheatley, P.J., Wilson, D.M.: 2006, The WASP Project and the SuperWASP Cameras. *Pub. Astron. Soc. Pac.* **118**, 1407 – 1418.

Pont, F., Melo, C.H.F., Bouchy, F., Udry, S., Queloz, D., Mayor, M., Santos, N.C.: 2005a, A planet-sized transiting star around OGLE-TR-122. Accurate mass and radius near the hydrogen-burning limit. *Astron. Astrophys.* **433**, L21 – L24.

Pont, F., Bouchy, F., Melo, C., Santos, N.C., Mayor, M., Queloz, D., Udry, S.: 2005b, Doppler follow-up of OGLE planetary transit candidates in Carina. *Astron. Astrophys.* **438**, 1123 – 1140.

Pont, F., Moutou, C., Bouchy, F., Behrend, R., Mayor, M., Udry, S., Queloz, D., Santos, N., Melo, C.: 2006, Radius and mass of a transiting M dwarf near the hydrogen-burning limit. OGLE-TR-123. *Astron. Astrophys.* **447**, 1035 – 1039.

Popper, D.M.: 1974, Rediscussion of eclipsing binaries. X. The B stars AG Persei and CW Cephei. *Astrophys. J.* **188**, 559 – 565.

Popper, D.M., Tomkin, J.: 1984, S CANCRI - A semidetached system with a very low-mass secondary. *Astrophys. J.* **285**, 208 – 213.

Press, W.H., Teukolsky, S.A., Vetterling, W.T., Flannery, B.P.: 1992, *Numerical recipes in C. The art of scientific computing.*

Ramsey, L.W., Adams, M.T., Barnes, T.G., Booth, J.A., Cornell, M.E., Fowler, J.R., Gaffney, N.I., Glaspey, J.W., Good, J.M., Hill, G.J., Kelton, P.W., Krabbendam, V.L., Long, L., MacQueen, P.J., Ray, F.B., Ricklefs, R.L., Sage, J., Sebring, T.A., Spiesman, W.J., Steiner, M.: 1998, Early performance and present status of the Hobby-Eberly Telescope. In: Stepp, L.M. (ed.) *Advanced Technology Optical/IR Telescopes VI*, *Society of Photo-Optical Instrumentation Engineers (SPIE) Conference Series* **3352**, 34 – 42.

Rasio, F.A.: 1995, The minimum mass ratio of W Ursae Majoris binaries. *Astrophys. J. Lett.* **444**, L41 – L43.

Ribas, I.: 2003, The 0.4-M_{sun} eclipsing binary CU Cancri. Absolute dimensions, comparison with evolutionary models and possible evidence for a circumstellar dust disk. *Astron. Astrophys.* **398**, 239 – 251.

Ribas, I., Jordi, C., Torra, J.: 1999, CD Tau: a detached eclipsing binary with a solar-mass companion. *Mon. Not. Roy. Astron. Soc.* **309**, 199 – 207.

Ribas, I., Jordi, C., Vilardell, F., Fitzpatrick, E.L., Hilditch, R.W., Guinan, E.F.: 2005, First Determination of the Distance and Fundamental Properties of an Eclipsing Binary in the Andromeda Galaxy. *Astrophys. J. Lett.* **635**, L37 – L40.

Ribas, I., Morales, J.C., Jordi, C., Baraffe, I., Chabrier, G., Gallardo, J.: 2008, Fundamental properties of low-mass stars. *Memorie della Societa Astronomica Italiana* **79**, 562.

Ricker, G.R., Winn, J.N., Vanderspek, R., Latham, D.W., Bakos, G.Á., Bean, J.L., Berta-Thompson, Z.K., Brown, T.M., Buchhave, L., Butler, N.R., Butler, R.P., Chaplin, W.J., Charbonneau, D., Christensen-Dalsgaard, J., Clampin, M., Deming, D., Doty, J., De Lee, N., Dressing, C., Dunham, E.W., Endl, M., Fressin, F., Ge, J., Henning, T., Holman, M.J., Howard, A.W., Ida, S., Jenkins, J.M., Jernigan, G., Johnson, J.A., Kaltenegger, L., Kawai, N., Kjeldsen, H., Laughlin, G., Levine, A.M., Lin, D., Lissauer, J.J., MacQueen, P., Marcy, G., McCullough, P.R., Morton, T.D., Narita, N., Paegert, M., Palle, E., Pepe, F., Pepper, J., Quirrenbach, A., Rinehart, S.A., Sasselov, D., Sato, B., Seager, S., Sozzetti, A., Stassun, K.G., Sullivan, P., Szentgyorgyi, A., Torres, G., Udry, S., Villasenor, J.: 2015, Transiting Exoplanet Survey Satellite (TESS). *Journal of Astronomical Telescopes, Instruments, and Systems* **1**(1), 014003.

Salpeter, E.E.: 1955, The Luminosity Function and Stellar Evolution. *Astrophys. J.* **121**, 161.

Sangaralingam, V., Stevens, I.R.: 2011, STEREO TRansiting Exoplanet and Stellar Survey (STRESS) - I. Introduction and data pipeline. *Mon. Not. Roy. Astron. Soc.* **418**, 1325 – 1334.

Seager, S.: 2010, *Exoplanets*.

Smalley, B.: 2005, T_{eff} and log g determinations. *Memorie della Societa Astronomica Italiana Supplementi* **8**, 130.

Soubiran, C., Le Campion, J.F., Cayrel de Strobel, G., Caillo, A.: 2010, The PASTEL catalogue of stellar parameters. *Astron. Astrophys.* **515**, A111.

Sousa, S.G., Santos, N.C., Adibekyan, V., Delgado-Mena, E., Tabernero, H.M., González Hernández, J.I., Montes, D., Smiljanic, R., Korn, A.J., Bergemann, M., Soubiran, C., Mikolaitis, S.: 2014, A new procedure for defining a homogenous line-list for solar-type stars. *Astron. Astrophys.* **561**, A21.

Southworth, J., Clausen, J.V.: 2007, Absolute dimensions of eclipsing binaries. XXIV. The Be star system DW Carinae, a member of the open cluster Collinder 228. *Astron. Astrophys.* **461**, 1077 – 1093.

Stempels, H.C., Collier Cameron, A., Hebb, L., Smalley, B., Frandsen, S.: 2007, WASP-1: a lithium- and metal-rich star with an oversized planet. *Mon. Not. Roy. Astron. Soc.* **379**, 773 – 778.

Strassmeier, K.G.: 2009, Starspots. *Astron. Astrophys. Rev.* **17**, 251 – 308.

Street, R.A., Pollaco, D.L., Fitzsimmons, A., Keenan, F.P., Horne, K., Kane, S., Collier Cameron, A., Lister, T.A., Haswell, C., Norton, A.J., Jones, B.W., Skillen, I., Hodgkin, S., Wheatley, P., West, R., Brett, D.: 2003, SuperWASP: Wide Angle Search for Planets. In: Deming, D.Seager, S. (eds.) *Scientific Frontiers in Research on Extrasolar Planets*, *Astronomical Society of the Pacific Conference Series* **294**, 405 – 408.

Street, R.A., Christian, D.J., Clarkson, W.I., Collier Cameron, A., Enoch, B., Kane, S.R., Lister, T.A., West, R.G., Wilson, D.M., Evans, A., Fitzsimmons, A., Haswell, C.A., Hellier, C., Hodgkin, S.T., Horne, K., Irwin, J., Keenan, F.P., Norton, A.J., Osborne, J., Pollacco, D.L., Ryans, R., Skillen, I., Wheatley, P.J., Barnes, J.: 2007, SuperWASP-N extrasolar planet candidates between $18 < \mathrm{RA} < 21\mathrm{h}$. *Mon. Not. Roy. Astron. Soc.* **379**, 816 – 832.

Swam, M.S., Swade, D., Sontag, C., Heller-Boyer, C., Gaffney, N., Kidwell, R.: 2007, Data Processing and Archiving Software for the Kepler Mission. In: Shaw, R.A., Hill, F., Bell, D.J. (eds.) *Astronomical Data Analysis Software and Systems XVI*, *Astronomical Society of the Pacific Conference Series* **376**, 209.

Tal-Or, L., Mazeh, T., Alonso, R., Bouchy, F., Cabrera, J., Deeg, H.J., Deleuil, M., Faigler, S., Fridlund, M., Hébrard, G., Moutou, C., Santerne, A., Tingley, B.: 2013, CoRoT 101186644: A transiting low-mass dense M-dwarf on an eccentric 20.7-day period orbit around a late F-star. Discovered in the CoRoT lightcurves. *Astron. Astrophys.* **553**, A30.

Torres, G., Ribas, I.: 2002, Absolute Dimensions of the M-Type Eclipsing Binary YY Geminorum (Castor C): A Challenge to Evolutionary Models in the Lower Main Sequence. *Astrophys. J.* **567**, 1140 – 1165.

Torres, G., Andersen, J., Giménez, A.: 2010, Accurate masses and radii of normal stars: modern results and applications. *Astron. Astrophys. Rev.* **18**, 67 – 126.

Torres, G., Andersen, J., Nordström, B., Latham, D.W.: 2000, Absolute Dimensions of Eclipsing Binaries. XXIII. The F-Type System EI Cephei. *Astron. J.* **119**, 1942 – 1955.

Torres, G., Fischer, D.A., Sozzetti, A., Buchhave, L.A., Winn, J.N., Holman, M.J., Carter, J.A.: 2012, Improved Spectroscopic Parameters for Transiting Planet Hosts. *Astrophys. J.* **757**, 161.

Triaud, A.H.M.J., Hebb, L., Anderson, D.R., Cargile, P., Collier Cameron, A., Doyle, A.P., Faedi, F., Gillon, M., Gomez Maqueo Chew, Y., Hellier, C., Jehin, E., Maxted, P., Naef, D., Pepe, F., Pollacco, D., Queloz, D., Ségransan, D., Smalley, B., Stassun, K., Udry, S., West, R.G.: 2013, The EBLM project. I. Physical and orbital parameters, including spin-orbit angles, of two low-mass eclipsing binaries on opposite sides of the brown dwarf limit. *Astron. Astrophys.* **549**, A18.

Tull, R.G.: 1998, High-resolution fiber-coupled spectrograph of the Hobby-Eberly Telescope. In: D'Odorico, S. (ed.) *Optical Astronomical Instrumentation*, *Society of Photo-Optical Instrumentation Engineers (SPIE) Conference Series* **3355**, 387 – 398.

Udry, S., Mayor, M., Queloz, D., Naef, D., Santos, N.: 2000, The CORALIE Planet-Search Sample. In: Bergeron, J.Renzini, A. (eds.) *From Extrasolar Planets to Cosmology: The VLT Opening Symposium*, 571.

Vaccaro, T.R., Rudkin, M., Kawka, A., Vennes, S., Oswalt, T.D., Silver, I., Wood, M., Smith, J.A.: 2007, LP 133-373: A New Chromospherically Active Eclipsing dMe Binary with a Distant, Cool White Dwarf Companion. *Astrophys. J.* **661**, 1112 – 1118.

Valenti, J.A., Fischer, D.A.: 2005, Spectroscopic Properties of Cool Stars (SPOCS). I. 1040 F, G, and K Dwarfs from Keck, Lick, and AAT Planet Search Programs. *Astrophys. J. Supplement.* **159**, 141 – 166.

Valenti, J.A., Piskunov, N.: 1996, Spectroscopy made easy: A new tool for fitting observations with synthetic spectra. *Astron. Astrophys. Suppl.* **118**, 595 – 603.

Valenti, J.A., Butler, R.P., Marcy, G.W.: 1995, Determining Spectrometer Instrumental Profiles Using FTS Reference Spectra. *Pub. Astron. Soc. Pac.* **107**, 966.

Vaz, L.P.R., Cunha, N.C.S., Vieira, E.F., Myrrha, M.L.M.: 1997, V 3903 Sagittarii: a massive main-sequence (O7V+O9V) detached eclipsing binary. *Astron. Astrophys.* **327**, 1094 – 1106.

Wang, X. Sharon, Wright, J.T., Cochran, W., Kane, S.R., Henry, G.W., Payne, M.J., Endl, M., MacQueen, P.J., Valenti, J.A., Antoci, V., Dragomir, D., Matthews, J.M., Howard, A.W., Marcy, G.W., Isaacson, H., Ford, E.B., Mahadevan, S., von Braun, K.: 2012, The Discovery of HD 37605c and a Dispositive Null Detection of Transits of HD 37605b. *Astrophys. J.* **761**, 46.

West, R.G., Collier Cameron, A., Hebb, L., Joshi, Y.C., Pollacco, D., Simpson, E., Skillen, I., Stempels, H.C., Wheatley, P.J., Wilson, D., Anderson, D., Bentley, S., Bouchy, F., Christian, D., Enoch, B., Gibson, N., Hébrard, G., Hellier, C., Loeillet, B., Mayor, M., Maxted, P., McDonald, I., Moutou, C., Pont, F., Queloz, D., Smith, A.M.S., Smalley, B., Street, R.A., Udry, S.: 2009, The sub-Jupiter mass transiting exoplanet WASP-11b. *Astron. Astrophys.* **502**, 395 – 400.

Whittaker, G.N., Stevens, I.R., Sangaralingam, V.: 2013, STEREO trend removal pipeline and planet detection possibilities. *Mon. Not. Roy. Astron. Soc.* **431**, 3456 – 3469.

Wilson, R.E.: 1979, Eccentric orbit generalization and simultaneous solution of binary star light and velocity curves. *Astrophys. J.* **234**, 1054 – 1066.

Wisniewski, J.P., Ge, J., Crepp, J.R., De Lee, N., Eastman, J., Esposito, M., Fleming, S.W., Gaudi, B.S., Ghezzi, L., Gonzalez Hernandez, J.I., Lee, B.L., Stassun, K.G., Agol, E., Allende Prieto, C., Barnes, R., Bizyaev, D., Cargile, P., Chang, L., Da Costa, L.N., Porto De Mello, G.F., Femenía, B., Ferreira, L.D., Gary, B., Hebb, L., Holtzman, J., Liu, J., Ma, B., Mack, C.E., Mahadevan, S., Maia, M.A.G., Nguyen, D.C., Ogando, R.L.C., Oravetz, D.J., Paegert, M., Pan, K., Pepper, J., Rebolo, R., Santiago, B., Schneider, D.P., Shelden, A.C., Simmons, A., Tofflemire, B.M., Wan, X., Wang, J., Zhao, B.: 2012, Very Low Mass Stellar and Substellar Companions to Solar-like Stars from MARVELS. I. A Low-mass Ratio Stellar Companion to TYC 4110-01037-1 in a 79 Day Orbit. *Astron. J.* **143**, 107.

Wraight, K.T., White, G.J., Bewsher, D., Norton, A.J.: 2011, STEREO observations of stars and the search for exoplanets. *Mon. Not. Roy. Astron. Soc.* **416**, 2477 – 2493.

Wraight, K.T., Fossati, L., White, G.J., Norton, A.J., Bewsher, D.: 2012, Bright low mass eclipsing binary candidates observed by STEREO. *Mon. Not. Roy. Astron. Soc.* **427**, 2298 – 2307.

Wright, J.T., Marcy, G.W., Butler, R.P., Vogt, S.S., Henry, G.W., Isaacson, H., Howard, A.W.: 2008, The Jupiter Twin HD 154345b. *Astrophys. J. Lett.* **683**, L63 – L66.

Zahn, J.P.: 1977, Tidal friction in close binary stars. *Astron. Astrophys.* **57**, 383 – 394.

Zucker, S.: 2003, Cross-correlation and maximum-likelihood analysis: a new approach to combining cross-correlation functions. *Mon. Not. Roy. Astron. Soc.* **342**, 1291 – 1298.

List of Publications

A. Refereed journals

1. **“The PRL Stabilized High-Resolution Echelle Fiber-fed Spectrograph: Instrument Description and First Radial Velocity Results”**

   Chakraborty, A. Mahadevan, S. Roy, A.; Dixit, V.;, Richardson, E. H.; Dongre, V.; Pathan, F. M. **Chaturvedi, P.**; Shah, V.; Ubale, G. P.; Anandarao, B. G.

   2014, Publications of the Astronomical Society of the Pacific, 126, 133

2. **“Determination of mass and orbital parameters of a low-mass star HD 213597B”**

   Chaturvedi, P.; , Deshpande, R.; Dixit, V.; Roy A.; Chakraborty, A.; Mahadevan, S.; Anandarao, B. G., Hebb, L.; Janardhan, P.

   2014, Monthly Notices of Royal Astronomical Society, 442, 3737

3. **“World beyond our Own”**

   Chaturvedi, P.; Singal, A.

   2014, Planex Newsletter, Vol.4, Issue 4, 14

B. Conference Proceedings

1. **Precision radial-velocity measurements on bright Sun-like stars**

   Dixit, V; **Chaturvedi, P**; Chakraborty, Abhijit; Mahadevan, S; Roy, A; Dongre, V

   2013, Astronomical Society of India Conference Series − 9

C. Communicated

1. **"Detection of a very low mass star in an Eclipsing Binary system"**
   Chaturvedi, P.; Chakraborty, A.; Anandarao, B. G.; Roy A.; Mahadevan, S.
   2015, Monthly Notices of Royal Astronomical Society, under revision

D. Under preparation

1. **"Detection of two mid M-dwarfs in F+M Eclipsing Binary systems from PARAS"**
   Chaturvedi, P.; Chakraborty, A.; Anandarao, B. G.
   under preparation

E. Presentations at Conferences and Symposia

1. Group Seminar on 'Low mass stars in Eclipsing Binary systems' on 5th July 2015 at MPE, Garching, Germany

2. Group Seminar on 'Low mass stars in Eclipsing Binary systems' on 01 July 2015 at Observatory de Meudon, Paris, France.

3. Presented a poster on 'Study of low mass stars in eclipsing binary systems by Radial velocity with PARAS' at a conference at IAP, Paris, France between 29th June to 3rd July 2015.

4. Planet Seminar on 'Eclipsing Binary Stars by PARAS Spectrograph' at Observatory de Geneva, Geneva, Switzerland on 26th June 2015

5. Contributed talk on 'Low Mass Stars in Eclipsing Binaries' on 26 November 2014 at Near Infra Red Workshop, TIFR, Hyderabad.

6. Contributed talk on 'Low Mass Stars in Eclipsing Binaries' on 22 August 2014 at APRIM meeting, Daejeon, South Korea.'

7. Contributed Oral presentation on ‘Orbital parameters of low mass stars in Eclipsing Binary systems’ at IISER-Mohali at the Astronomical Society of India (ASI) Meet on 21 March 2014.

8. Presented a poster on ‘Precision Radial-Velocity Measurements on bright Sun-like stars’ at ASI 2013 Meeting held at Trivandrum on 20 February 2013.

Publications attached with Thesis

1. **"Determination of mass and orbital parameters of a low-mass star HD 213597B"**
   Chaturvedi, P.; , Deshpande, R.; Dixit, V.; Roy A.; Chakraborty, A.; Mahadevan, S.; Anandarao, B. G., Hebb, L.; Janardhan, P.
   2014, Monthly Notices of Royal Astronomical Society, 442, 3737

Monthly Notices
of the
ROYAL ASTRONOMICAL SOCIETY

MNRAS **442,** 3737–3744 (2014) doi:10.1093/mnras/stu1127

Determination of mass and orbital parameters of a low-mass star HD 213597B

Priyanka Chaturvedi,[1⋆] Rohit Deshpande,[2,3] Vaibhav Dixit,[1] Arpita Roy,[2,3] Abhijit Chakraborty,[1] Suvrath Mahadevan,[2,3] B. G. Anandarao,[1] Leslie Hebb[4] and P. Janardhan[1]

[1] *Astronomy and Astrophysics Division, Physical Research Laboratory, Ahmedabad 380009, India*
[2] *Department of Astronomy and Astrophysics, Pennsylvania State University, University Park, PA 16802, USA*
[3] *Center for Exoplanets and Habitable Worlds, The Pennsylvania State University, University Park, PA 16802, USA*
[4] *Department of Physics, Hobart and William Smith Colleges, Geneva, NY 14456, USA*

Accepted 2014 June 5. Received 2014 June 5; in original form 2013 December 31

ABSTRACT

HD 213597 is an eclipsing binary system which was detected by the *STEREO* spacecraft and was speculated to host a low-mass stellar companion. We used high-resolution spectroscopy with the 10-m Hobby–Eberly Telescope and the 1.2-m telescope in Mount Abu for radial velocity (RV) measurements of this source. We performed aperture photometry for this star on the *STEREO* archival data and thereby confirm the transit signature. We also did follow-up ground-based photometry with a 10-inch telescope from Mt Abu. The spectroscopic RV semi-amplitude of the primary (33.39 km s^{-1}) indicates that the secondary is an M dwarf making the system a short period F+M eclipsing binary. These RVs along with the inclination derived from our combined photometric analysis ($i = 84\overset{\circ}{.}9$), enable us to estimate the mass of the secondary as $M_B \sim 0.286\,\mathrm{M}_\odot$ and radius as $R_B \sim 0.344\,\mathrm{R}_\odot$ using an estimated mass $M_A \sim 1.3\,\mathrm{M}_\odot$ and radius $R_B \sim 1.97\,\mathrm{R}_\odot$ of the primary. Our spectral analysis returned the following parameters: $T_{\mathrm{eff}} = 6625 \pm 121$ K, [Fe/H] $= -0.095 \pm 0.08$ and $\log g = 3.72 \pm 0.22$ for the primary. When $\log g$ is constrained to a value of 3.96, we derive $T_{\mathrm{eff}} = 6753 \pm 52$ K and [Fe/H] $= -0.025 \pm 0.05$.

Key words: techniques: photometric – techniques: radial velocities – binaries: eclipsing – stars: individual: HD 213597 – stars: low-mass.

1 INTRODUCTION

Mass and radius are the two fundamental properties of a star that allow us to determine their age, evolution and luminosity (Andersen 1991). Through careful photometry and spectroscopy of detached single- and double-lined eclipsing binaries, it is possible to obtain radii and masses of individual components to as high accuracies as 1 per cent for double-lined eclipsing binaries. Such precise measurements impose strong constraints on stellar evolution models. In recent years, such measurements have revealed discrepancies between observed and model-derived stellar radii of low-mass stars (Torres, Andersen & Giménez 2010). For stars with masses below $0.5\,\mathrm{M}_\odot$, the measured radii appear to be 20–30 per cent larger than predicted (López-Morales 2007). One hypothesis suggests that this disagreement is caused by the degree of magnetic activity in stars: strong magnetic fields inhibit convection causing stars to inflate their radii (Mullan & MacDonald 2001; López-Morales & Ribas 2005). Another hypothesis suggests metallicity dependency on radii inflation: Berger et al. (2006) in their study find that the disagreement is larger among metal-rich stars than metal-poor stars. They conclude that current atmospheric models do not take into account opacity sources which may lead to such discrepancy. Therefore, it becomes imperative to discover more such systems and determine their masses and radii to very high precision.

F-type stars are typically fast rotators with a tenuous convective zone. Bouchy et al. (2011a) suggest that there is a higher probability of M dwarfs orbiting F-type primaries, in contrast to G-type primaries. Bouchy et al. (2011a,b) further suggest that for a massive companion to exist around a primary star, the total angular momentum must be above a critical value. If a primary star has a smaller spin period than the orbital period of the system (as in the case for G-type stars), the tidal interactions between the two stars will cause the secondary companion to be eventually engulfed by the primary. However, this is less likely to occur among fast rotating F-type stars which have weaker magnetic braking and can avoid the spin-down caused due to the tides raised by the massive secondary. This helps the companions around F-type stars to survive rapid

⋆ E-mail: priyanka@prl.res.in

Table 1. Stellar properties of host star HD 213597A from literature.

Parameter	Value	Reference
Mass	1.5 ± 0.1 $M_{\odot}$	(1)
Radius	2.039 ± 0.303 $R_{\odot}$	(2)
$\log g$	3.99 ± 0.05	(1)
$v\sin i$	40 ± 5 km s^{-1}	(3)
$T_{\rm eff}$	6837 ± 80 K	(1)
[Fe/H]	-0.14 ± 0.1	(1)
Age	1.90 ± 0.2 Gyr	(1)
Distance	115 ± 15 pc	(4)
V magnitude	7.8	(5)
RA (epoch=2000)	$22^{\rm h}32^{\rm m}32\overset{\rm s}{.}626$	(5)
Dec. (epoch=2000)	$1°34'56\overset{''}{.}83$	(5)

References: (1) Casagrande et al. (2011); (2) Masana et al. (2006); (3) Nordström et al. (2004); (4) from *Hipparcos* data; (5) from SIMBAD.

orbital decay due to loss of angular momentum. F-type primaries with M-type secondaries (hereafter F+M binaries) are often discovered in transit surveys, which are primarily designed to search for transiting planets (e.g. Bouchy et al. 2005; Beatty et al. 2007). Over the last few years a handful of F+M binaries have been discovered and their properties determined (e.g. Pont et al. 2005a,b, 2006; Fernandez et al. 2009). Nonetheless, every additional system discovered and analysed contributes more to our understanding of fundamental stellar properties making the sample of F+M binaries an important subset of stellar studies.

The NASA *STEREO* mission consists of two satellites in the heliocentric orbit that study the Sun and its environment. An imager on one of the satellites is being employed to study the variability of bright stars and to look for transiting exoplanets. Observations taken by the *STEREO* spacecraft were analysed by Wraight et al. (2012) to search for low-mass eclipsing companions to bright stars with effective temperatures between 4000 and 7000 K and visual magnitude $6 < V < 12$. The *STEREO* Heliospheric Imagers (HIs) have a field of view of $20° \times 20°$ and a 2048×2048 element CCD with a spectral response that peaks between 6300 and 7300 Å (Wraight et al. 2012). HD 213597 was one of the nine candidates selected (Wraight et al. 2012) where the radius of the secondary was estimated to be below 0.4 $R_{\odot}$. HD 213597A, with a visual magnitude of 7.8, is an F-type star having a rotational velocity of 40 km s^{-1} (Nordström et al. 2004) and a radius of 2.039 $R_{\odot}$ (Masana, Jordi & Ribas 2006). Table 1 lists the properties of this star obtained from the literature. The earlier studies on this star suggest that it may host a low-mass companion.

Here, we describe high-resolution spectroscopic and photometric observations and the methods of analysis used to derive the physical parameters concerning HD 213597 system. Details of the spectroscopic observations and transit photometry are reported in Section 2, while Section 3 describes the analytic methods and main results. Discussion and conclusions are presented in Section 4.

2 SPECTROSCOPIC AND PHOTOMETRIC OBSERVATIONS OF HD 213597

2.1 Spectroscopy

High-resolution spectroscopic observations of the star HD 213597A were made with the fibre-fed high-resolution spectrograph (HRS; Tull 1998) at the 10-m McDonald Hobby–Eberly Telescope (HET; Ramsey et al. 1998), and the fibre-fed echelle spectrograph, Physical Research Laboratory Advanced Radial Velocity Abu-sky Search (PARAS; Chakraborty et al. 2014) at the 1.2-m telescope at Gurushikhar Observatory, Mount Abu, India.

2.1.1 HET-HRS observations

We obtained nine observations between 2011 October and 2012 July using the HRS in its 316g5936 cross-disperser setting, 2 arcsec diameter fibre, resolution of ∼30 000 and a simultaneous wavelength coverage of 4300–5800 and 6200–7600 Å. The exposure times ranged between 60 and 300 s, which yielded signal-to-noise ratio (S/N) between 200 and 600 per resolution element. Each observation was bracketed before and after with a thorium–argon (ThAr) lamp exposure for wavelength calibration. The same procedure was used on HD 215648, which served as a template to derive radial velocities (RVs). HD 215648 has a spectral type of F7V with $T_{\rm eff} = 6228 \pm 100$ K, $\log g = 4.15 \pm 0.07$ (Edvardsson et al. 1993), $v\sin i = 6.7 \pm 0.7$ km s^{-1} (Ammler-von Eiff & Reiners 2012) and [Fe/H] $= -0.22$ (Valenti & Fischer 2005). The data were reduced using a custom optimal extraction pipeline as described in Bender et al. (2012).

2.1.2 Mt Abu-PARAS observations

A total of 15 observations were taken between October and November 2012 using the fibre-fed PARAS spectrograph which has a single prism as a cross-disperser, a blaze angle of 75° and a resolution of 67 000. The exposure time for each observation was fixed at 1200 s which resulted in S/N between 20 and 25 pixel^{-1} at the blaze wavelength. Simultaneous exposures of the science target and the ThAr lamp for wavelength calibration were taken. The wavelength region between 3700 and 6800 Å was considered for the RV measurements. The data were reduced by the Interactive Data Language (IDL) pipeline designed specifically for PARAS as described in Chakraborty et al. (2014).

2.1.3 Errors on radial velocity measurements

The precision on RV measurements (Hatzes & Cochran 1992) is given as $\sigma \sim 1.45 \times 10^9 ({\rm S/N})^{-1} R^{-1} B^{-1/2}$ m s^{-1}, where S/N is the signal-to-noise ratio of the spectra, while R and B are the resolving power and wavelength coverage of the spectrograph in angstrom (Å), respectively. Although PARAS has much higher resolution than the HET-HRS mode that was used, the S/N of PARAS spectra is lower, leading to the PARAS RVs having larger uncertainties than the HET-HRS RVs. As mentioned earlier, HD 213597A is an early F-type star with a rotational velocity of 40 km s^{-1}. Bouchy, Pepe & Queloz (2001) defined a quality factor Q that represents the quality and spectral line richness of the spectrum. It was further shown that Q deteriorates with increasing rotational velocity thereby increasing the RV uncertainty. For instance, a F2-type star with a rotational velocity of 40 km s^{-1} has a RV uncertainty 10 times larger than one that is rotating at 4 km s^{-1}. The covariant errors obtained from fitting the peak of the cross-correlation function in IDL are reported as uncertainties on the HET data. For PARAS spectra, errors based on photon noise are computed for each spectrum as discussed in Bouchy et al. (2001). Since HD 213597A has a RV semi-amplitude of ∼33 km s^{-1}, for a relatively small orbital period of 2.4238 d, the RVs get smeared within the duration of the exposure as a function of orbital phase. The orbital smearing errors were estimated and

Table 2. Observations for the star HD 213597. The time in UT and BJD–TDB are mentioned in first two columns followed by exposure time and barycentric corrected RV in third and fourth column, respectively. The next two columns have RV errors, fifth column corresponds to covariant errors (HET-HRS) or photon noise errors (PARAS) and column 6 has orbital smearing errors. Last column is the instrument used for observations.

UT date	T-240 0000 (BJD–TDB)	Exp. time (s)	RV (km s^{-1})	σ-RV (km s^{-1})	σ-orbital smearing (km s^{-1})	Instrument (flag)
2011 Oct 30	55864.689	250	4.844	0.209	0.167	HET-HRS
2011 Nov 25	55890.614	60	11.822	0.208	0.030	HET-HRS
2011 Nov 27	55892.609	180	−20.967	0.214	0.116	HET-HRS
2011 Dec 15	55910.552	60	15.026	0.212	0.026	HET-HRS
2012 Jun 11	56089.949	300	14.561	0.210	0.142	HET-HRS
2012 Jun 22	56100.924	300	−30.586	0.217	0.162	HET-HRS
2012 Jun 23	56101.918	300	19.909	0.212	0.064	HET-HRS
2012 Jul 01	56109.905	180	−27.993	0.204	0.103	HET-HRS
2012 Jul 02	56110.901	300	−9.125	0.214	0.203	HET-HRS
2012 Oct 17	56218.260	1200	2.940	0.148	0.255	PARAS
2012 Oct 17	56218.276	1200	2.905	0.176	0.290	PARAS
2012 Oct 17	56218.292	1200	2.134	0.180	0.325	PARAS
2012 Oct 18	56219.210	1200	−61.491	0.248	0.253	PARAS
2012 Oct 18	56219.225	1200	−61.522	0.242	0.219	PARAS
2012 Oct 18	56219.241	1200	−62.592	0.226	0.185	PARAS
2012 Oct 21[a]	56222.269	1200	−42.356	0.267	0.805	PARAS
2012 Oct 21[a]	56222.285	1200	−36.462	0.283	0.813	PARAS
2012 Oct 23	56224.198	1200	−62.984	0.148	0.051	PARAS
2012 Oct 23	56224.214	1200	−62.904	0.158	0.085	PARAS
2012 Nov 7	56239.202	1200	−42.605	0.148	0.763	PARAS
2012 Nov 7	56239.219	1200	−40.721	0.155	0.773	PARAS
2012 Nov 7	56239.234	1200	−39.516	0.167	0.783	PARAS
2012 Nov 8	56240.179	1200	0.438	0.188	0.479	PARAS
2012 Nov 8	56240.195	1200	−1.008	0.183	0.511	PARAS

[a]Not considered for RV analysis.

added quadratically with the photon noise and covariant errors for both PARAS and HET data points and used as uncertainties for individual RV points. The barycentric corrected RV values along with the associated uncertainties are mentioned in Table 2. Over the course of 1 yr (2011 October–2012 November) we obtained a combined total of 24 observations with the two spectrographs. Two epochs from the observed RVs of PARAS data were removed in the fitting routine because of very low S/N (due to passing clouds).

2.2 Transit photometry

We performed ground-based photometric observations for this star from the calculated mid-eclipse time based on the ephemeris of Wraight et al. (2012). Given the celestial coordinates of the star (refer Table 1) and the prolonged monsoon in India, we get a narrow window of 3 weeks in the month of October to observe the complete transit of the object. Thus, we also revisited the archival *STEREO* data (Wraight et al. 2012), in order to compute the transit parameters like transit duration and angle of inclination in combination with our ground-based photometry at Physical Research Laboratory (PRL), Mount Abu, India.

STEREO data from HI-1A instrument were extracted from the UK Solar System Data Centre (UKSSDC) website.[1] The star was observable for a period of 16–17 d on the CCD for each cycle of observation. Six such cycles of data were used for HD 213597A between the period 2008 January to 2012 October. For our purposes, we used L2 images, which were pre-processed (bias subtracted and flat-fielded) and accounted for solar coronal contamination. The wavelength band of observation is narrowly peaked between 630 and 730 nm (Wraight et al. 2012). A total of 36 transits for HD 213597A were recorded in six cycles of the extracted data.

We also obtained follow-up photometric observations of HD 213597A with the PRL 10-inch telescope at Gurushikhar, Mount Abu, India. We carried out photometry on 2013 October 21 UT for a duration of 5 h. The observations were carried out using a Johnson R band with a back thinned E2V 1k × 1k CCD array with a field of view of 46 × 46 arcmin^2. A mismatch of the dome position while guiding resulted in the rejection of an hour-long observation. Furthermore, due to passing clouds, we lost about 20 per cent of the egress time. Despite the data loss, we detected the transit at a confidence level of 4σ.

[1] www.ukssdc.rl.ac.uk

3 ANALYSIS AND RESULTS

3.1 Radial velocity measurements

3.1.1 HET-HRS

The reduced data were wavelength calibrated and continuum normalized while the echelle orders were stitched to produce a continuous 1D spectrum between two wavelength regions of 4300–5800 and 6200–7500 Å. The spectrum was then divided into eight segments (4386–4486, 4593–4843, 4925–5025, 5100–5410, 5475–5800, 6365–6430, 6620–6850, 7450–7500 Å) that are free of telluric lines. Each segment was cross-correlated using a 1D cross-correlation algorithm. The resulting 1D correlation arrays were

Table 3. Spectroscopically determined stellar parameters of HD 213597A (this work). The two measurements listed for each stellar parameter results from two SME run: (1) when all parameters are allowed to float; (2) when $\log g$ is fixed to a value determined by mass and radius measurements.

Stellar parameter	Value (free parameters)	Uncertainty	Value (constrained fitting)	Uncertainty
$T_{\rm eff}$ (K)	6625	± 121	6752	± 52
$\log g$	3.72	± 0.22	3.96	–
[Fe/H]	-0.095	± 0.08	-0.025	± 0.05
[M/H]	-0.156	± 0.03	-0.105	± 0.03
$v\sin i$ (km s^{-1})	39.53	± 1.3	39.53	± 1.3
Microturbulence (km s^{-1})	2	–	2	–

combined using the maximum likelihood method (Zucker 2003). We employed a robust non-linear least-square curve fitting algorithm, MPFIT in IDL, to fit the peak of the cross-correlation function and determine the RVs and the associated errors.

3.1.2 *Mt Abu-PARAS*

The entire reduction and analysis for PARAS was carried out by the custom-designed pipeline in IDL based on the REDUCE optimal extraction routines of Piskunov & Valenti (2002). The pipeline performs the routine tasks of cosmic ray correction, dark subtraction, order tracing and order extraction. A complete thorium line list for the PARAS spectral range is utilized. The wavelength calibration algorithms were specifically optimized for PARAS as described in Chakraborty et al. (2014). The RV values were computed by cross-correlating the observed spectra against an F-type binary mask. Barycentric corrections were applied to all the RV points by standard IDL routines. The binary mask was created with the SPECTRUM program (Gray 2009) using Kurucz stellar atmosphere models with a temperature of $T_{\rm eff}$ = 6750 K, $\log g$ = 4.0 and a metallicity [M/H] = -0.2 (refer Table 1).

3.2 Spectral analysis

We based our spectral analysis of HD 213597A on the SME (Valenti & Piskunov 1996) spectral synthesis code. SME is composed of a radiative transfer engine that generates synthetic spectra from a given set of trial stellar parameters and a Levenberg–Marquardt solver that finds the set of parameters (and corresponding synthetic spectrum) that best matches observed input data in specific regions of the spectrum. The basic parameters that we used to define a synthetic spectrum are effective temperature ($T_{\rm eff}$), surface gravity ($\log g$), metallicity ([M/H]), iron abundance relative to solar ([Fe/H]) and projected rotational velocity ($v\sin i$). In order to match an observed spectrum, we solved for these five parameters. SME was implemented by using the Advanced Computing Centre for Research and Education (ACCRE) High-Performance Computing Center at Vanderbilt University for a large number (150) of different initial conditions to fully explore the χ^2 space and find the optimal solution at the global minimum. In addition, we applied a line list based on Stempels et al. (2007) that is suited for hotter stars, used the MARCS model atmosphere grid in the radiative transfer engine, and obtained the microturbulence ($v_{\rm t}$) from the polynomial relation defined in Gómez et al. (2013).

We applied our SME pipeline to the high S/N HET spectrum of HD 213597A allowing all five parameters listed above to vary freely. We obtained $T_{\rm eff} = 6625 \pm 121$ K, $\log g = 3.72 \pm 0.22$ and [Fe/H] = -0.095 ± 0.08. It is important to note that for hotter stars, uncertainties on the gravity derived from spectral synthesis increase because the wings of the Mg I b triplet at 5167, 5172 and 5183 Å used to constrain this parameter become narrower and less sensitive to gravity. We also ran our SME pipeline again, this time constraining $\log g = 3.96 \pm 0.1$ based on the literature cited value. In this set of 150 trials, we fixed the gravity to a randomly chosen value within this range and solve for the other four parameters. For the constrained run, we obtained $T_{\rm eff} = 6752 \pm 52$ K, iron abundance ([Fe/H]) = -0.025 ± 0.05 and metallicity ([M/H]) = -0.105 ± 0.03.

The formal 1σ errors are based on the $\delta\chi^2$ statistics for the five free parameters. To derive the systematic uncertainties, we compared the results of our pipeline to three independent data sets with parameters in the literature (Valenti & Fischer 2005; Torres et al. 2012; Huber et al. 2013) and report the mean absolute deviation of our results compared to all the comparison stars. The final results (both free and constrained $\log g$) are listed in Table 3 along with their combined statistical and systematic uncertainties. Fig. 1 shows a sample of the observed spectrum (solid line) overlaid by the best-fitting model obtained by a free parameter fit ($T_{\rm eff}$ = 6625 K, [Fe/H] = -0.095, $\log g$ = 3.72, dotted line). The observed and model spectra are shown across the wavelength region 5160–5190 Å, including the Mg I b triplet.

3.3 Transit

The *STEREO* images from HI, HI-1A, L2 data are a priori bias and flat corrected. These files have a field of view of 20° × 20° imaged on a 2k × 2k CCD. The data were 2 × 2 binned on a 1k × 1k image with a field of view of 70 × 70 arcsec^2 pixel^{-1}. Each image is a sum of 30 exposures with a total exposure time of 20 min and an observational cadence of 40 min (Wraight et al. 2011). The procedure given in Sangaralingam & Steven (2011) was followed to do aperture photometry on the data. An aperture of 3.5 pixels was chosen for the same. We used the standard IRAF[2] DAOPHOT package for processing the photometry data. The flux computed by IRAF was detrended by fitting a fourth-order polynomial to account for the CCD response function as discussed in Sangaralingam & Steven (2011). The data were further normalized for each cycle. The rms scatter on the light curve for the source star outside the transit time duration is 7 mmag. A total of 36 transits were obtained for the entire data of six cycles between the period 2008 January–2012 October.

For the ground-based photometry observations from Mt Abu on 2013 October 21, each individual frame had an exposure time of 2 s and a readout time of ∼1 s. Similar to the *STEREO* data, IRAF

[2] IRAF is distributed by the National Optical Astronomy Observatory, which is operated by the Association of Universities for Research in Astronomy, Inc., under cooperative agreement with the National Science Foundation.

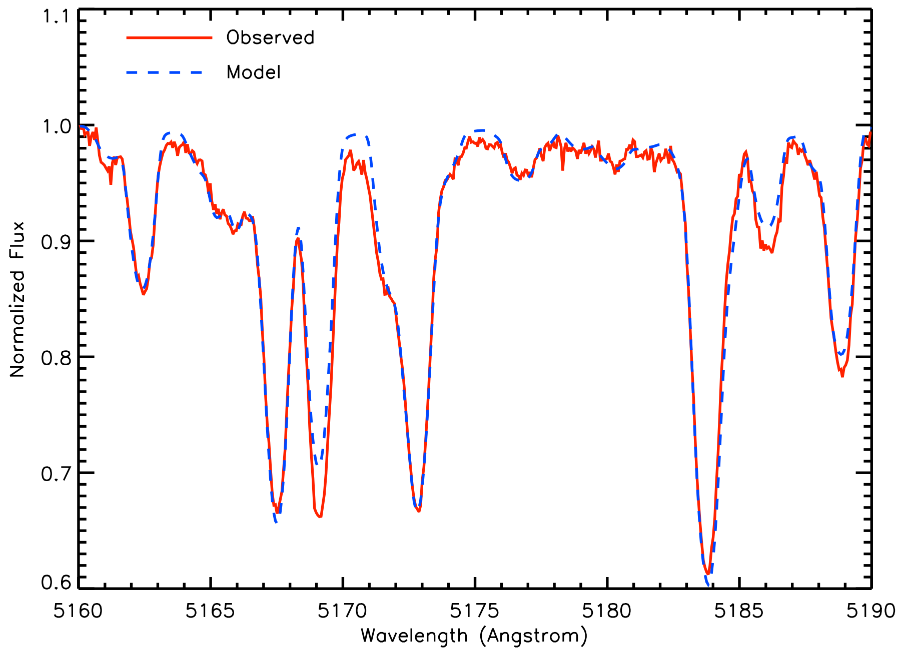

Figure 1. Observed normalized spectra (solid line) plotted across the wavelength region of 5160–5190 Å covering the Mg I triplet at 5167, 5172 and 5183 Å. Overplotted is the modelled spectra (dash line) obtained from SME analysis (when all parameters are kept free), with temperature value of $T_{\rm eff}$ of 6625 K, [Fe/H] of 0.095 and log g of 3.72.

DAOPHOT package was used to perform aperture photometry on the data. The frames were flat-fielded and dark corrected. Varying airmass and other local sky variations are accounted for, to an extent, by performing differential photometry on a comparison star and a check star. For differential photometry, we need a comparison star which is non-varying with time and is similar in colour and magnitude to the program star. We chose HD 213763 with spectral type F5V and a visual magnitude of 7.8 as the comparison star. In order to cross-check the non-variability of the comparison star, we required another field star called check star, which in our case was HD 213598 (K0V with a visual magnitude of 9.14). Although it is desirable to choose a check star of similar colour as that of the source and comparison stars, we settled for a K-type check star due to unavailability of bright field stars in the near vicinity. Since we used the Johnson *R* band for our photometry observations, the effect of scattering by moonlight and the atmospheric extinction was minimal. The average S/N of the source and the comparison star was between 300 and 350 for individual frames. 60 consecutive frames of similar exposures were median combined to avoid the scintillation noise from sky which, otherwise, becomes the dominant source of noise. Thus, each binned data frame comprised a total exposure time of 120 s and a total time cadence of 202 s (including the readout time) making the S/N of the combined frame to be ∼2500 for the same stars. Differential photometry was performed on the program star, HD 213597A and additional two bright field stars (HD 213763 and HD 213598). Individual light curve of comparison and check star showed a rms scatter of 12 mmag over the entire observation period. The rms scatter between the comparison and the check star reduced to 6 mmag after differential photometry. This formed the base level for detection of any transit and thus reflected the photometric error on each data point in the light curve. The data from *STEREO* and PRL 10-inch telescope were combined to produce a phase-folded light curve as both the data sets were observed in *R* band and had similar photometric errors on them.

3.4 Simultaneous spectroscopy and photometry fitting

We simultaneously fit the spectroscopy and photometry data with EXOFAST (Eastman, Gaudi & Agol 2013). EXOFAST is a set of IDL routines designed to fit transit and RV variations simultaneously or separately, and characterize the parameter uncertainties and covariances with a Differential Evolution Markov chain Monte Carlo method (Johnson et al. 2011). It can either fit RV and transit values exclusively or use both data sets to give a simultaneous fit. It also requires priors on $T_{\rm eff}$, log g and iron abundance [Fe/H]. EXOFAST uses empirical polynomial relations between masses and radii of stars; their log g, $T_{\rm eff}$ and [Fe/H] based on a large sample of non-interacting binary stars in which all of these parameters were well measured (Torres et al. 2010). These priors are used as a convenient way of modelling isochrones and are fast enough to incorporate them at each step in Markov chain. The errors derived here are determined by evaluating the posterior probability density based on the range of a given parameter that encompasses some set fraction of the probability density for the given model. We thereby caution the reader that the errors reported here for the mass and radius of the secondary are formal errors from EXOFAST. These values and errors are themselves based on models and isochrones and should not be used as independent observational checks on these models until more precise values can be derived in the future by teasing out a double-lined spectroscopy orbital solution for this system.

We executed the EXOFAST routine with the combined RV data sets (HET-HRS and PARAS) and the combined photometry data sets (one from the transit light curve obtained by *STEREO* and the other one obtained by PRL 10-inch telescope). On varying the SME-derived parameters as input priors to EXOFAST, we found that constraining log g with the same uncertainties as given in Table 3 yielded the most consistent values for $T_{\rm eff}$ and [Fe/H] (best simultaneous fit for RV and transit data). The results of the execution are summarized in Table 4. Fig. 2 illustrates the RV versus orbital

Table 4. Results obtained from EXOFAST by simultaneous fitting of RV and transit data for HD 213597 with a 68 per cent confidence interval.

Parameter	Units	Values
HD 213597A		
M_A	Mass ($M_\odot$)	$1.293^{+0.12}_{-0.1}$
R_A	Radius ($R_\odot$)	$1.973^{+0.085}_{-0.080}$
L_A	Luminosity ($L_\odot$)	$7.04^{+0.60}_{-0.52}$
ρ_A	Density (cgs)	$0.2377^{+0.0054}_{-0.0053}$
$\log g_A$	Surface gravity (cgs)	3.96 ± 0.01
$T_{\rm eff}$	Effective temperature (K)	6699^{+53}_{-52}
[Fe/H]	Iron abundance	$-0.065^{+0.050}_{-0.048}$
HD 213597B		
e	Eccentricity	$0.0198^{+0.0094}_{-0.0091}$
ω_*	Argument of periastron (°)	72^{+12}_{-18}
P	Period (d)	$2.4238503^{+0.000017}_{-0.0000019}$
a	Semimajor axis (au)	$0.04112^{+0.00058}_{-0.00057}$
M_B	Mass ($M_\odot$)	$0.286^{+0.012}_{-0.01}$
R_B	Radius ($R_\odot$)	$0.344^{+0.0097}_{-0.01}$
ρ_B	Density (cgs)	$9.32^{+0.43}_{-0.41}$
$\log g_B$	Surface gravity	$4.803^{+0.0093}_{-0.0097}$
RV parameters		
$e\cos\omega_*$		$0.0056^{+0.0043}_{-0.0042}$
$e\sin\omega_*$		$0.0184^{+0.0096}_{-0.0097}$
$T_{\rm P}$	Time of periastron (BJD)	$245\,5392.09^{+0.087}_{-0.12}$
K	RV semi-amplitude m s^{-1}	33390^{+290}_{-280}
M_B/M_A	Mass ratio	0.2218 ± 0.0045
γ	Systemic RV m s^{-1}	-4420^{+180}_{-190}
$f(m)$	Mass function[a] ($M_\odot$)	0.0091 ± 0.000048
Transit parameters		
$T_{\rm C}$	Time of transit (BJD)	$245\,5392.2014^{+0.0015}_{-0.0016}$
R_B/R_A	Radius of secondary in terms of primary radius	0.178 ± 0.001
i	Inclination (°)	$84.9^{+0.61}_{-0.50}$
a/R_A	Semimajor axis in stellar radii	$4.48^{+0.039}_{-0.038}$
δ	Transit depth	$0.0317^{+0.0013}_{-0.0012}$
T_{14}	Total transit duration (min)	274^{+5}_{-4}

[a]By BOOTTRAN (IDL).

phase for HD 213597A. Solid and open circles (top panel) show RV measurements of the primary taken with the HRS and PARAS instruments, respectively. The figure also shows the residuals (observed model) in the bottom panel. There are four RV measurements for this star from Nordström et al. (1997) observed with the 1.5-m Wyeth reflector at the Oak Ridge Observatory in Harvard, MA. We corrected for the offset in RV and overplotted these points in Fig. 2 to give it a longer time base. However, we did not include these points in the model due to their relatively large errors. It is important to note that despite a long time-gap between our observations and those of Nordström et al. (1997), their RV measurements (asterisks) lie on the model curve as shown in Fig. 2.

Fig. 3 (upper panel) shows the simultaneous fit for the transit light curve obtained by analysing *STEREO* archival data (filled circles) and PRL 10-inch telescope data (open squares) overplotted with the model derived from EXOFAST (solid curve). The residuals are plotted in lower panel. The simultaneous fit gives us a transit depth of $0.0317^{+0.0013}_{-0.0012}$ mag, angle of inclination of $84.9^{+0.62}_{-0.5}$ and a transit time duration of 274^{+5}_{-4} min. The transit depth cited here is consistent with the refined analysis of *STEREO* light curve by Whittaker, Stevens & Sangaralingam (2013). We obtain the mass of the secondary as $0.286^{+0.012}_{-0.01}$ $M_\odot$ and a radius of $0.344^{+0.0097}_{-0.01}$ $R_\odot$. We also calculated the mass function for this system by using the IDL BOOTTRAN package (Wang et al. 2012). The results obtained by the combined RV and transit data sets are consistent with the period 2.4238 d (Wraight et al. 2012; Whittaker et al. 2013) with a semimajor axis of 4.48 $R_\star$ (0.041 au) and a RV semi-amplitude of 33.39 km s^{-1}. Based on the mass limits, we conclude that the secondary star is an early M dwarf (Baraffe & Chabrier 1996).

4 DISCUSSION AND CONCLUSIONS

Using high-resolution spectroscopy taken with the HET-HRS, PARAS spectrographs and photometry with the *STEREO* data, PRL 10-inch telescope, we conclude that HD 213597 is an eclipsing binary system with an F-type primary and an early M-type secondary. The estimated secondary mass from RV measurements is $M_B = 0.286^{+0.012}_{-0.01}$ $M_\odot$ with an accuracy of ~3–4 per cent (formal

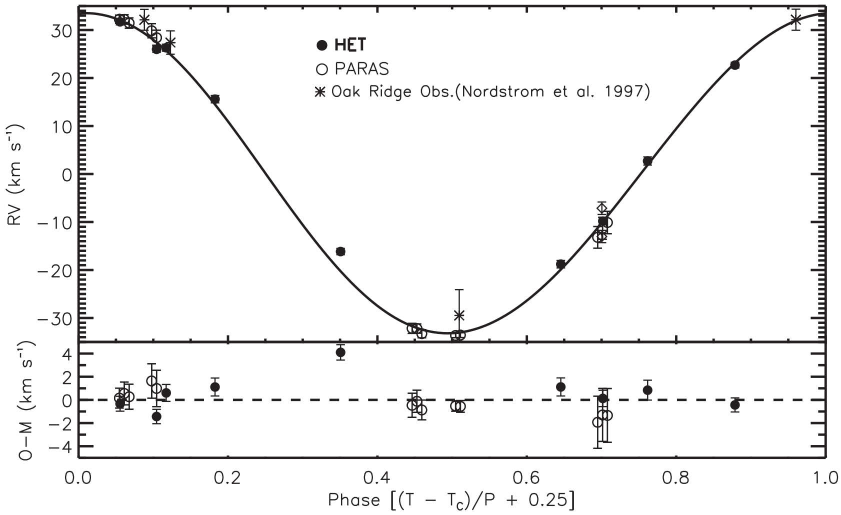

Figure 2. Top panel: RV model curve for star HD 213597 obtained from EXOFAST is plotted against orbital phase. HRS-HET (filled circles) and PARAS, Mount Abu (open circles) observed data points along with the estimated errors are overplotted on the curve. The two data points from PARAS not considered for RV fitting are overplotted with diamonds. The four RV measurements (not considered for RV fitting) from Nordström et al. (1997) are overplotted on the modelled data. Bottom panel: the residuals from best-fit are plotted below the RV plot. The residuals are not plotted for the points which are not considered for the RV fitting. For better visual representation, the *x*-axis in phase is shifted by 0.25 so that the central primary transit crossing point (T_c) occurs at phase 0.25 instead of 0.

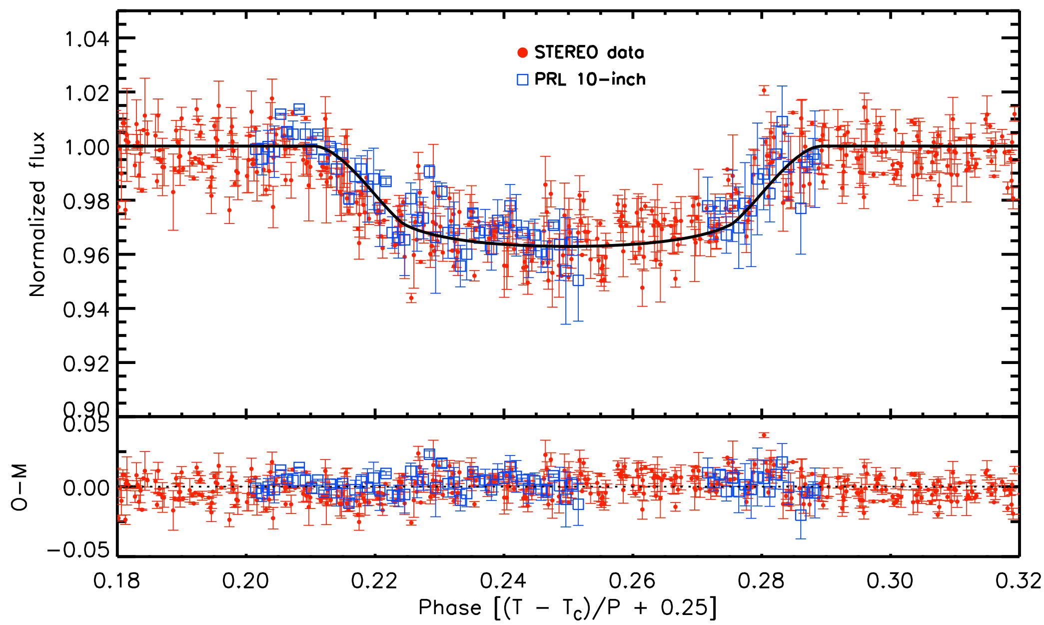

Figure 3. Top panel: transit curve obtained from *STEREO* data and PRL 10-inch telescope is plotted based on the parameters from EXOFAST. The *STEREO* data are plotted with (red) filled circles and the PRL 10-inch telescope data are plotted with open (blue) squares along with their individual error bars. (Colours are only in online version.) Bottom panel: observed-fit residuals are plotted. For better visual representation, the *x*-axis in phase is shifted by 0.25 so that the central primary transit crossing point (T_c) occurs at phase 0.25 instead of 0.

errors). Based on the transit depth of $0.0317^{+0.0013}_{-0.0012}$ mag, the radius of the secondary is estimated to be $R_B = 0.344^{+0.0097}_{-0.01}\,R_\odot$ with an accuracy of ∼5–6 per cent (formal errors). The radius estimated here is in good agreement with the value given by Wraight et al. (2012).

Metallicity and the iron abundance of the system are accurately determined in this work as -0.105 ± 0.03 and -0.025 ± 0.05 (see Table 3) by spectroscopic analysis. From the models for M dwarfs (Baraffe et al. 1998), we estimate the $T_{\rm eff}$ of the secondary star for a mass of $\sim 0.3\,M_\odot$ (from this work) and an age of ∼2 Gyr (Casagrande et al. 2011), as 3437 K for a [M/H] of 0.0, and 3643 K for a [M/H] of −0.5. From Baraffe et al. (1998) models, the radius for $0.3\,M_\odot$ turns out to be $0.29\,R_\odot$ for [M/H] = 0.0 and $0.28\,R_\odot$ for [M/H] = −0.5. Clearly, these theoretically derived radius values are lower than the observations presented here.

The binary system has an inclination angle of $84\overset{\circ}{.}9^{+0.61}_{-0.5}$. The rotational velocity of the primary star obtained by SME analysis, as mentioned in Table 3, is 40 km s^{-1}, which matches when measured by the width of the cross-correlation function. This value is comparatively lower than the reported rotational velocities for similar

F-type stars (Gĺébocki & Gnaciński 2005). With the knowledge of rotational velocity of the primary star and its radius of $\sim$2.03 $R_\odot$ from Table 1, the projected spin period $P/\sin i$ of the primary star is calculated to be 2.422 d, which is close to the observed orbital period of the system. The eccentricity of the system, calculated as 0.0198, makes it close to circular. Since the orbital and rotational periods for the star are synchronous, this star forms another evidence for tidal circularization playing role in a close binary system (Mazeh 2008).

The detailed spectral analysis of the high S/N HET spectra gives us $T_{\rm eff}$= 6752 $\pm$ 52 K, [Fe/H] = $-$0.025 $\pm$ 0.05 for $\log g$ = 3.96 $\pm$ 0.1. The temperature indicates an F-type primary star. It may be mentioned that Masana et al. (2006) obtained a $T_{\rm eff}$ of 6936 $\pm$ 70 K based on V and Two Micron All Sky Survey (2MASS) *JHK* photometry, while Casagrande et al. (2011) reported a value of 6837 $\pm$ 80 K based on improved colour calibration of the same bands. Our results are more reliable as they are based on detailed spectral analysis from high S/N spectra. Furthermore, these results are substantiated by the fact that the RV and photometry data are not able to constrain a solution in EXOFAST by using the previously cited $T_{\rm eff}$ value of 6936 $\pm$ 70 K. Using $T_{\rm eff}$, [Fe/H] and $\log g$ derived from this work, the mass and radius of the primary star obtained from mass–radius relationship (Torres et al. 2010) are 1.48 $M_\odot$ and 2.11 $R_\odot$, respectively, consistent with the values reported in literature (see Table 1).

Future spectroscopic observations of this star during transit will enable us to observe the Rossiter–McLaughlin effect (Scott Gaudi & Winn 2007), and help determine whether the secondary star is in retrograde or prograde orbital motion with respect to the rotation of the primary. This may lead to a better understanding of the binary formation mechanisms at a primordial stage. Future high-resolution near-infrared observations will be able to provide dynamical masses of the system.

ACKNOWLEDGEMENTS

This work has been made possible by the PRL research grant for PC and the PRL–DOS (Department of Space, Government of India) grant for the PARAS spectrograph. This work was partially supported by funding from the Center for Exoplanets and Habitable Worlds. The Center for Exoplanets and Habitable Worlds is supported by the Pennsylvania State University, the Eberly College of Science and the Pennsylvania Space Grant Consortium. We thank the observatory staff at the Hobby–Eberly Telescope (HET) and the PRL Mt Abu telescope from where the data were obtained. HET is a joint project of the University of Texas at Austin, the Pennsylvania State University, Stanford University, Ludwig-Maximilians-Universität München and Georg-August-Universität Göttingen. The HET is named in honour of its principal benefactors, William P. Hobby and Robert E. Eberly. PC acknowledges help from Varun Dongre and Vishal Shah for their technical support during the course of data acquisition. We thank the UKSSDC team for the STEREO archival data. This research has made use of the ADS and CDS data bases, operated at the CDS, Strasbourg, France. We also thank the referee, Barry Smalley, for detailed and insightful comments which have helped to improve the quality of the paper significantly.

REFERENCES

Ammler-von Eiff M., Reiners A., 2012, A&A, 542, A116
Andersen J., 1991, A&AR, 3, 91
Baraffe I., Chabrier G., 1996, ApJ, 461, L51
Baraffe I., Chabrier G., Allard F., Hauschildt P. H., 1998, A&A, 337, 403
Beatty T. G. et al., 2007, ApJ, 663, 573
Bender C. F. et al., 2012, ApJ, 751, L31
Berger D. H. et al., 2006, ApJ, 644, 475
Bouchy F., Pepe F., Queloz D., 2001, A&A, 374, 733
Bouchy F., Pont F., Melo C., Santos N. C., Mayor M., Queloz M., Udry S., 2005, A&A, 431, 1105
Bouchy F. et al., 2011a, A&A, 525, A68
Bouchy F. et al., 2011b, A&A, 533, A83
Casagrande L., Shönrich R., Asplund M., Cassini S., Ramírez I., Meléndez J., Bensby T., Feltzing S., 2011, A&A, 530, 138
Chakraborty A. et al., 2014, PASP, 126, 133
Eastman J., Gaudi B. S., Agol E., 2013, PASP, 125, 83
Edvardsson B., Andersen J., Gustafsson B., Lambert D. L., Nissen P. E., Tomkin J., 1993, A&A, 275, 101
Fernandez J. M. et al., 2009, ApJ, 701, 764
Gĺébocki R., Gnaciński P., 2005, in Favata F., Hussain G. A. J., Battrick B., eds, Proceedings of the 13th Cambridge Workshop on Cool Stars, Stellar Systems and the Sun, ESA SP-560. ESA, Noordwijk, p. 571
Gómez Y. et al., 2013, ApJ, 768, 79
Gray R. O., 2009, Documentation for SPECTRUM v2.76, Appalachian State University
Hatzes A. P., Cochran W. D., 1992, in Ulrich M. H., ed., ESO Workshop on High Resolution Spectroscopy with the VLT. European Southern Observatory, Garching bei Munchen, Germany, p. 275
Huber D. et al., 2013, ApJ, 767, 127
Johnson J. A. et al., 2011, AJ, 141, 16
López-Morales M., 2007, ApJ, 660, 732
López-Morales M., Ribas I., 2005, ApJ, 631, 1120
Masana E., Jordi C., Ribas I., 2006, A&A, 450, 735
Mazeh T., 2008, in Goupil M. J., Zahn J. P., eds, EAS Publ. Ser. Vol. 29, Tidal Effects in Stars, Planets and Disks. EDP Sciences, France, p. 1
Mullan D. J., MacDonald J., 2001, ApJ, 559, 353
Nordström B., Stefanik R. P., Latham D. W., Andersen J., 1997, A&AS, 126, 21
Nordström B. et al., 2004, A&A, 418, 989
Piskunov N., Valenti J., 2002, A&A, 385, 1095
Pont F., Melo C. H. F., Udry S., Queloz D., Mayor M., Santos N. C., 2005a, A&A, 433, L21
Pont F., Bouchy F., Melo C., Santos N. C., Mayor M., Queloz D., Udry S., 2005b, A&A, 438, 1123
Pont F. et al., 2006, A&A, 447, 1035
Ramsey L. W. et al., 1998, Proc. SPIE, 3352, 34
Sangaralingam V., Steven I., 2011, MNRAS, 418, 1325
Scott Gaudi B., Winn J. N., 2007, ApJ, 655, 550
Stempels H., Collier Cameron A., Hebb L., Smalley B., 2007, MNRAS, 379, 773
Torres G., Andersen J., Giménez A., 2010, A&AR, 18, 67
Torres G., Fischer D. A., Sozzetti A., Buchhave L., Winn Joshua N., Holman Matthew J., Carter Joshua A., 2012, ApJ, 757, 161
Tull R., 1998, Proc. SPIE, 3355, 21
Valenti J. A., Fischer D. A., 2005, ApJS, 159, 141
Valenti J. A., Piskunov N., 1996, ApJS, 118, 595
Wang S. X. et al., 2012, ApJ, 761, 46
Whittaker G. N., Stevens I. R., Sangaralingam V., 2013, MNRAS, 431, 3456
Wraight K. T., White G. J., Bewsher D., Norton A. J., 2011, MNRAS, 416, 2477
Wraight K. T., Fossati L., White G. J., Norton A. J., Bewsher D., 2012, MNRAS, 427, 2298
Zucker S., 2003, MNRAS, 342, 1291

This paper has been typeset from a TEX/LATEX file prepared by the author.